Characterization of *in vitro* and *in cellulo* Tau protein aggregation by advanced light microscopy

Inaugural-Dissertation
to obtain the academic degree
Doctor rerum naturalium (Dr. rer. nat.)

submitted to the Department of Biology, Chemistry, Pharmacy of Freie Universität Berlin
by
Maximilian Walter Franck
From Stuttgart

Berlin, 2023

The work was conducted from September 2019 until June 2023 under supervision of Dr. Susanne Wegmann at the Deutsches Zentrum für Neurodegenerative Erkrankungen (DZNE) Berlin.

1st reviewer: Dr. Susanne Wegmann

2nd reviewer: Dr. Stephan Sigrist

Date of defense: 13.02.24

Acknowledgement

I would like to thank Susanne for her guidance, support and help within the last years. I really appreciated her support in letting me pursue my interest in microscopy by introducing me to a lot of people, which enabled me to learn a tremendous amount. Despite her packed schedule she always found the time to discuss with me my project and contribute with valuable ideas, critical appraisal and consistent motivation and vision. I am very grateful for everything I have learned.

I would also like to thank Prof. Stephan Sigrist, who kindly agreed to supervise my thesis.

I would like to thank our collaboration partners within this project, Dr. Thorsten Mielke, and everyone from the Max-Planck-Institute in Dahlem, as well as Dr. Abin Biswas from the Humbold-Universität. Thank you all for allowing me to use these amazing microscopes and supporting me along the way with any questions I had, as well as discussing experiments and how I could improve further.

Furthermore, I would also like to thank the staff from the AMBIO facility who helped with any microscopy questions I had at the Charité but also were very open to discussing imaging related topics-

Huge thanks go to all my colleagues, from whom everyone contributed enormously to provide the most pleasant working atmosphere.

Thank you, Lisa, I do believe without you the lab would not be where it is today. Not only did you help me with all molecular biology related questions, but you would also always listen and discuss project ideas with me. Thank you, Janine, for making it very easy for me to enter the world of Tau condensation and answering the same questions on how to prepare condensates a million times. Alvaro I would like to thank you for always helping me with my bacterial cultures and mini-preps and our many conferences calls and coffee breaks. Bilge thank you so much for our great gossip

breaks, cloning help and of course listening to me complain and helping me with my project. Satabdee and Leandre I would like to thank you guys as well for being great company and always having an open ear for any LLPS related questions I might have had. I would also like to thank two honorable members of Team Tau, Roberto & Marta for bringing Italian flair to the working environment always open for discussing imaging approaches and great food tips and dinners!

I would like to thank all my friends, Verena, Mick, Peter, and the guys from Berolina Stralau. And of course, my family who would always be by my side, listening to my struggles, helping me through some rough patches and just making my time in Berlin even better.

And most importantly I would like to thank Giulia who has always been by my side, always supporting me and believing in me, making me want to live up to the scientist she saw in me. I wouldn't be who I am today if it wasn't for her.

Selbstständigkeitseklärung

Herewith I certify that I have prepared and written my thesis independently and that I have not used any sources and aids other than those indicated by me. Intellectual property of other authors has been appropriately marked. Likewise, I assure that I have not applied for an examination procedure elsewhere, and the dissertation has not been submitted in this or any other form to any other faculty as a dissertation.

Datum: 13.02.24

Maximilian Walter Franck

Table of Contents

Abbreviations

2D	Two Dimensional
2N4R	Full Length Human Tau
3D	Three Dimensional
3R	Three Repeat Domain
4R	Four Repeat Domain
AD	Alzheimer's Disease
AGG	Aggregate
ALS	Amyotrophic Lateral Sclerosis
AMY	Amyloid-Like
APOE	Apolipoprotein E
APP	Amyloid Precursor Protein
ATP	Adenosine Triphosphate
BACE1	B-Secretase
MTBD	Microtubule-Binding Domain
BSA	Bovine Serum Albumin
CDK5	Cyclin-Dependent Kinase 5
CFP	Cyan Fluorescent Protein
CLUS	Cluster
CNS	Central Nervous System
CSF	Cerebrospinal Fluid
CTF-β	C-Terminal Fragment
CV	Coefficient Of Variation
CYT	Cytosolic Aggregate
DAPI	4′,6-Diamidino-2-Phenylindole
DMEM	Dulbecco's Modified Eagle′S Medium
DMSO	Dimethyl sulfoxide
DNA	Deoxyribonucleic Acid
DTT	Dithiothreitol
cryoEM	Cryogenic Electron Microscopy
EOAD	Early-Onset Alzheimer's Disease
ER	Endoplasmic Reticulum
FBS	Fetal Bovine Serum
FD	Frontotemporal Dementia
FDG-PET	Fluorodeoxyglucose Positron Emission Tomography
FLD	Frontal Lobe Dementia

FLIM	Fluorescent Lifetime Imaging Microscopy
FP	Fluorescent Protein
FRAP	Fluorescent Recovery After Photobleaching
FRET	Fluorescent Resonance Energy Transfer
FTD	Frontotemporal Dementia
FTDP	Frontotemporal Dementia and Parkinsonism
GSK	Glycogen Synthase Kinase-3B
HD	Huntington Disease
HEK	Human Embryonic Kidney
HEPES	N-2-Hydroxyethylpiperazine-N-2-Ethane Sulfonic Acid
hnRNP	Heterogeneous Nuclear Ribonucleoprotein A1
IDP	Intrinsically Disordered Protein
IDR	Intrinsically Disordered Regions
IF	Immunofluorescent
IHC	Immunohistochemistry
KDEL	Kdel Receptor
KH2PO4	Monopotassium Phosphate
LLPS	Liquid-Liquid Phase Separation
LOAD	Late-Onset Alzheimer's Disease
LPA	Logopenic Progressive Aphasia
LT	Lifetime
MAM	Mitochondria-Associated Er Membranes
MAP	Microtubule Associated Protein
MAPT	Microtubule Associated Protein Tau
MCI	Mild Cognitive Impairment
MD	Mass Density
MEF2	Myocyte Enhance Factor 2
MEM	Minimum Essential Medium
MMSE	Mini-Mental State Examination
MRI	Magnetic Resonance Imaging
MTS	Mitochondria Targeting Sequence
NA	Numerical Aperture
NDD	Neurodegenerative Disease
NE	Nuclear Envelope
NFL	Neurofilament Light
NFT	Neurofibrillary Tangles
NGS	Normal Goat Serum
NMDA	The N-Methyl-D-Aspartate
NPC	Nuclear Pore Complex

NPM	Nucleophosmin
NUC	Nuclear Aggregate
ODT	Optical Diffraction Tomography
PBS	Phosphate-Buffered Saline
PCA	Posterior Cortical Atrophy
PD	Parkinson's Disease
PEG	Polyethylene Glycol
PET	Positron Emission Tomography
PFA	Paraformaldehyde
PHDN1	Phalloidin
PKA	Protein Kinase A
PSEN1	Presenilin 1
PSEN2	Presenilin 2
PSP	Progressive Supranuclear Palsy
PTM	Post-Translational Mutation
R1	Pseudo-Repeat 1
R2020	MATLAB Script
R4	Pseudo-Repeat 4
RAGE	Receptor For Advanced Glycation End Products
RBP	RNA-Binding Proteins
RCM1	Rescan Confocal Microscope
RD	Repeat Domain
RD^{P301S}	Repeat Doman with P301S Mutation
RFP	Red Fluorescent Protein
RI	Refractive Index
RNA	Ribonucleic Acid
ROI	Region Of Interest
ROS	Reactive Oxygen Species
RT	Room Temperature
SD	Standard Deviation
SH-SY5Y	Subline Of Neuroblastoma Cells
STED	Stimulated Emission Depletion Microscopy
TAURD	Tau Repeat Domain
TBS	Tris-Buffered Saline
TC	Tissue Culture
UPR	Unfolded Protein Response
VBM	Voxel-Based Morphometry
YFP	Yellow Fluorescent Protein

Summary

Neurodegenerative diseases (NDDs) encompass a heterogeneous group of chronic neurological disorders characterized by progressive neuron degeneration within specific regions of the central nervous system (CNS). Among these, Alzheimer's disease (AD) stands out as the most prevalent cause of dementia, accounting for approximately 60-80% of all dementia cases. Neuropathologically, AD is marked by the presence of two prominent protein pathological hallmarks: 1) the extracellular accumulation of aggregated amyloid-beta (Aβ) peptides, leading to the formation of amyloid-plaques, and 2) the intracellular aggregation of fibrillar structures composed of neuronal microtubule-associated protein Tau, forming neurofibrillary tangles (NFTs). Despite extensive and prolonged research efforts spanning several decades, the underlying molecular mechanisms of this intricate neurodegenerative condition remain only partially understood.

In this context, the present study employs a well-established HEK sensor cell line, constitutively expressing the aggregation-prone mutant Tau repeat domain fused to either cyan fluorescent protein (CFP) or yellow fluorescent protein (YFP) (TauRDP301S-CFP/YFP). By introducing pre-aggregated Tau forms into these cells, a spectrum of distinct Tau assemblies is generated, encompassing large amorphous cytosolic aggregates (CYT) and amyloid-like structures (AMY), compact cytosolic Tau clusters (CLUS), Tau clusters near the nuclear envelope (NE), and nuclear spherical accumulations (NUC). After determining the sequence of accumulation type occurrence by live cell time-lapse imaging, I characterized the packing density of Tau in the different accumulation types using a multimodal microscopy approach. High-resolution FLIM/FRET microscopy, in which the fluorescent lifetime quenching of CFP serves as a proxy for the packing density of Tau, revealed distinct differences between Tau accumulations, as well as confirming a time-dependent hardening of Tau condensates in vitro.

Optical diffraction tomography (ODT), which measures absolute protein concentration, revealed differences in the molecular and physical density of Tau accumulations. Additionally, it unveiled a drastic restructuring of 24-hour-old Tau

condensates compared to freshly formed 1-hour-old condensates, suggesting the potential transition from soluble Tau to fibrillar Tau aggregates. Lastly, 3D confocal reconstruction microscopy and StED microscopy provided insight into the precise positioning of different Tau accumulations regarding cytoskeletal fibers and cellular landmark organelles, such as the nuclear envelope and the endoplasmic reticulum (ER), revealing multiple interaction partners of Tau and implying possible downstream effects of Tau on cellular processes and mechanisms.

By employing various light microscopy techniques, insights into Tau aggregation at different stages was gained, contributing to a deeper understanding of Tau aggregation formation and its implications for cellular processes. Furthermore, ODT emerged as a valuable tool for studying Tau aggregation in both cellular environments and in vitro conditions, revealing new structural insights. This research may offer prospects for understanding Tau transition and potential drug development.

Zusammenfassung:

Neurodegenerative Erkrankungen (NDDs) umfassen eine heterogene Gruppe chronischer neurologischer Störungen, die durch den progressiven Abbau von Neuronen in spezifischen Regionen des zentralen Nervensystems (ZNS) gekennzeichnet sind. Unter diesen ist die Alzheimer-Krankheit (AD) als häufigste Ursache von Demenz besonders hervorzuheben und macht etwa 60-80% aller Demenzfälle aus. Neuropathologisch ist die AD durch zwei prominente pathologische Proteine gekennzeichnet: 1) die extrazelluläre Ablagerung von aggregierten Amyloid-Beta (Aβ) -Peptiden, die zur Bildung von Amyloid-Plaques führen, und 2) die intrazelluläre Aggregation von faserförmigen Strukturen des neuronalen Mikro Tubulin-assoziierten Proteins Tau, die Neurofibrillenbündel (NFTs) bilden. Trotz umfangreicher und langjähriger Forschungsbemühungen über mehrere Jahrzehnte hinweg sind die zugrunde liegenden molekularen Mechanismen dieses komplexen neurodegenerativen Zustands nur teilweise verstanden.

In diesem Zusammenhang verwendet die vorliegende Studie eine etablierte HEK-Sensorzelllinie, die konstitutiv das aggregationsanfällige mutierte Tau-Tandemrepeats fusioniert mit entweder Cyanfluoreszenzprotein (CFP) oder Gelbfluoreszenzprotein (YFP) (TauRDP301S-CFP/YFP) exprimiert. Durch die Einführung voraggregierter Tau-Formen in diese Zellen entsteht eine Vielzahl von unterschiedlichen Tau-Assemblierungen, darunter große amorphe zytoplasmatische Aggregate (CYT) und Amyloid-ähnliche Strukturen (AMY), kompakte zytoplasmatische Tau-Cluster (CLUS), Tau-Cluster in der Nähe der Kernhülle (NE) und nukleäre kugelförmige Ansammlungen (NUC). Nachdem die Abfolge des Auftretens der Ansammlungstypen durch konfokale Echtzeitmikroskopie der Zellen ermittelt wurde, wurde die Packungsdichte von Tau in den verschiedenen Ansammlungstypen mithilfe eines multimodalen Mikroskopie-Ansatzes charakterisiert. Die hochauflösende FLIM/FRET-Mikroskopie, bei der die Fluoreszenzlebensdauer von CFP als Proxy für die Packungsdichte von Tau dient,

enthüllt deutliche Unterschiede zwischen den Tau-Akkumulationen und bestätigt gleichzeitig eine zeitabhängige Verfestigung der Tau-Kondensate in vitro.
Die optische Beugungstomographie (ODT), die die absolute Protein-Konzentration misst, enthüllt Unterschiede in der molekularen und physischen Dichte der Tau-Akkumulationen. Außerdem deckt sie eine drastische Umstrukturierung der 24 Stunden alten Tau-Kondensate im Vergleich zu frisch gebildeten 1-Stunden alten Kondensaten auf, was auf den potenziellen Übergang von löslichem Tau zu faserförmigen Tau-Aggregaten hindeutet. Schließlich liefert 3D-Konfokalrekonstruktionsmikroskopie und StED-Mikroskopie Einblicke in die genaue Positionierung verschiedener Tau-Akkumulationen in Bezug auf das Zytoskelett und zelluläre markante Organellen wie die Kernhülle und das endoplasmatische Retikulum (ER), wobei mehrere Interaktionspartner von Tau enthüllt werden und mögliche nachgeschaltete Auswirkungen von Tau auf zelluläre Prozesse und Mechanismen angedeutet werden.
Durch den Einsatz verschiedener Lichtmikroskopie-Techniken kann ein Einblick in die Tau-Aggregation in verschiedenen Stadien gewonnen werden und so zu einem tieferen Verständnis der Bildung der Tau-Akkumulationen und ihrer Auswirkungen auf zelluläre Prozesse beitragen. Darüber hinaus erweist sich die ODT-Mikroskopie als wertvolles Instrument zur Untersuchung der Tau-Aggregation sowohl in zellulärer Umgebung als auch unter in vitro Bedingungen, und enthüllt neue strukturelle Erkenntnisse. Diese Forschung kann zukünftig zu einem besseren Verständnis des Übergangs von Tau führen und möglicherweise zur Entwicklung neuer Arzneimittel beitragen.

3 Introduction

Neurodegenerative diseases (NDDs) comprise a diverse group of chronic and progressive neurological disorders characterized by the selective degeneration and loss of neurons in specific regions of the central nervous system (CNS). These devastating conditions have become a major public health concern worldwide due to their high prevalence and significant impact on the aging population. NDDs encompass a wide range of disorders, including Alzheimer's disease (AD), Parkinson's disease (PD), amyotrophic lateral sclerosis (ALS), Huntington's disease (HD), and frontotemporal dementia (FTD), among others. The prevalence of NDDs is steadily increasing, driven by the aging demographics of many societies. Epidemiological studies estimate that the incidence of NDDs is expected to rise in the coming decades, posing substantial challenges to healthcare systems and society. The pathogenesis of NDDs remains complex and multifactorial, involving intricate interactions between genetic, environmental, and lifestyle factors. Despite extensive research efforts, the precise etiology and molecular mechanisms underlying these diseases are yet to be fully elucidated.

The deposition of protein aggregates in the brain is a unifying pathological hallmark of NDDs. AD is the most common cause of dementia, accounting for 60-80% of all dementia cases. Other forms of dementia include vascular dementia, dementia with Lewy bodies, frontotemporal lobar degeneration, Parkinson's disease, and mixed dementia types (Hippius & Neundörfer, 2003). The global prevalence of dementia was approximately 50-65 million people in 2019, with AD accounting for approximately 74% of all cases (Nichols et al., 2022). Due to the world's aging population, it is projected that the number of people with dementia will triple by 2050(Herbert et al., 2013). However, despite decades of intensive research, there is currently no curative treatment for AD, with current treatments only providing symptomatic relief in the early stages of the disease (J. Cummings et al., 2022).

3.1 Alzheimer's disease

3.1.1 Symptoms, pathology, and disease progression

AD was first described by Alois Alzheimer in 1906 when he presented his findings of his 50-year-old patient's condition as "A peculiar severe disease process of the cerebral cortex" (ALZHEIMER, 1906; Hippius & Neundörfer, 2003). Based on Alois Alzheimer's finding, AD is now characterized by abnormal protein accumulation in the central nervous system (CNS), resulting in the death of neurons (Stelzmann et al., 1995). The risk of developing AD is influenced by both genetic and environmental factors, with age being the most significant risk factor (Norton et al., 2014). Other risk factors include a family history of the disease, head injury, depression, and cardiovascular disease (Norton et al., 2014). Several genes have been identified as risk factors for AD, including the APOE ε4 allele, which is associated with a greater risk of developing the disease in both early- and late-onset cases (Karch & Goate, 2015).

AD is characterized by progressive cognitive and behavioral deficits, leading to a decline in daily functioning ("2023 Alzheimer's Disease Facts and Figures," 2023). Common symptoms include memory loss, language difficulties, impaired visual-spatial skills, disorientation, mood swings, and behavioral changes ("2023 Alzheimer's Disease Facts and Figures," 2023). Clinically, the disease progresses slowly, beginning with mild AD and advancing to a moderate and finally severe phase. Mild cognitive impairment (MCI) is a distinct diagnosis for individuals with cognitive impairment that exceeds normal aging deterioration, but do not necessarily progress to dementia (Tilley et al., 1998) Individuals in these early stages of AD experience memory gaps, misplace objects, or have difficulties finding words. People with moderate AD, on the other hand, require more care as they begin to have difficulties recognizing family members, learning new tasks, and experiencing personality changes (Tilley et al., 1998). In late phases of AD, patients are dependent on all-round care as even many normal physiological functions cannot be controlled ("2023 Alzheimer's Disease Facts and Figures," 2023). AD is ultimately fatal, with AD-related pneumonia being the leading cause of death as patients

become vulnerable to infections when movements are impaired. Additionally, difficulties with swallowing lead to malnutrition and dehydration (Tilley et al., 1998). The clinical phase of AD lasts, on average, nine years, but only represents the final one-third of the entire disease process, as molecular changes can be detected up to 20 years before the onset of clinical symptoms (Jack et al., 2013; Khanahmadi et al., 2015).

Neuropathologically, two main protein pathological hallmarks can be found in the AD brain: i) the extracellular deposition of aggregated amyloid-beta (A-beta) peptides in amyloid-plaques and ii) the intracellular accumulation of fibrillar aggregates of the neuronal microtubule associates protein Tau in neurofibrillary tangles (NFTs). The correlation between disease progression and neuroanatomical pattern of pathological protein aggregates was first described by Braak & Braak (Braak & Braak, 1991, 1995).Whereas amyloid-plaque pathology appears brain-wide and intensifies with disease progression, the progressive occurrence of NFTs follows a certain neuroanatomical pattern and correlates with clinical disease progression ("2023 Alzheimer's Disease Facts and Figures," 2023; Jack et al., 2013; Khanahmadi et al., 2015; Tilley et al., 1998)

3.1.2 Forms of AD

AD is a complex neurodegenerative disorder that is primarily considered a single disease entity. However, different forms of AD have been identified based on their underlying molecular pathology and clinical presentation. Understanding the different forms of AD is crucial for developing targeted therapies and effective interventions for this devastating disease. The so called Early-onset AD (EOAD) refers to cases of AD that occur before the age of 65. EOAD is less common than late-onset AD (LOAD) (less than 10% of all cases) ("2023 Alzheimer's Disease Facts and Figures," 2023) but tends to have a more rapid progression and a more severe cognitive decline. EOAD is often associated with genetic mutations, and several genes have been identified as causative or risk factors for this form of the disease, including amyloid precursor protein (APP), presenilin 1 (PSEN1), and presenilin 2

(PSEN2) (Tanzi & Bertram, 2005). EOAD is also associated with increased levels of amyloid-β (Aβ) peptide and tau protein in the brain, which are the hallmark pathological features of AD.

On the other hand, LOAD is the most common form of AD, accounting for over 95% of all cases ("2021 Alzheimer's Disease Facts and Figures," 2021). LOAD is typically diagnosed after the age of 65, and its clinical presentation is characterized by a gradual decline in cognitive and functional abilities. LOAD is a multifactorial disease, with both genetic and environmental factors contributing to its pathogenesis. The most significant genetic risk factor for LOAD is the apolipoprotein E (APOE) ε4 allele, which is associated with an increased risk of developing the disease and a more severe cognitive decline (Roses, 1996). LOAD is also associated with the accumulation of Aβ and tau protein in the brain, which lead to the formation of amyloid plaques and neurofibrillary tangles, respectively (Selkoe, 2011).

In addition to EOAD and LOAD, there are several atypical forms of AD that have been identified based on their clinical presentation and underlying pathology. These include posterior cortical atrophy (PCA), which is characterized by visual deficits and posterior cortical atrophy on neuroimaging; logopenic progressive aphasia (LPA), which is characterized by language deficits and temporal-parietal atrophy on neuroimaging; and frontal variant AD (FvAD), which is characterized by behavioral and executive function deficits and frontal lobe atrophy on neuroimaging (Migliaccio et al., 2015). These atypical forms of AD are typically associated with different patterns of Aβ and tau accumulation in the brain, and understanding their underlying pathology is crucial for developing targeted treatments and interventions.

3.1.3 Diagnosis

Usually, a diagnosis of AD is established through a comprehensive physical and neurological examination, which may involve various tests, including assessments of cognitive abilities such as the Mini-Mental Examination (MMSE (Arevalo-Rodriguez et al., 2015)). Nevertheless, accurately diagnosing AD can be challenging since the symptoms may overlap with those of other types of dementia. Hence, confirming the diagnosis of AD typically requires analyzing postmortem tissue through histological examination (Braak & Braak, 1991).

Nevertheless, there are many different methods and techniques available to diagnose AD at different stages of the disease (Fig 1). Such include cerebrospinal fluid (CSF) analysis of Aβ, and tau proteins is considered one of the most reliable diagnostic tools for AD (Palmqvist et al., 2019). In addition to decreased levels of $A\beta_{42}$ and increased levels of tau, other CSF biomarkers that may aid in the diagnosis of AD include phosphorylated tau (p-tau) and neurofilament light (NFL) protein (J. L. Cummings & Cole, 2002). However, CSF analysis is an invasive procedure that can be uncomfortable for patients and may carry a risk of infection.

Amyloid positron emission tomography (PET) imaging is a non-invasive imaging technique that can detect amyloid plaques in the brain. Studies have shown that amyloid PET imaging can accurately distinguish between individuals with and without AD-related amyloid pathology (Rowe et al., 2010). However, amyloid PET imaging is expensive and not commonly available.

FDG-PET is another imaging technique that can aid in the diagnosis of AD by detecting changes in brain metabolism. Hypometabolism in the temporoparietal cortex and posterior cingulate cortex, two brain regions important for memory and cognition, are commonly observed in patients with AD (Minoshima et al., 1997). However, FDG-PET is less sensitive and less specific than amyloid PET imaging.

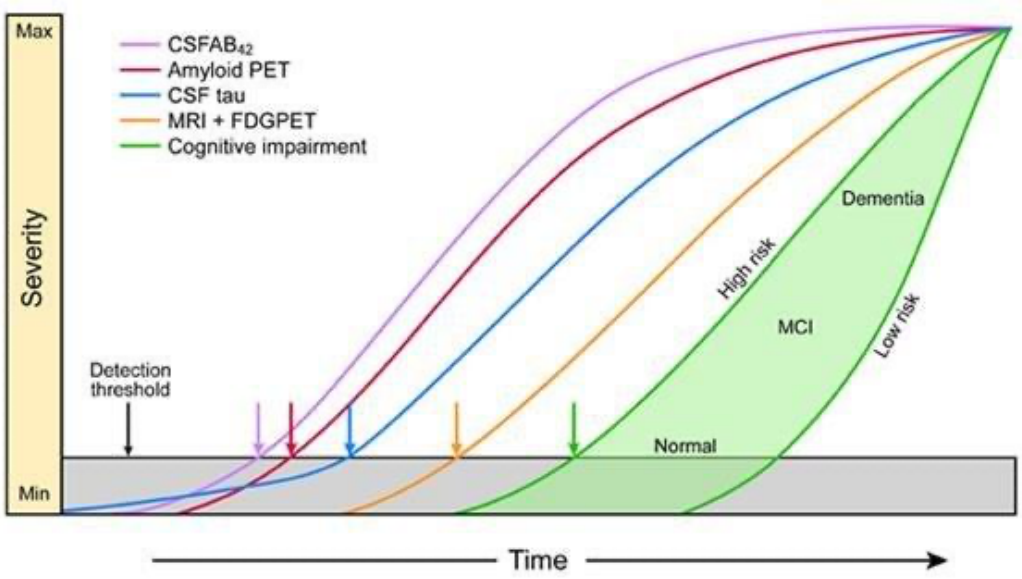

Figure 1. Schematic of AD progression and detection methods. Schematic illustration showing timepoints of detection methods used to diagnose AD. (pink) CSF extraction and analysis for AB42 is the earliest method of detection, yet very painful for the patient. (red) Amyloid PET imaging allows visualization of plaques early on. (blue) CSF extraction and analysis for Tau allows for a rather early detection during early onset. (yellow) MRI+FDGPET is a very informative and precise detection method, however it is not very specific to AD and could also lead to diagnosis of other form of dementia. (Image from Khanahmadi et al., 2015[10])

Magnetic resonance imaging (MRI) is a non-invasive imaging technique that can detect structural changes in the brain, such as hippocampal atrophy, which is a hallmark of AD (Jack et al., n.d.). Voxel-based morphometry (VBM), a technique used to analyze MRI data, has been used to identify correlations between neurofibrillary tangle pathology and atrophy in specific brain regions (Frisoni et al., 2007). However, structural changes detected by MRI may not be specific to AD and may also be observed in other neurodegenerative disorders.

In summary, a combination of clinical evaluation, CSF analysis, neuroimaging, and other biomarker tests can aid in the diagnosis of AD. While each diagnostic method has its advantages and limitations, the use of multiple diagnostic tools can increase the accuracy of AD diagnosis and aid in early detection.

3.1.4 Treatment

Currently, the available treatments for AD primarily focus on managing the symptoms and include cholinesterase inhibitors (e.g., donepezil, rivastigmine, galantamine) and an NMDA receptor antagonist called memantine. These medications aim to enhance neurotransmitter signaling and regulate glutamate activity to improve cognitive symptoms in AD patients (J. Cummings et al., 2014).

However, these symptomatic treatments have limited efficacy and do not address the underlying disease process. To advance AD treatment, researchers are actively exploring novel therapeutic approaches in clinical trials. One promising avenue is the development of disease-modifying therapies targeting the key pathological features of AD.

A major target of disease-modifying therapies is the reduction of amyloid-beta plaques. Recently, several anti-amyloid antibodies - such as aducanumab, gantenerumab, and solanezumab - have been developed that selectively bind and remove amyloid-beta from the brain. Clinical trials are assessing their efficacy in slowing down cognitive decline and disease progression (J. Cummings et al., 2022).

Another critical aspect of AD pathology is the abnormal phosphorylation and aggregation of Tau protein. Tau-directed immunotherapy and small molecule inhibitors are being investigated to prevent or reduce Tau aggregation and its subsequent detrimental effects on neuronal function.

Furthermore, emerging research focuses on addressing neuroinflammation, oxidative stress, and synaptic dysfunction in AD. Anti-inflammatory agents, antioxidants, and drugs that enhance synaptic function are being evaluated for their potential neuroprotective effects and their ability to mitigate disease progression (Long & Holtzman, 2019).

Despite the considerable efforts in AD research, several clinical trials targeting amyloid-beta and Tau have faced challenges and produced mixed outcomes. Factors such as patient selection, treatment timing, and the complexity of AD pathology contribute to the complexities of developing effective therapies. Ongoing research aims to optimize treatment strategies, identify reliable biomarkers for early

detection and monitoring, and explore combination therapies to maximize the potential benefits of treatment in AD (J. Cummings et al., 2022).

3.2 Pathological hallmarks in the AD brain

The etiology of AD is still not completely understood. However, two hallmark structures that are always present in the disease are extracellular plaques of Aβ peptide and hyperphosphorylated intracellular fibrillar bundles of Tau, known as neurofibrillary tangles (NFTs) (Bamburg & Bloom, 2009) (Figure 2).

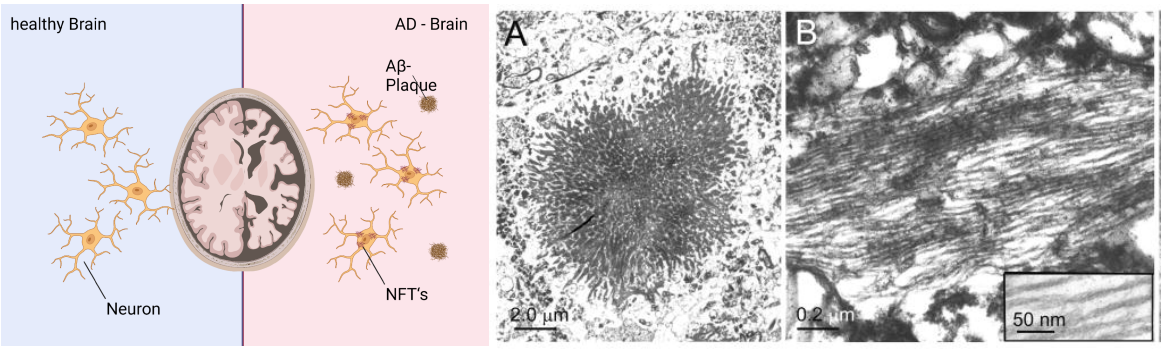

Figure 2. Pathological hallmarks of Alzheimer Disease. (A) Schematic illustration of a healthy brain (left) compared to an AD brain showing extracellular amyloid-beta aggregates (Aβ-plaques) and intracellular Tau aggregates (NFTs) (Illustration is adapted from https://www.asceneuron.com/alzheimers-disease). (B) Electron microscopy images of Aβ-plaques (left) and neurofibrillary tangles (right). (Images taken from Bamburg & Bloom, 2009)[18].

Aβ plaques are extracellular deposits of aggregated Aβ protein that accumulate in the brain. Aβ is a peptide that is produced from a larger protein called amyloid precursor protein (APP) through the action of two enzymes, beta-secretase, and gamma-secretase (Selkoe, 2011).

NFTs are intracellular aggregates of hyperphosphorylated tau protein that accumulate within the neuronal cytoplasm and processes, leading to neuronal dysfunction and cell death (Götz & Ittner, 2008). Tau is a microtubule-associated protein that stabilizes microtubules, which are critical for neuronal transport and signaling (Iqbal et al., 2016). In AD, tau becomes hyperphosphorylated and

aggregates into NFTs, leading to the destabilization of microtubules and the disruption of neuronal transport and signaling (Selkoe, 2011). This results in synaptic dysfunction and neuronal death, which are critical pathological features of AD (Jack et al., 2013).

Thus, these structures also categorize Alzheimer's disease as an amyloidosis, which is characterized by the aggregation of usually soluble proteins into insoluble proteinaceous -sheet-rich fibrils(Balupuri et al., 2020). It is believed that the formation of these Aβ- plaques from the amyloid peptide in the extracellular space causes neuronal cell death due to interruption of synaptic communication between neurons. Additionally, the intracellular forming NFT´s from hyperphosphorylated Tau interrupts the intracellular nutrient transport which leads to malnourishment of the cell, contributing to the pathology of AD (“2023 Alzheimer’s Disease Facts and Figures,” 2023).

In addition to Aβ plaques and NFTs, other hallmarks of AD include neuroinflammation, oxidative stress, and mitochondrial dysfunction. Neuroinflammation is a key component of AD pathology and is characterized by the activation of microglia and astrocytes, which can contribute to neuronal damage and exacerbate Aβ deposition and tau pathology (Jack et al., 2010; Reiman et al., 2012). Oxidative stress, which results from an imbalance between reactive oxygen species (ROS) and antioxidants, is also implicated in AD pathology and can lead to damage of lipids, proteins, and nucleic acids (Jack et al., 2010; Reiman et al., 2012). Mitochondrial dysfunction is also a hallmark of AD and is characterized by decreased mitochondrial function and energy production, which can contribute to neuronal dysfunction and cell death (Jack et al., 2010; Reiman et al., 2012).

Overall, the accumulation of Aβ plaques and NFTs, along with neuroinflammation, oxidative stress, and mitochondrial dysfunction, contribute to the complex and progressive pathology of AD.

3.2.1 A-beta plaques

3.2.1.1 The A-beta peptide

APP is a transmembrane protein that is ubiquitously expressed throughout the body, with particularly high levels found in the brain. The exact function of APP remains unclear, although it is thought to play a role in neuronal growth and repair, as well as synaptic function and plasticity (Thinakaran & Koo, 2008). APP is processed by two enzymatic pathways, non-amyloidogenic and amyloidogenic, resulting in the formation of different peptides, including the Aβ peptide (Zheng & Koo, 2011).
The non-amyloidogenic pathway is the primary processing pathway for APP in neurons. In this pathway, APP is cleaved by the α-secretase enzyme within the Aβ domain, resulting in the release of a soluble N-terminal fragment (sAPPα) and a membrane-bound C-terminal fragment (CTFα) (Thinakaran & Koo, 2008). sAPPα is involved in several physiological processes including synapse formation and repair, neuronal survival, and learning and memory (Hick et al., 2015). CTFα is further cleaved by γ-secretase within the transmembrane domain of APP, resulting in the production of p3, a shorter and less amyloidogenic fragment (Hick et al., 2015). The non-amyloidogenic pathway is thought to be a protective pathway, as it results in the production of sAPPα and p3, which have been shown to have neuroprotective effects and do not contribute to the formation of toxic Aβ oligomers or plaques (Tackenberg & Nitsch, 2019).

On the other hand, in the amyloidogenic pathway, APP is cleaved first by β-secretase (BACE1) (Vassar et al., 1999) within the extracellular domain of APP, generating a soluble N-terminal fragment (sAPPβ) and a C-terminal fragment (CTFβ). CTFβ is then further cleaved by γ-secretase, resulting in the production of the Aβ peptide (Selkoe & Hardy, 2016). Aβ is released into the extracellular space and can form aggregates and plaques, which are thought to be a major cause of neuronal damage in Alzheimer's disease (Hardy & Selkoe, 2002).
However, recent research has also suggested that Aβ may play a role in normal physiological processes in the brain.

As mentioned above Aβ can also have protective functions. It has been shown for example that Aβ has neuroprotective properties, such as antioxidant activity and the ability to modulate synaptic plasticity (Puzzo & Arancio, 2013). Aβ has also been shown to play a role in the regulation of cerebral blood flow (Zlokovic, 2011). Aβ has been found to bind to the receptor for advanced glycation end products (RAGE) on endothelial cells and stimulate the production of nitric oxide, which in turn induces vasodilation and increases cerebral blood flow. In addition, Aβ has been shown to have antimicrobial properties, particularly against bacteria and fungi (D. K. V. Kumar et al., 2016). This suggests that Aβ may play a role in the innate immune response in the brain.

Thus, while the amyloidogenic processing of APP leading to the formation of Aβ plaques is a hallmark of Alzheimer's disease, it is important to understand the complex physiological roles of Aβ in the brain beyond its pathological effects.

3.2.1.2 Formation of A-beta aggregates

Amyloid beta (Aβ) aggregation is a complex process that occurs through multiple steps, involving conformational changes, nucleation, growth, and fibril elongation. The exact molecular mechanisms underlying Aβ aggregation formation are not yet fully understood, but recent biophysical studies have provided insights into the molecular events that drive the process (Balupuri et al., 2020; Harper et al., 1997; Meisl et al., 2016; Tycko, 2011).

The initial step in Aβ aggregation is the formation of unfolded Aβ monomers, which are produced through the above mentioned amyloidogenic and non-amyloidogenic pathways. Aβ peptides can exist in different isoforms, with Aβ42 being the most prone to aggregation and the most abundant in the amyloid plaques of AD patients. Under physiological conditions, Aβ monomers are predominantly unstructured or adopt a random coil conformation (Masters et al., 1985). However, under certain conditions such as low pH, high temperature, or the presence of other molecules,

Aβ monomers can undergo a conformational change and adopt a β-sheet structure that is prone to aggregation (S. Kumar & Nussinov, 2002; Pellarin & Caflisch, 2006). The next step in Aβ aggregation is the nucleation phase, where a small population of Aβ monomers undergo a conformational change and form a nucleus that can recruit additional Aβ monomers. Nucleation is believed to be the rate-limiting step of the aggregation process (Chatani & Yamamoto, 2018; Linse et al., 2007). The formation of a stable nucleus is critical for subsequent aggregation and can be influenced by factors such as pH, temperature, and ionic strength (Lü hrs et al., 2005; McParland et al., 2000). Once a stable nucleus is formed, it can rapidly grow by adding additional Aβ monomers, leading to the formation of oligomers, protofibrils, and eventually fibrils (Shankar et al., 2008; Tycko, 2011; Walsh et al., 2002). This step is called the Elongation-phase.

Oligomers are intermediate structures in the aggregation process, consisting of a small number of Aβ monomers that are loosely connected. Oligomers are believed to be the most neurotoxic species, causing synaptic dysfunction and neuronal death (Haass & Selkoe, 2007; Mucke et al., 2000). Protofibrils are larger aggregates of Aβ monomers that are more structured than oligomers and have a higher propensity to aggregate further (Soto, 2003). Fibrils are the product of Aβ aggregation, consisting of long, unbranched, and insoluble structures that form the characteristic amyloid plaques observed in AD (Klein et al., 2001; Selkoe, 2001).

3.2.2 The amyloid cascade hypothesis

In 1992, Hardy and Higgins proposed the amyloid cascade hypothesis as an attempt to unify the characteristic hallmarks and symptoms of Alzheimer's disease (AD) and provide an overall hypothesis for the progression of molecular events in AD pathology (Hardy & Higgins, 1992). The hypothesis posits that the deposition of the Aβ peptide in the brain is the primary causative agent of Alzheimer's pathology, and the formation of tau neurofibrillary tangles and cell loss are downstream events resulting from Aβ deposition (Figure 3). This concept was significant in subsequent

years for the focus of AD research and has been further developed since (Selkoe, 1991)

Aβ peptides are highly prone to aggregation and can form oligomers, protofibrils, and eventually insoluble fibrils that deposit into extracellular plaques in the brain (Ittner & Götz, 2011). The accumulation of these plaques is one of the hallmark features of AD pathology.

The accumulation of Aβ peptides in the brain can also trigger neuroinflammation by activating microglia and astrocytes, which release pro-inflammatory cytokines and free radicals that can damage neurons (Morris et al., 2011). Additionally, Aβ peptides can impair synaptic function by disrupting the interaction between neurons and interfering with the normal function of synaptic proteins (Wang & Mandelkow, 2016). Moreover, the amyloid cascade hypothesis suggests that Aβ peptides can induce the hyperphosphorylation of tau, leading to the formation of NFTs. Tau is a microtubule-associated protein that plays a critical role in maintaining the structure and stability of neuronal microtubules. In AD, tau becomes hyperphosphorylated, leading to its detachment from microtubules, aggregation into NFTs, and ultimately causing neuronal dysfunction and degeneration (Querfurth & LaFerla, 2010). The accumulation of Aβ and the formation of NFTs can disrupt several cellular processes, including intracellular transport, energy metabolism, and synaptic plasticity, leading to the widespread degeneration of neurons in the brain (Shankar et al., 2008).

In conclusion, the amyloid cascade hypothesis provides a comprehensive explanation of the pathological processes that occur in AD. The accumulation of Aβ peptides initiates a cascade of events that lead to neuronal dysfunction and degeneration, ultimately leading to the clinical symptoms of AD. The role of tau in AD is also essential, as the hyperphosphorylation and aggregation of tau lead to the formation of NFTs, which contribute significantly to neuronal dysfunction and degeneration.

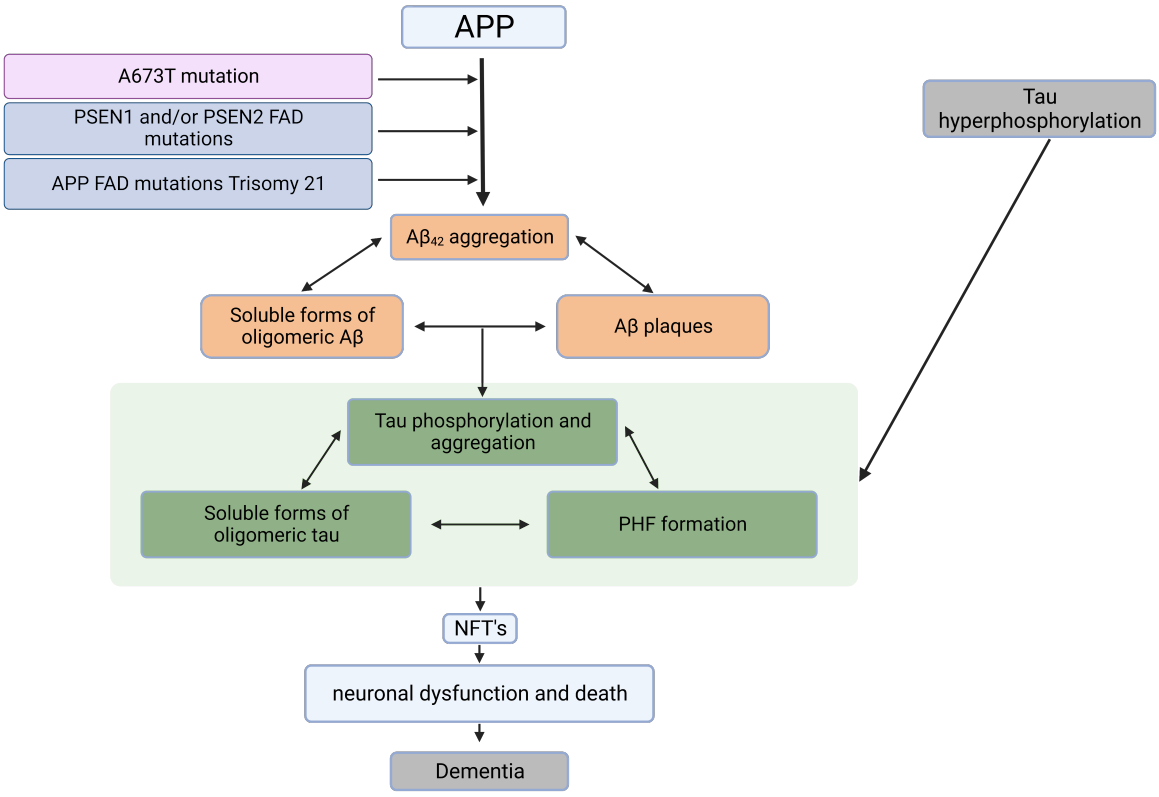

Figure 3. The amyloid cascade hypothesis.
According to the Amyloid Cascade Hypothesis, the aggregation of amyloid beta (Aβ) peptides is a key event in the pathogenesis of Alzheimer's disease. As Aβ peptides accumulate, they can form extracellular plaques, which may cause the parallel dysfunction of Tau protein. Once a certain threshold of Aβ is reached, Tau protein is believed to spread through the brain, promoting the accelerated deterioration of neuronal cells and leading to cognitive impairment and dementia. (Image taken from Karran & De Strooper, 2016[162]).

3.2.3 Neurofibrillary tangles

3.2.3.1 The microtubule associated protein Tau (MAPT)

Given that Alzheimer's disease is characterized by two hallmark features, it is becoming increasingly evident that Tau plays a pivotal role in the pathogenesis of this neurodegenerative disorder. Therefore, comprehending the precise function and impact of Tau in normal physiological processes and pathological conditions is of utmost importance to gain deeper insights into the pathophysiology of Alzheimer's disease.

Tau is a microtubule-associated protein (MAP) that plays a role in the structure and function of neurons. The human MAPT gene located on chromosome 17q21.31 encodes for Tau (Andreadis, 2005). It spans over 100 kb and consists of 16 exons that undergo complex alternative splicing, resulting in the expression of six different isoforms (ranging from 352-441 amino acids) of Tau in the adult human brain (Figure 4) (T. Guo et al., 2017; Hutton et al., 1998). Tau protein can be divided into four distinct regions: a lengthy and flexible N-terminus (~250 amino acids), a proline-rich region of considerable length, a microtubule-binding domain (MTBD) that consists of four pseudo-repeats (R1-R4), and a relatively shorter C-terminus (~40 amino acids). Due to its lack of a well-defined three-dimensional structure, tau is classified as an intrinsically disordered protein (IDP), which grants it the ability to perform diverse functions (Wright & Dyson, 2015).

The six isoforms are distinguished by the presence or absence of exon 2, 3, or 10. The isoforms with all three exons are referred to as 3R (containing three repeats of the MTBD) and those without exon 10 as 4R (containing four repeats). Specifically, 3R isoforms are more abundant in the adult human brain than 4R isoforms, whereas in the fetal brain, both isoforms are expressed at similar levels (Goedert & Jakes, 1990; Kosik et al., 1988).

The differential expression of Tau isoforms is important for the proper functioning of neurons. Studies have shown that the ratio of 3R to 4R isoforms can affect the stability and dynamics of microtubules, with higher levels of 3R isoforms promoting microtubule stability, while higher levels of 4R isoforms promote microtubule flexibility (Kolaczkowska & Kubes, 2013; Y. Wang & Mandelkow, 2016). Furthermore, the dysregulation of the 3R/4R ratio has been implicated in neurodegenerative diseases, such as AD and frontotemporal dementia (FD) (Andreadis, 1992; Hutton & Hardy, 1997)

The expression of Tau is tightly regulated by multiple factors, including transcription factors, splicing factors, and microRNAs (Kou et al., 2020). For instance, transcription factors such as specificity protein 1 (SP1) and myocyte enhancer factor 2 (MEF2) have been shown to regulate the expression of Tau (Brusco & Haas, 2015; Schindowski et al., 2006). Splicing factors such as heterogeneous nuclear

ribonucleoprotein A1 (hnRNP A1) and the serine/arginine-rich (SR) proteins also play a role in the alternative splicing of Tau exons (Kanai & Hirokawa, 1995). Furthermore, several microRNAs have been identified that regulate the expression of Tau, including miR-132, miR-9, and miR-34c (Noble et al., 2005; Qian et al., 2010).

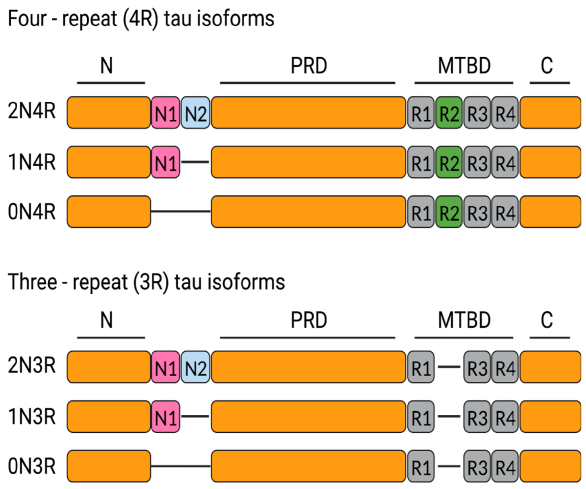

Figure 4. Alternative splicing of Tau protein in the human CNS.
Tau isoforms are produced in the human CNS by alternative splicing of the MAPT gene. Exons 2 and 3 in the N-terminal region of tau encode distinct amino acid sequences that are either excluded (0N) or differently inserted, resulting in 1N (exon 2) or 2N (exons 2 and 3) tau isoforms. The proline-rich domain (PRD) is in the center of tau. Exon 10 in the microtubule binding domain (MTBD) alternative splicing leads in 3R or 4R tau isoforms. All six human CNS tau isoforms share the C-terminal region (Illustration adapted from Guo, Noble & Hanger,2017[73]).

3.2.3.2 The physiological role of Tau

As part of the MAP family, Tau´s primary role is to stabilize and support microtubules, which are the primary component of the cytoskeleton, and to promote their assembly and organization (Goedert & Spillantini, 2006). Microtubules are essential for the maintenance of cell shape, the establishment and maintenance of cell polarity, and the regulation of intracellular transport (Hirokawa et al., 2009). Tau interacts with microtubules by binding to tubulin subunits, the building blocks of microtubules. This interaction is crucial for microtubule assembly, stability, and dynamics, and is regulated by post-translational modification of Tau.

Tau binds to the microtubule lattice through its microtubule binding domain (MTBD), which consists of four imperfect repeats. Each repeat has a conserved hexapeptide motif that interacts with the αβ-tubulin dimer. Studies have suggested that each Tau molecule interacts with 2-4 tubulin dimers, bridging them together and promoting the assembly of the microtubule (Drechsel et al., 1992). The binding of Tau to microtubules has also been shown to increase the rigidity and mechanical stability

of the microtubule lattice, which is important for the maintenance of neuronal morphology (Figure 5) (A. Rai et al., 2011).

The interaction between Tau and tubulin is regulated by various factors. For example, the isoforms of tubulin that make up the microtubule can affect Tau binding. Recent studies have demonstrated that certain tubulin isoforms, such as tubulin containing the α6A isoform, bind Tau more strongly than other isoforms (Bachmann et al., 2021). Additionally, Tau phosphorylation, a common post-translational modification of Tau, can regulate its binding to microtubules. Phosphorylation of certain residues on Tau has been shown to decrease its binding affinity for microtubules (Sengupta et al., 1998).

In addition to stabilizing microtubules Tau also has a regulatory effect on the active transport along the microtubules by interacting with motor proteins such as kinesin and dynein (Dixit et al., 2008; Mandelkow et al., 1992).

Kinesin and dynein are two key motor proteins that move along microtubules and are responsible for intracellular transport of a variety of cargo, including organelles, vesicles, and protein complexes. Studies have demonstrated that Tau can directly interact with kinesin and dynein and modulate their binding to microtubules (B. Trinczek*, 1999; Dixit et al., 2008). For example, Tau has been demonstrated to improve binding affinity of kinesin to microtubules and enhance the processivity of kinesin-mediated transport (Ebneth et al., 1999; Panda et al., 2003). Conversely, Tau has also been shown to inhibit the binding of dynein to microtubules and reduce the processivity of dynein-mediated transport.

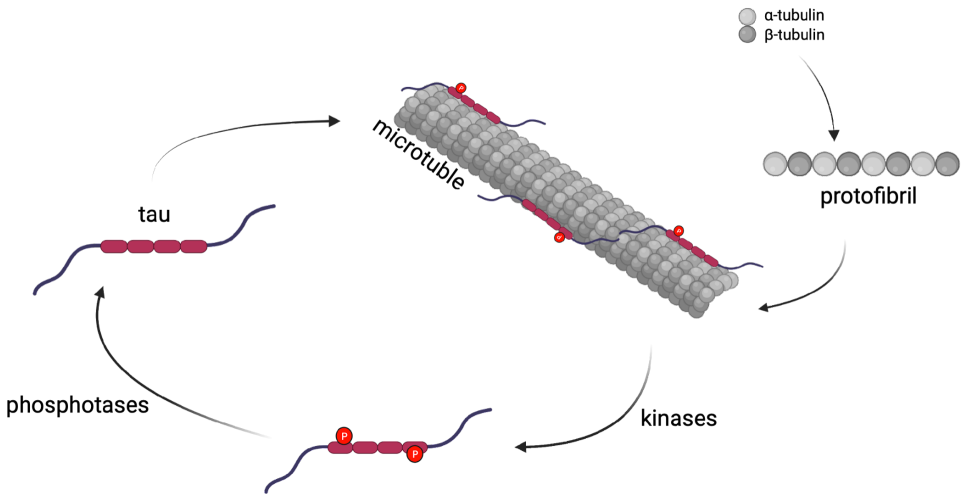

Figure 5. Tau's role in microtubule dynamics under healthy conditions.
α/β-tubulin heterodimers–assemble into MT protofibrils, which eventually become microtubules. Phosphorylated Tau binds the microtubules to increase the stability and rigidity. (Image adapted from Bodea, Eckert & Götz,2016[163]).

Beyond its role in microtubule stabilization and transport regulation, Tau has also been implicated in other physiological functions. For example, it has been suggested that Tau plays a role in regulating neuronal migration during brain development (Morris et al., 2011). Tau has also been implicated in the regulation of synaptic function, and in the modulation of signal transduction pathways in response to extracellular signals (Ittner et al., 2010).

Furthermore, it has been shown that Tau plays a regulatory role in nuclear transport. Tau can shuttle between the nucleus and cytoplasm, and has been shown to interact with nucleoporins, the proteins that make up the nuclear pore complex, which regulates the transport of macromolecules in and out of the nucleus (Eftekharzadeh et al., 2018; Tripathi et al., 2019).

The role of Tau in nuclear transport is an active area of research, and its dysregulation has been implicated in various neurodegenerative diseases. For example, altered Tau localization and nuclear transport has been observed in the brains of individuals with AD and FLD (Ittner et al., 2010).

3.2.3.3 Tau post-translational modifications

The different functions of Tau are highly regulated through post-translational modifications, including phosphorylation, acetylation, glycosylation, and ubiquitination (Alquezar et al., 2021). These modifications have a profound effect on Tau's ability to interact with microtubules, and on its physiological function. Phosphorylation of Tau is a critical regulatory mechanism that is involved in modulating the binding affinity of Tau to microtubules (Biernat et al., 1992; Mandelkow & Mandelkow, 2011).

Tau is phosphorylated at multiple sites by various kinases, including glycogen synthase kinase-3β (GSK-3β), cyclin-dependent kinase 5 (CDK5), and protein kinase A (PKA) (Medina & Avila, 2014). Phosphorylation of Tau reduces its binding affinity for microtubules, leading to microtubule destabilization and impaired axonal transport, which is a hallmark of AD (Lee & Leugers, 2012).

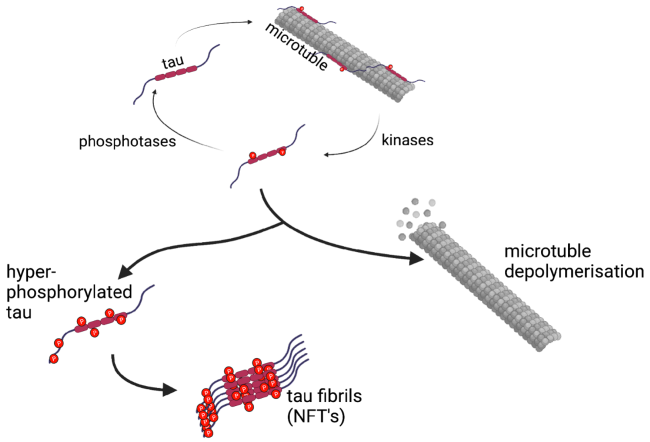

Figure 6. Microtubule dynamics under AD conditions. The creation of intracellular tau deposits and ultimately neurofibrillary tangles (NFTs) because of tau hyperphosphorylation and increased microtubule degradation. High phosphorylation of Tau sequesters it from its physiological cycle (thicker arrow). (Image adapted from Bodea, Eckert & Götz, 2016[163]).

Hyperphosphorylation of Tau is a key event in the pathogenesis of AD, as it leads to the formation of neurofibrillary tangles (NFTs), which are intracellular aggregates of hyperphosphorylated Tau protein (Goedert & Spillantini, 1999). NFTs are a pathological hallmark of AD and are associated with the loss of synapses and cognitive impairment (Figure 6) (Hardy & Selkoe, 2002).

In addition to its effects on microtubule stability, phosphorylation of Tau has been shown to regulate its nuclear localization and transcriptional activity (Maina et al., 2016).

To better understand the effect of hyperphosphorylation and how it affects the functions of Tau, two mutations, P301S and P301L, are widely used. Both these mutations are associated with frontotemporal dementia with Parkinsonism-17 (FTDP-17), a rare autosomal dominant neurodegenerative disorder characterized by progressive cognitive and motor dysfunction (Sakaue et al., 2005). The mutations are in the microtubule-binding region of Tau, creating a single amino acid substitution at position 301 of the protein, where proline is replaced with either serine or leucine, respectively and have been shown to increase Tau phosphorylation and impair its ability to bind to microtubules, leading to the formation of neurofibrillary tangles (Hutton et al., 1998).

Studies have shown that the P301S and P301L (Figure 6) mutations promote Tau aggregation and neurotoxicity, and that reducing Tau phosphorylation can attenuate these effects (Cho & Johnson, 2003; De Calignon et al., 2012). Additionally, these mutations have been shown to alter the subcellular localization of Tau and impair its normal physiological functions, including its role in nuclear transport and regulation of gene expression (Jesu´ et al., 2004).

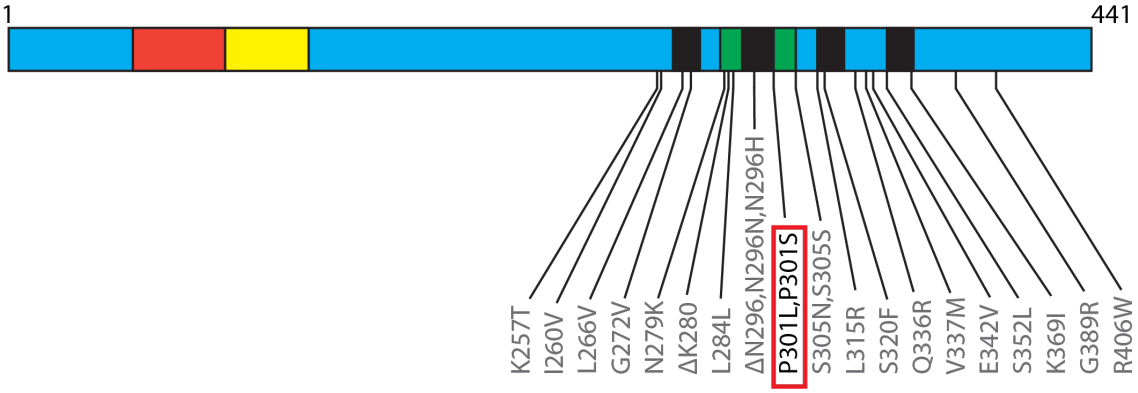

Figure 6 Mutations in Tau gene in FTDP-17.
Schematic Diagram of mutations causing FTDP-17 in full-length Tau (441 amino acids, 2N4R). Here highlighted are the two missense mutations P301L and P301S, where the Proline is swapped for a Leucine or Serine, respectively (Image adapted from Goedert & Jakes, 2004[164163]).

3.2.3.4 Tau aggregation and spreading

The accumulation of Tau pathology in the brain is a hallmark of several neurodegenerative disorders collectively known as tauopathies, including AD, FTD, and PSP (Spillantini & Goedert, 1998). While the exact mechanisms underlying the pathogenesis of tauopathies are not fully understood, evidence suggests that Tau aggregation and propagation are major contributors to the progressive cognitive and motor deficits observed in these disorders (Ballatore et al., 2007)

The process of Tau aggregation is believed to be initiated by the presence of pre-existing soluble and insoluble Tau oligomers and fibrils, which can accumulate within neurons and disrupt their normal function (Lasagna-Reeves et al., 2012). The kinetics of Tau protein aggregation involves a characteristic pattern of events (Figure 7). Upon initiation, Tau aggregation exhibits a lag phase (0-10h), during which there is a slow nucleation process as soluble Tau monomers undergo conformational changes and form initial aggregates.

Following a lag phase, the aggregation enters an exponential growth phase (10-18h), where the population of Tau aggregates rapidly increases through the recruitment of additional monomers. This phase is characterized by a positive feedback loop, where the growing aggregates facilitate the recruitment and incorporation of more Tau monomers.

Finally, the aggregation process reaches a plateau phase (> 18h), where a dynamic equilibrium is established between the formation and dissolution of Tau aggregates. This plateau represents a steady state where the overall Tau aggregation rate remains relatively constant (Polanco et al., 2022).

The presence of Tau seeds can promote the formation of new Tau aggregates through a process known as seeding, which involves the templated conversion of soluble Tau monomers into the insoluble, beta-sheet rich conformation of Tau found in NFTs (Clavaguera et al., 2009). Once initiated, the aggregation of Tau can spread from one neuron to another through a prion-like mechanism, leading to the propagation of Tau pathology throughout the brain (Holmes & Diamond, 2014; Takeda et al., 2015).

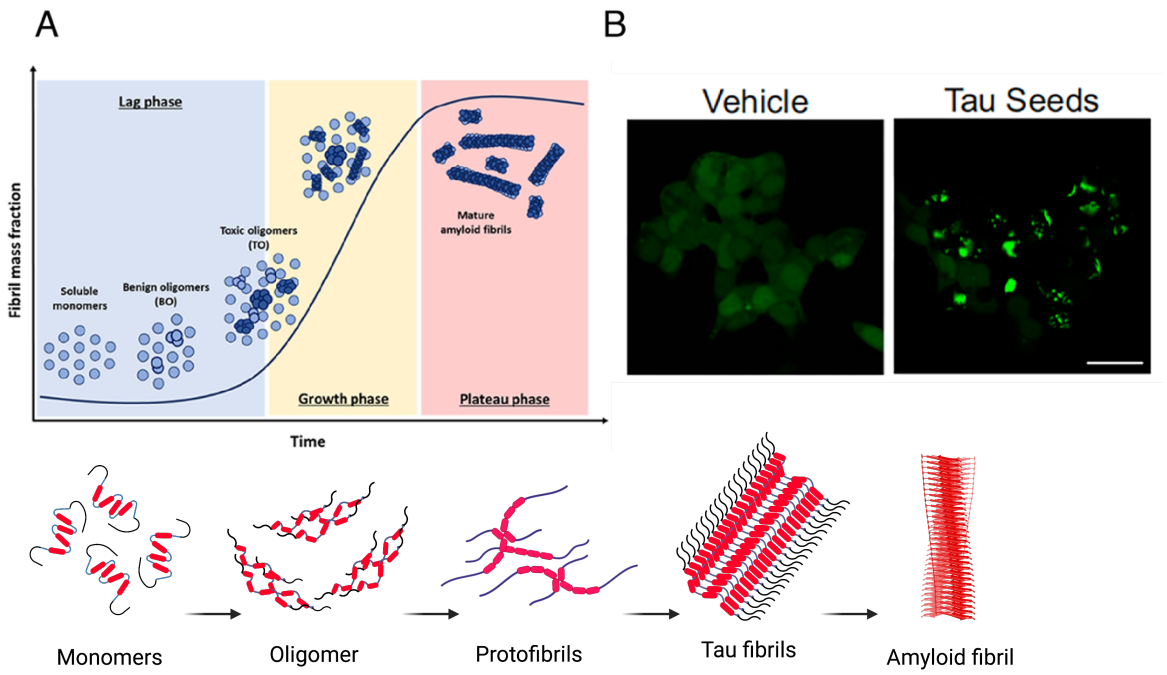

Figure 7. Protein aggregation kinetics *in vitro* and *in cellulo* (A) Diagram of typical tau protein aggregation kinetics. Protein aggregation starts with slow formation of oligomers in so called Lag phase (0-10h) for TauRD-P301L expressed in HEK239T. Lag Phase is then followed by a Growth phase (10-18h) were number of tau aggregates rapidly increases and first protofibrils start to form. Lastly aggregation reaches a Plateau phase (>-18h) where number of aggregates remains stable (Image adapted from Polanco et al.,2022[114]). (B) Confocal image of tau biosensor HEK293T cells expressing TauRD-P30iS-CFP/YFP FRET sensor. (left) Control cells transfected with liposome vehicle and (right) HEK cells transfected with 1 nM tau seeds. (Image adapted from Holmes et al., 2014[122])

In addition to seeding, the propagation of Tau pathology is thought to involve the intercellular transfer of Tau species, such as extracellular vesicles containing Tau or Tau protein released from dying neurons, between cells in a prion-like manner (Wu et al., 2016). This transfer can lead to the accumulation of Tau aggregates in neighboring neurons and the spread of Tau pathology throughout the brain (Brettschneider et al., 2014).

A highly effective approach to investigate protein aggregation, including the aggregation of Tau protein, involves the use of cell models that replicate disease-like conditions. One such model is the "HEK sensor" cell line (HEK293T) overexpressing the repeat domain of human N24R Tau with the FTD-associated P301S mutation (Sanders et al., 2014). This cell. line has been used extensively to study the aggregation of Tau and its modulation by various factors (Stopschinski et al., 2020).

The HEK cell model has been used to investigate the effects of small molecules on Tau aggregation and have identified several compounds that can inhibit Tau aggregation and promote its clearance (Holmes et al., 2014; Stopschinski et al., 2020)

The HEK cell model has also been used to study the effects of post-translational modifications on Tau aggregation, such as phosphorylation, acetylation, and ubiquitination (Ajit et al., 2019). These modifications can affect the aggregation propensity of Tau and may play a role in the pathogenesis of tauopathies.

Moreover, Diamond and colleagues have developed a novel HEK cell line that expresses a mutant form of Tau (P301L) that is associated with an increased risk of developing tauopathies (Sanders et al., 2014). This cell line has been used to study the effects of genetic and environmental factors on Tau aggregation and to screen for potential therapeutic compounds.

Overall, the HEK sensor cell model has been a valuable tool for studying the mechanisms underlying Tau aggregation and for developing potential therapies for tauopathies.

3.2.3.5 Tau aggregate structure

Tau fibrils, like other amyloid fibrils, are complex protein aggregates characterized by a highly ordered structure known as the amyloid fold. This distinctive fold is a hallmark of many neurodegenerative diseases, including Alzheimer's disease, Parkinson's disease, and various tauopathies (Chiti & Dobson, 2017).

The observed resemblance among diverse proteins lacking sequence or conformational homology implies that the conserved polypeptide chain backbone predominantly governs the key interactions within the amyloid fibril, which are largely distinct from the involvement of amino acid side chains. This underscores the potential significance of backbone-mediated interactions in determining the structural organization and stability of amyloid fibrils (Fändrich & Dobson, 2002).

Amyloid fibrils are protein aggregates characterized by a twisted, unbranched morphology that typically ranges from 7-13 nm in diameter but can reach micrometer-scale lengths. They are composed of smaller twisted assemblies known

as protofilaments, which contain parallel-arranged protein subunits along the fibril axis, usually with two to six subunits per protofilament (Figure 8). The molecular architecture of amyloid fibrils is characterized by a cross-β-sheet pattern, as revealed by X-ray diffraction studies (Sunde & Blake, 1997). In this structural arrangement, the protein subunits within the protofilaments are organized as β-strands oriented perpendicular to the fibril axis and are stabilized by a network of hydrogen bonds oriented parallel to the fibril axis (D. Eisenberg & Jucker, 2012; L. Q. Wang et al., 2020). The hydrogen bonding interactions between the β-strands enable the formation of a stable, elongated fiber through the stacking of the β-sheets in a head-to-tail fashion (D. S. Eisenberg & Sawaya, 2017). This structural motif is common to all amyloid fibrils, regardless of the identity of the protein subunits from which they are composed.

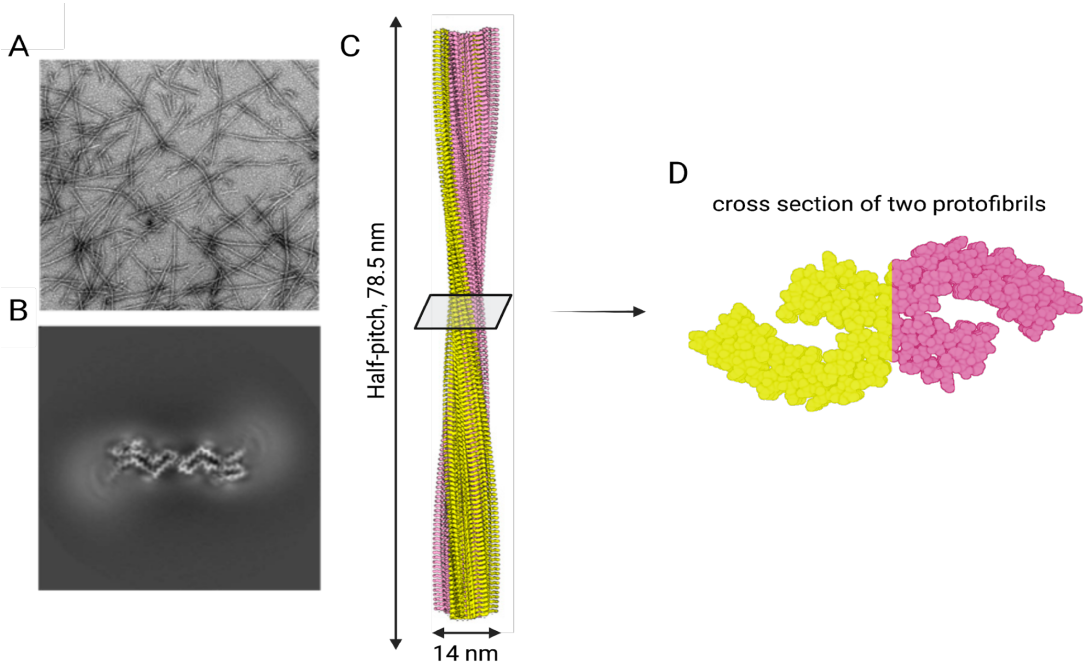

Figure 8. Cryo-Em structure of amyloid-like fibrils. (A)Negative staining TEM image of amyloid fibrils. (B) Cross-section view of two protofibrils forming a dimer. (C) 3D reconstruction of two protofibrils intertwined in a left-handed helix with a width of 14 nm and a half-helical pitch of 78.5 nm. (D) cross section of the two protofibrils forming dimer. (Images adapted from Wang et al.,2020[62]).

3.4.2.6 Tau liquid-like condensates

Liquid-liquid phase separation (LLPS) is a physical process by which a homogenous solution of molecules separates into two distinct phases, where one phase is condensed/enriched in these macromolecules and the other is depleted of those same macromolecules (Brangwynne et al., 2015). These phases are usually characterized by their rapid exchange of macromolecules and the formation of droplets. In cells, phase separation can drive the formation of non-membrane-bound organelles which are critical for a wide range of cellular processes, such as heterochromatin formation (Larson et al., 2017), nucleocytoplasmic transport (Schmidt & Görlich, 2016) and the formation of membrane less organelles such as the nucleoli (Feric et al., 2016).

One of the proteins implicated in phase separation is Tau. Studies have shown that Tau undergoes phase separation in vitro and in cells, leading to the formation of Tau droplets or liquid-like compartments (Wegmann et al., 2018). The ability of Tau to phase separate is dependent on its surrounding milieu (crowding and interaction partners) and its intrinsically disordered regions, which can undergo conformational changes upon mutations (e.g., P301L) or post-translational modifications.

PTMs of Tau, including as phosphorylation, acetylation, and methylation, have been found in recent research to modify its phase behavior and proclivity to form aggregates. Phosphorylation of Tau at certain locations, for example, has been found to increase the likelihood of LLPS and aggregation (Figure 9) (Wegmann et al., 2018). Furthermore, recent studies have also highlighted the importance of RNA in the phase separation of tau. RNA-binding proteins (RBPs) and RNA molecules have been shown to co-localize with Tau in liquid-like droplets facilitating tau condensate formation or affecting protein-protein interactions, suggesting a potential role for RNA in Tau phase separation and aggregation (Hochmair et al., 2022). The interaction between Tau and RNA appears to be mediated by the intrinsically disordered regions (IDRs) of both proteins, due to their ability to form weak, transient, multivalent interactions, which are known to be critical for phase separation and aggregation (Hochmair et al., 2022; Lin et al., 2019, 2021).

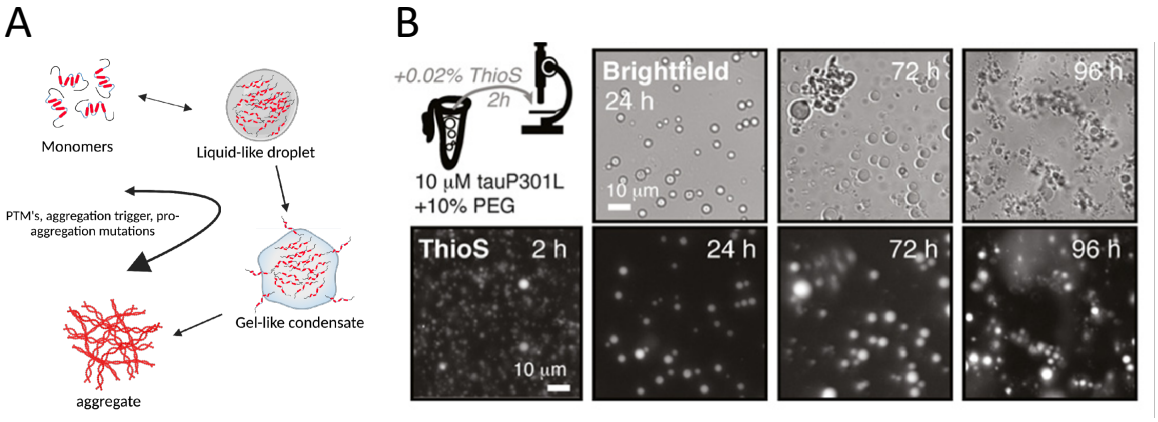

Figure 9. Induction of Tau LLPS upon mutation causing aggregation.
(A) Schematic of the principle of LLPS and the transition into aggregation through gelation of liquid-like droplet. (B) Progressive aggregate formation of tau condensates, after incubating tau-P301L with 10% PEG, a crowding agent, at room temperature (25°C). Tau clusters appear to connect individual droplets after 72h with an even higher increase after 96 h. ThioS fluorescence reveals increasing amount of tau aggregates, due to its high binding affinity for β-pleated sheet confirmations, indicating a shift from tau condensates to tau aggregates with increasing ThioS fluorescence. (Image adapted from Wegmann et al., 2018[129]).

Dysregulation of Tau phase separation has been implicated in several neurodegenerative disorders, including AD and FTD. Studies have shown that mutations or PTMs of Tau can alter its ability to phase separate, leading to the formation of insoluble aggregates or inclusion bodies (Wegmann et al., 2018).
The emerging role of LLPS in Tau aggregation and tauopathies provides a potential bridge between the biophysical properties of Tau protein and the pathological changes observed in neurodegenerative diseases such as AD.

3.5 Microscopic methods to investigate Tau protein aggregation.

The characterization of protein aggregates entails the utilization of numerous techniques and methods. Among these, imaging plays a crucial role. Microscopy has been an integral part of research for an extensive period and continues to evolve, enabling the capture of biological processes at higher resolutions and the study of these processes under novel conditions. Various microscopy techniques are available for investigating protein aggregation phenomena.

3.5.1 Confocal microscopy and immunohistochemistry

Immunohistochemistry (IHC) is a pivotal technique in the investigation of protein aggregation, as it facilitates the specific detection and localization of target proteins within tissue sections via antibody-antigen interaction. Integration of IHC with confocal microscopy augments the visualization and quantification of protein aggregates within cells (Figure 10) (Pawley, 2006).

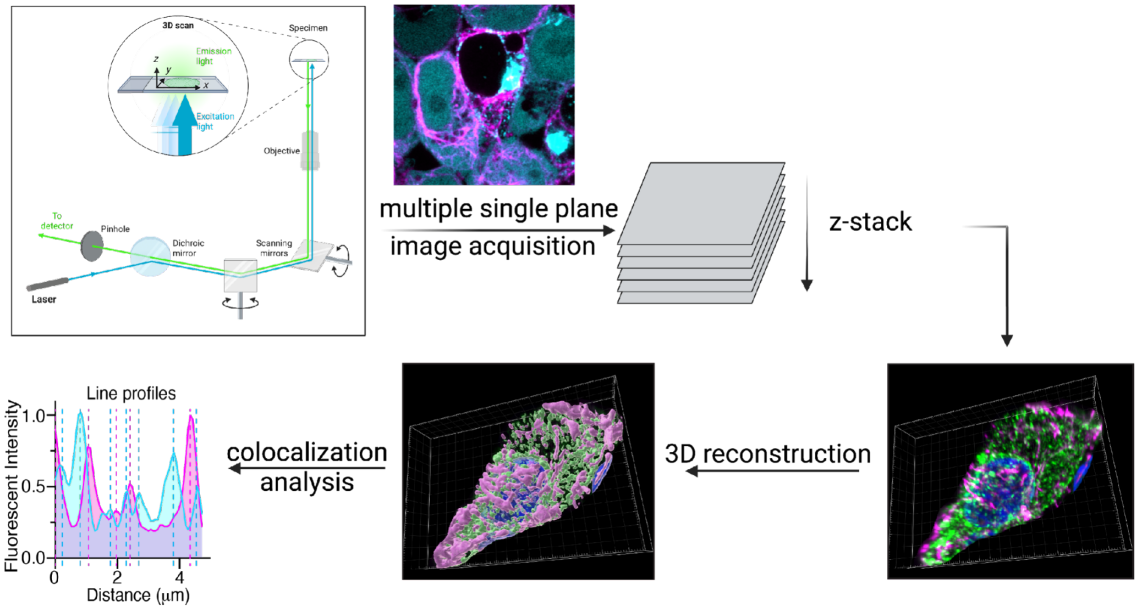

Figure 10. Principle of confocal microscopy and immunohistochemistry. Cells are initially subjected to staining and imaging procedures using a laser scanning confocal microscope, capturing multiple single-plane images at different focal planes. Subsequently, the acquired confocal images are subjected to deconvolution to improve image resolution and clarity. Utilizing IMARIS software, three-dimensional visualization of the confocal images is performed, enabling the reconstruction and exploration of the spatial organization of the cellular staining's. To assess colocalization between different fluorescent signals, colocalization analysis is carried out using line plots of fluorescent intensities obtained from the respective staining's. Colocalization is considered to occur when the line profiles of two signals overlap or come into close proximity with each other.

Confocal microscopy, as an advanced imaging modality, offers high-resolution visualization capabilities, thereby enabling researchers to discern protein aggregates with increased precision (Pawley, 2006). Z-projections, generated by assembling optical sections acquired at distinct focal planes, allow for three-dimensional reconstruction of cellular structures, thus providing insights into the

spatial organization and distribution of protein aggregates (Frost et al., 2009). The combination of confocal microscopy with IHC permits the specific identification of aggregating proteins, such as Tau, in relation to other cellular components, thereby facilitating a comprehensive understanding of the aggregation process within the cellular milieu (Ballatore et al., 2007). Colocalization analysis further refines the study of protein aggregation by elucidating the spatial relationships between aggregating proteins and other cellular constituents or proteins (Kadavath et al., 2015). When utilized in conjunction with IHC and confocal microscopy, this approach allows for the simultaneous visualization of multiple proteins and the identification of their subcellular interactions (J. L. Guo et al., 2013).

I employed confocal microscopy, z-projections, colocalization analysis, and IHC to characterize the intracellular localization of Tau aggregates in AD. Their findings demonstrated that Tau aggregates were predominantly localized within the endoplasmic reticulum, offering insights into the molecular mechanisms underlying Tau-induced neurodegeneration.

3.5.2 Fluorescence lifetime imaging microscopy (FLIM)

FLIM-FRET (Fluorescence Lifetime Imaging Microscopy with Förster Resonance Energy Transfer) is a powerful technique employed to investigate protein-protein interactions and conformational changes within live cells. It leverages the principles of Förster Resonance Energy Transfer (FRET) to provide valuable insights into molecular interactions (Becker, 2012).

FLIM-FRET involves the use of fluorescent protein tags, such as CFP and YFP, where one fluorophore serves as the donor (CFP) and another as the acceptor (YFP). The excited donor fluorophore can transfer its energy to an adjacent acceptor fluorophore through non-radiative resonance energy transfer. This transfer occurs when the distance between the donor and acceptor fluorophores is within a critical range (~10nm) reflecting their spatial proximity (Figure 11).

By measuring the fluorescence decay rate, or fluorescence lifetime, of the donor fluorophore, FLIM-FRET provides information about the molecular interactions and

structural changes within protein complexes. A shorter fluorescence lifetime indicates efficient FRET and suggests proximity between the donor and acceptor fluorophores, signifying protein-protein interactions. Conversely, a longer fluorescence lifetime suggests a lack of FRET and a greater distance between the fluorophores.

FLIM-FRET has demonstrated its utility in investigating protein aggregation, particularly in the context of Tau, as demonstrated in the study conducted by (Hochmair et al., 2022) In their research, FLIM-FRET was employed to quantify conformational changes within Tau protein by measuring fluorescence lifetimes of in vitro Tau condensates. The study highlighted FLIM-FRET as an effective approach to probe the dynamic structural transitions of Tau and provided valuable insights into the behavior of Tau aggregates (Hochmair et al., 2022).

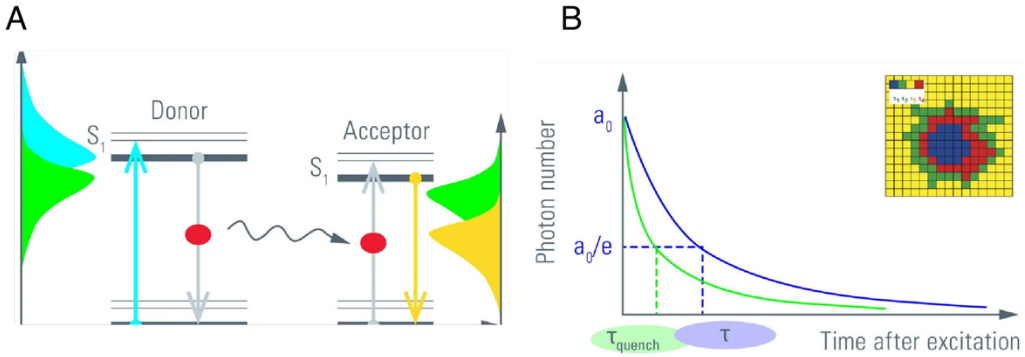

Figure 11. Principal of FRET and FLIM. (A) Schematic showing the principal of FRET (Förster Resonance Energy Transfer). If in proximity (10 nm) the donor (left) will transfer energy from its excited fluorophore to the acceptor (right) which is in the ground state. Through the transferred energy the acceptor fluorophore becomes excited and emits light. It is important to note that the Excitation wavelength of the acceptor and Emission wavelength of the donor have to overlap. (B) Fluorescence photon count is plotted against time after excitation, where the initial photon count, a_0, decays exponentially. Fluorescence lifetime can be determined by looking at the decay rate of a_0/e, which is ~37%. FRET can cause quenching which will lead to a shift of fluorescent lifetime to the left, shortening it. By measuring the lifetime at each position in an image it produces a spatial lifetime map (see insert on the right) (Image taken from Leica website https://www.leica-microsystems.com/science-lab/life-science/what-is-fret-with-flim-flim-fret/).

3.5.3 Optical diffraction tomography (ODT)

Optical diffraction tomography (ODT) is a non-invasive, label-free imaging technique that leverages the principles of interferometry and tomography to generate three-

dimensional refractive index (RI) distributions of biological specimen (Müller et al., 2015). ODT reconstructs the specimen's RI distribution by measuring the scattered light intensity and phase shift as light propagates through the sample, providing quantitative information on the specimen's morphology and composition (Biswas et al., 2021).

The methodology of ODT involves illuminating the sample with a coherent light source and detecting the interference pattern between the scattered light and a reference beam. By acquiring multiple two-dimensional diffraction patterns at different illumination angles, a three-dimensional RI distribution can be reconstructed using computational algorithms such as MATLAB R 2019b (Figure 12) (Biswas et al., 2021).

The relationship between RI and mass density of a sample, which is described by the Lorentz-Lorenz equation or the Gladstone-Dale relation: $RI = K * \rho + \alpha C$.

Here, RI is the refractive index of the sample, K is the specific refractive index increment (a constant that depends on the material and wavelength of the incident light), and ρ is the mass density of the sample.

ODT has been applied to study protein aggregation by enabling the observation of cellular alterations, including changes in cytoplasmic density and organelle morphology, which are induced by protein aggregation (Kemper et al., 2006). The technique's ability to provide quantitative, label-free, and non-invasive imaging makes it well-suited for the investigation of protein aggregation dynamics in live cells, offering the potential to elucidate the complex processes underlying aggregate formation, intracellular trafficking, and clearance (Kim et al., 2016).

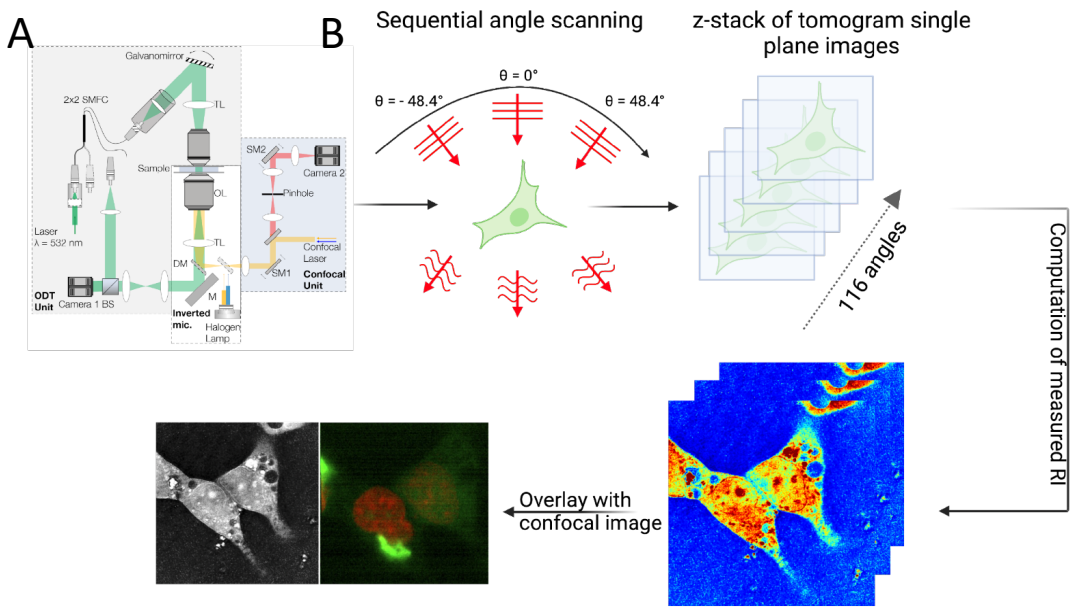

Figure 12. Principle of optical diffraction tomography. (A) Optical setup used to obtain fluorescence and refractive index images of HEK cells (SMFC, single mode fiber coupler; TL, tube lens; CL, condenser lens; OL, objective lens; M, mirror; DM, dichroic mirror. (B) First, phase maps are generated by imaging the HEK cells from different angles, capturing the changes in the phase of the transmitted light caused by the cells' refractive properties. Next, the recorded refractive index data is computationally reconstructed, yielding ODT images that provide information about the refractive index distribution within the cells. These ODT images are then overlapped with co-imaged fluorescent images, allowing for precise colocalization of the refractive index measurements with the fluorescence signals emitted by the Tau-labeled structures. By combining the ODT data with the fluorescence data, the mass densities of Tau within the cells can be confidently calculated, enabling a comprehensive understanding of Tau distribution and accumulation patterns in the cellular context. (Schematic for microscope setup adapted from Biswas et al.)

4 Aim of the studies

A comprehensive understanding of Tau aggregation necessitates an examination of the molecular assembly state and the dynamic interactions of various Tau accumulation forms. Hence, this study aimed to characterize Tau aggregation propagation in depth using live-cell imaging and in vitro studies to investigate the different forms of Tau accumulations. The physical and chemical properties of these accumulations were explored using a cellular model and compared to those of in vitro-generated Tau accumulations.

A multimodal microscopy approach was employed, encompassing laser scanning confocal colocalization microscopy and 3D reconstructions in conjunction with stimulated emission depletion (StED) microscopy to explore the intracellular localization and potential interacting partners of Tau aggregates, FLIM and FLIM-FRET to examine the biochemical properties of Tau within its local environment, and ODT to assess physical properties such as density, mass, and volume of Tau condensates. By employing these techniques, this study aims to provide insights into the early stages of cellular Tau aggregation and possible organelle interaction partners, paving the way for the creation of novel therapeutic strategies to treat AD and tauopathies.

5 Results

5.1 Accumulations of Tau in cell models of tauopathy

5.1.1 Hierarchy of Tau accumulation appearance in HEK sensor cells

The study of Tau aggregation has been a focal point in understanding the pathogenesis of neurodegenerative diseases, such as AD. One widely employed approach to study Tau aggregation involves seeding experiments, which have significantly contributed to the current understanding of the mechanisms underlying Tau aggregation, propagation, and spreading (Clavaguera et al., 2009).

Seeding experiments are typically performed by introducing preformed Tau aggregates (seeds) into cellular or animal models, which then induce the aggregation of endogenous Tau (Frost et al., 2009). These experiments have been pivotal in demonstrating the prion-like behavior of Tau, wherein the protein exhibits the ability to self-propagate and spread both between cells and across different brain regions (Takeda et al., 2015).

A prevalent challenge in investigating protein aggregation, particularly Tau, using cellular models lies in the precise and quantitative assessment of Tau aggregation dynamics in live cells. Conventional methodologies often entail endpoint assays or post-fixation imaging, which preclude real-time, quantitative insights into the aggregation process or the intracellular factors modulating it. Furthermore, these techniques may necessitate the application of potentially perturbing labels or tags, which can influence the native behavior of Tau in cells (Holmes & Diamond, 2014).

Thus, it was a significant breakthrough when Mark Diamond's group introduced their novel HEK293T cell line expressing the Tau repeat domain (TauRD) with the FTD-17-linked mutation P301S, fused to either cyan fluorescent protein (CFP) or yellow fluorescent protein (YFP) (Holmes & Diamond, 2014). The fusion of TauRD to CFP/YFP not only facilitates the measurement of fluorescence resonance energy transfer (FRET), yielding a more precise kinetic readout, but also enables real-time visualization of Tau aggregation (Holmes & Diamond, 2014).

Utilizing the HEK cell model, the initial goal was to delineate the intracellular propagation mechanism of Tau aggregation. To accomplish this, live-cell imaging experiments were conducted, longitudinally monitoring Tau aggregation by seeding TauRD-expressing CFP/YFP-HEK cells with Tau condensates, formed by LLPS. These condensates are a common widely spread mechanism to induce aggregation in cells. Seed materials can be acquired through various approaches, such as isolating pathological Tau aggregates from patient or transgenic animal model brains or employing in vitro fibrillization using recombinant Tau protein preparations (Clavaguera et al., 2009; Hochmair et al., 2022; Holmes & Diamond, 2014; Wegmann et al., 2018) the latter method was employed by incubating recombinant full-length (2N4R) Tau with heparin, a highly sulfated glycosaminoglycan that acts as a polyanionic cofactor. This accelerates the in vitro assembly of Tau monomers into fibrillar structures, effectively recapitulating pathological Tau aggregates observed in AD. The reaction mixture was then incubated for 24 hours at 37°C to facilitate appropriate oligomerization of Tau. Subsequently, the mixture was introduced to the cells and imaged for a period of 24h (Figure 13).

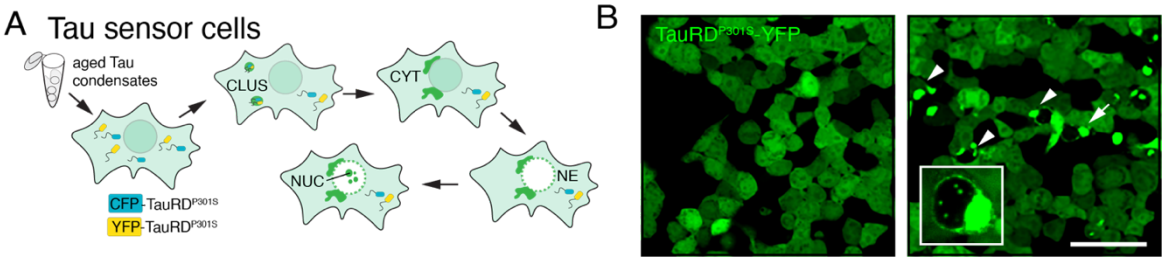

Figure 13. Principal of Tau aggregation and seeding assay in HEK293T-TauRD^{P301S}-CFP/YFP cells. (A) Schematic of experimental procedure of Tau seeding in HEK cells expressing TauRD^{P301S}-CFP/YFP to study aggregation over time. (B) Representative laser scanning confocal image of seeded HEK cells right after seeding (left) and after 24h (right) (Scale bar = 10 µm).

As previously mentioned, seeding HEK cells expressing the aggregation-prone 4R Tau repeat domain with the P301S mutation stimulated the formation of intracellular Tau accumulations. Notably, these accumulations exhibited unique cellular localizations, morphologies, and fluorescence intensities. Furthermore, multiple accumulations, either of the same or different types, could coexist within a single cell (Figure 14B) (Hochmair et al., 2022).

Based on subcellular localization, cytosolic and nuclear Tau inclusions could be distinguished. Cytosolic inclusions were further classified into small Tau clusters (size ~1.3µm) dispersed within the cell body (CLUS) or at the nuclear envelope (NE), and large Tau accumulations (CYT; size ~3-6µm) in proximity to the nucleus. Nuclear accumulations (NUC) were situated within the nucleus, specifically in regions devoid of DAPI-labeled DNA. The different types of accumulations were clearly distinguishable by size, intensity, and localization (Figure 14 D).

Intriguingly, when observed at higher resolution using StED microscopy, CLUS and NE accumulations appeared as short, elongated, branched Tau assemblies, resembling short, branched fibrils, while CYT and NUC Tau displayed larger amorphous clusters of these structures, resembling more the amyloid like aggregates observed in AD brains (Figure 14A) (Barghorn et al., 2004).

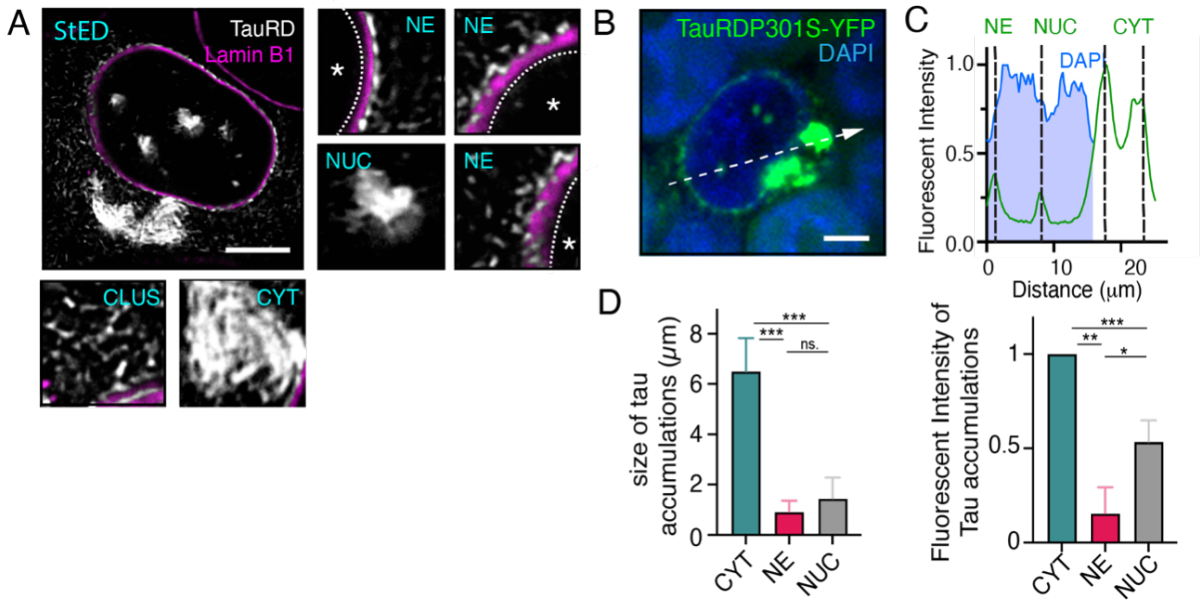

Figure 14. Definition and characterization of Tau accumulations. (A) Representative high-resolution StED micrograph displaying diverse Tau accumulations co-stained with Lamin B1 (pink). Distinct morphological forms of Tau aggregates, including CLUS, CYT, NE, and NUC, are evident. (B) Representative laser scanning confocal image of a TauRD^{P301S}-CFP/YFP-expressing HEK cell co-stained with DAPI, emphasizing the distinct localization of Tau aggregates through Plot Profile analysis using ImageJ (white arrow). (C) Representative graph displaying line plots of Tau and DAPI, highlighting the unique location of each aggregate type. (D) Graphs illustrating the classification of Tau accumulations based on size and intensity. Size was determined using the half-width for each peak displayed in the line plot graph. Intensities were normalized to the highest measured intensity peak and subsequently compared between accumulation types (N=5). (Scale bar for StED image = 10 µm; Scale bar for confocal image = 5µm) (Statistical significance was assessed by ordinary one-way ANOVA ***, p≤ 0.002)

Furthermore, another noteworthy observation emerged from time-lapse live-cell confocal z-stack imaging at 60-minute intervals of sensor cells treated with Tau condensates (Figure 15), which highlighted a stepwise appearance of Tau accumulation subtypes. At first, small, bright CLUS Tau puncta formed in the cell cytoplasm, eventually transforming into larger CYT Tau aggregates. CLUS and CYT Tau accumulations were detected in all cells displaying any type of Tau aggregation during the experiment. NE Tau accumulations materialized approximately 12-15 hours post-seeding in 28% of cells with accumulations. NUC Tau accumulations were initially observed at >20 hours after seeding, arising in 6% of all cells with accumulations (Figure 15 B, C).

The findings imply a sequential emergence of Tau accumulation subtypes, wherein small cytosolic clusters develop into larger aggresomal-like cytosolic aggregates near the nucleus. At this point, they begin forming small puncta-like structures, which may obstruct nuclear transport and subsequently lead to leakage into the nucleus, where they ultimately form nuclear accumulations at DNA low sites.

5.1.2 Tau accumulations cause impairment of nuclear transport

In Tau sensor cells without Tau accumulations, TauRD-CFP/YFP is found in both the cytoplasm and the nucleoplasm at similar concentrations (Figure 15 A) because TauRD-CFP/YFP (~42 kDa) is small enough to pass nuclear pores via passive diffusion. Intriguingly, when comparing cells exhibiting any form of tau accumulations to those without aggregation, a discernable difference in soluble tau fluorescent intensity was observed. To explore this phenomenon, fluorescent intensities of soluble tau within the nucleus and cytoplasm were measured and compared between cells with and without tau accumulations (Figure 15 D). Upon the emergence of initial CLUS and CYT accumulations, fluorescent intensities of both cytoplasmic and nuclear soluble Tau decreased, suggesting that Tau is likely being recruited to the accumulations. Notably, it seems that a greater proportion of Tau is being recruited from the nucleus (a loss exceeding 60% of fluorescent intensity

measured within the first 10 hours) as opposed to cytoplasmic Tau (a loss of approximately 50% of fluorescent intensity measured within the first 10 hours). This discrepancy might be due to the higher availability of soluble Tau in the cytoplasm, rendering the recruitment effect less conspicuous.

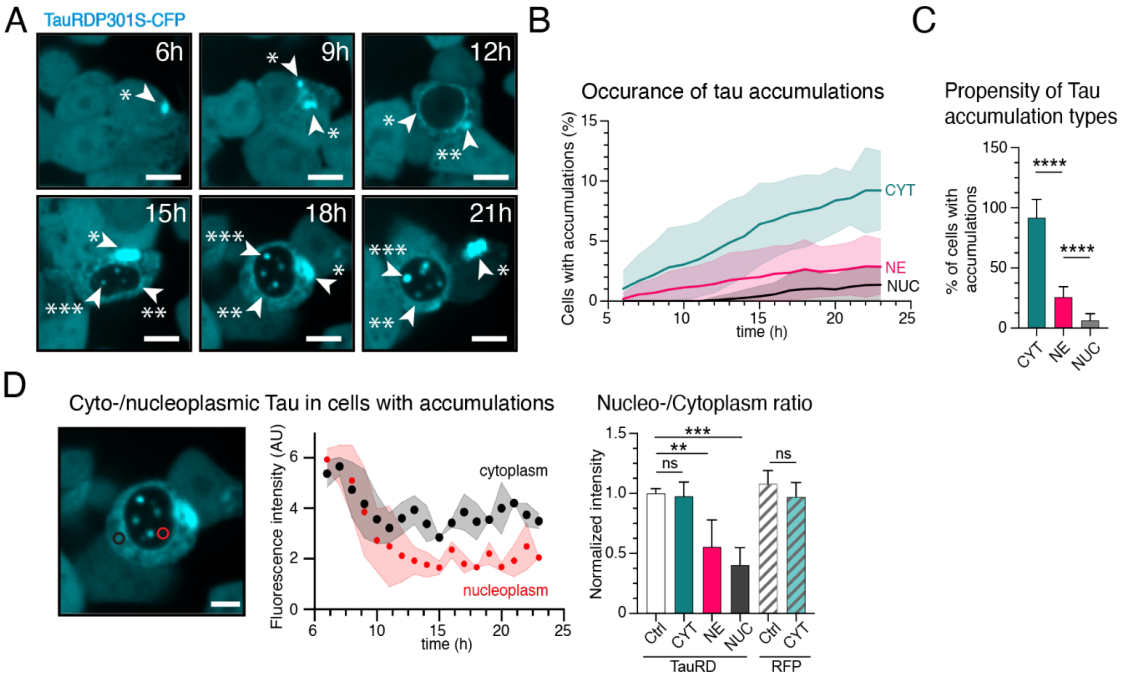

Figure 15. Condensate-induced Tau accumulations in HEK TauRD-^{P301S}-CFP/YFP.
(A) Representative image sequence of HEK sensor cells treated with 24h old Tau condensates and subsequently imaged for 24h. Tau accumulations start appearing after ~6h post transfection. Distinct Tau accumulation types are indicated by (*) and white arrow ((*) CYT, (**) NE, (***) NUC. Scale bars = 10 µm)). (B) Time-dependent occurrence of Tau accumulations in all imaged cells. After 24h around 10% of all cells showed CYT, 3% NE and 1% NUC accumulations. CYT and NE appear coincidentally after 6h with cells showing CYT accumulations more frequently. NUC accumulations appear after 13h earliest. (C) Propensity of Tau accumulation types within all measured aggregated cells. All measured and imaged aggregated cells showed CYT accumulations, 26% showed NE accumulations and 6 % showed NUC accumulations (N= 21). (D) Fluorescent Intensity measurements of soluble Tau in HEK sensor cells with and without Tau accumulations. Graph (left) shows the fluorescent signal of CFP-TauRD^{p301S} over time for cytoplasm and nucleus. Graph (right) shows the Ratio between fluorescent signal of Tau in the Nuclear and cytoplasmic space for cells showing either CYT, CYT +NE or all three types, as well as the control for cells expressing RFP (N=10). (Scale bar = 10µm, N =21, 7 positions in 3 independent experiments, stastical significance was assessed by ordinary one-way ANOVA with, ** p≤ 0.02 and **** p≤0.0001 for (C))

As a result, the ratio between nuclear and cytoplasmic fluorescent signals for each emerging tau accumulation subtype was assessed, displaying a correlated decrease in fluorescent signal coinciding with the emergence of NE and NUC tau

accumulations. Notably, the appearance of CLUS/CYT Tau accumulations in cells (early stage) does not affect Tau levels in the cytoplasm and nucleus. However, with the emergence of NE accumulations (intermediate stage), a 50% drop in fluorescent intensity is observed, suggesting that nuclear Tau is recruited first. Yet, when compared to the ratio of cells exhibiting NUC accumulations, an additional 10% decrease is seen, indicating further recruitment of nuclear Tau. Importantly, when compared to HEK cells expressing RFP, no significant loss in fluorescent signal between cytoplasm and nucleus can be observed between cells with and without Tau accumulations, suggesting that this a tau specific process.

In summary, these findings imply that when Tau accumulations reach the nuclear envelope, they can hinder the nuclear passive transport of $TauRD^{P301S}$. However, this is followed by increased nuclear leakage later, as evidenced by the presence of NUC accumulations (Eftekharzadeh et al., 2018; Hochmair et al., 2022).

5.2 Characterizing cellular Tau accumulations using advanced imaging. techniques

5.2.1 FRAP analysis of Tau accumulations.

Upon observing three distinct types of Tau accumulations that appeared to emerge in a time-dependent manner, it was hypothesized that these accumulation subtypes might exhibit differences in their physical and chemical properties, as well as their conformational states that transition over time from a more soluble state to a more solid state.

To investigate the disparities among these accumulations, fluorescence recovery after photobleaching (FRAP) experiments were first employed. FRAP is a robust technique utilized to study protein aggregation dynamics (Kanaan et al., 2020; Wegmann et al., 2018). The method entails selectively photobleaching a fluorophore-labeled protein (CFP/YFP) within a defined region of interest (ROI) and subsequently monitoring the recovery of fluorescence intensity over time as

unbleached proteins diffuse into the bleached area (Sprague & McNally, 2005). This facilitates the tracking of the passive diffusion rate of the fluorophore, and consequently, the viscosity of the labeled protein. For example, a low recovery rate suggests that the fluorophore cannot readily diffuse into the bleached ROI, indicating a more tightly packed protein assembly (Boyko et al., 2020). Therefore, I expected a clear difference between CLUS, CYT, NE and NUC.

FRAP experiments were conducted on the same HEK sensor cells expressing TauRD^{P301S}-CFP/YFP and seeded with 24-hour aged full-length Tau (htau40) condensates. The bleached ROIs were chosen based on the accumulation type, as depicted in Figure 16 A. Images were captured in rapid succession, at a rate of one image per second, to detect potential fast recovery rates. Each ROI was subjected to three consecutive laser pulses to ensure complete bleaching of the region. As anticipated, each accumulation type displayed a distinct recovery rate due to their conformational state (Figure 16 B).

The fluorescence recovery rates of seeded and non-seeded HEK sensor cells were compared. As anticipated, the control HEK cells expressing only TauRD^{P301S} displayed nearly instantaneous full recovery (100% mobile fraction) and a half-life recovery ($t_{1/2}$) of 5s. Small CLUS accumulations exhibited an almost complete recovery (88%), albeit at a slower pace, with a $t_{1/2}$ of 18s. Interestingly, NE and CYT accumulations displayed nearly identical recovery rates, with mobile fractions of 38% and 34%, respectively. However, NE accumulations demonstrated a faster recovery, with a $t_{1/2}$ of 6s compared to 9s for CYT accumulations. NUC accumulations exhibited minimal recovery, with a 91% immobile fraction and a recovery rate of 9s, comparable to CYT accumulations.

These findings suggest that each accumulation type possesses distinct diffusion rates and packing densities. For instance, CLUS Tau displays almost complete recovery but at a slower pace compared to non-seeded cells, indicating that Tau diffuses more slowly in seeded cells, possibly due to reduced passive diffusion mobility. CYT and NUC accumulations exhibit similar recovery speeds, yet they differ in their mobile/immobile fractions, which could be attributed to differences in packing

density. This implies a higher-order structure in NUC accumulations compared to CYT, allowing for less total recovery.

It is essential to note that the ROIs used differ for each accumulation type, which influences the $t_{1/2}$, as larger ROIs require more time to reach $t_{1/2}$. Consequently, comparing the recovery rates of NE and CYT, for example, is challenging. However, since NE accumulations appear as small puncta surrounding the nucleus, ROI sizes had to be adjusted to ensure that only NE accumulations were bleached, avoiding potential measurement artifacts.

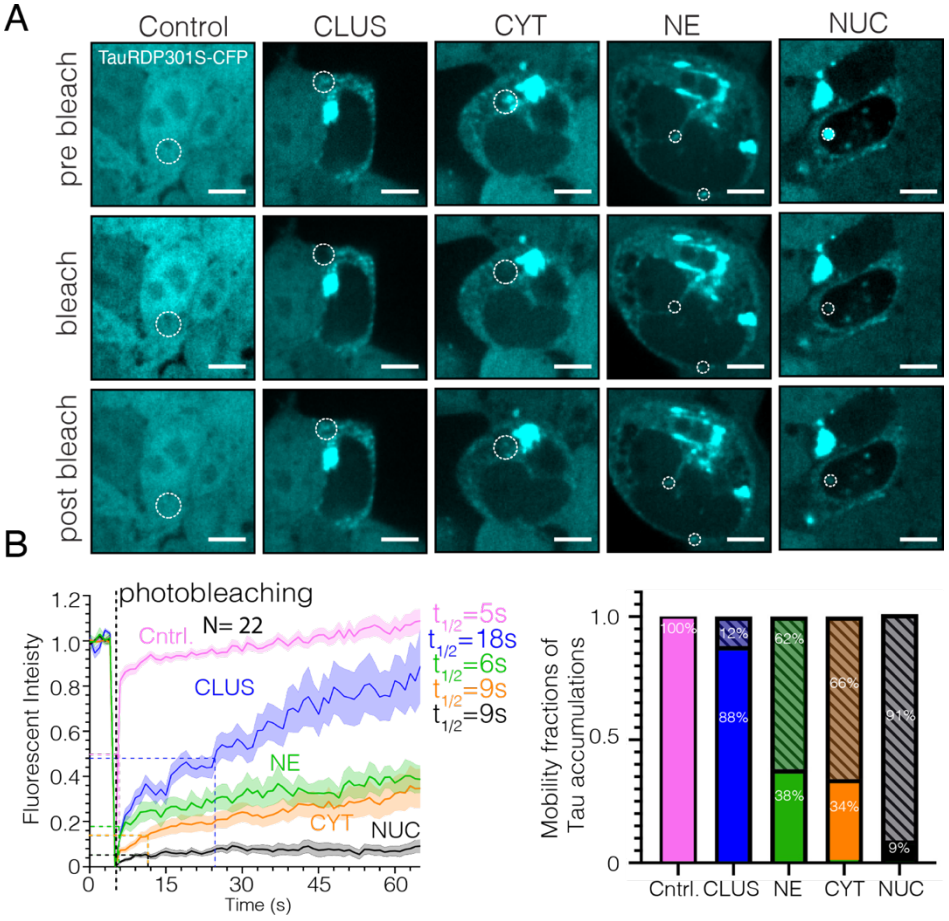

Figure 16. FRAP analysis of Tau accumulation types in HEK TauRD-^{P301S}-CFP/YFP.
(A) Spinning disc confocal images of Tau accumulation FRAP measurements pre-bleach, immediately post-bleach, and 60 seconds after recording. The bleached ROI is indicated by the white circle (Scale bar = 5µm, N= 22 Tau accumulations per type). (B) Fluorescence recovery measurements of Tau accumulations over 60 seconds (left) and the corresponding mobile and immobile fractions (right). The graph displays the normalized fluorescence intensity before and after bleach (indicated by the dashed black line). The average fluorescence intensity was measured every second for 60 seconds and subsequently normalized. Half-life recovery rates indicate the time required to achieve half the maximum recovery. The bar graph illustrates the ratio of mobile to immobile fractions for each Tau accumulation type.

5.2.2 FLIM measurements of Tau accumulations in HEK cell model to determine protein-protein interaction and packing.

FRAP analysis revealed significant differences in diffusion rates and protein mobility of Tau. However, FRAP is limited in the information it can provide. Therefore, FLIM combined with FRET, a powerful and sensitive method to further study protein aggregation at a molecular level was deployed. FLIM-FRET enables the measurement of protein-protein interactions, determination of intermolecular distances, and the assessment of conformational changes. Compared to FRAP, which primarily measures protein mobility and diffusion rates, FLIM-FRET offers additional insights into the spatial and temporal dynamics of protein aggregation. It enables the detection of transient and weak interactions among proteins, as well as the identification of specific protein conformations within aggregates. Furthermore, FLIM-FRET can be used to study the heterogeneity of protein aggregates and the distribution of distinct protein conformations.

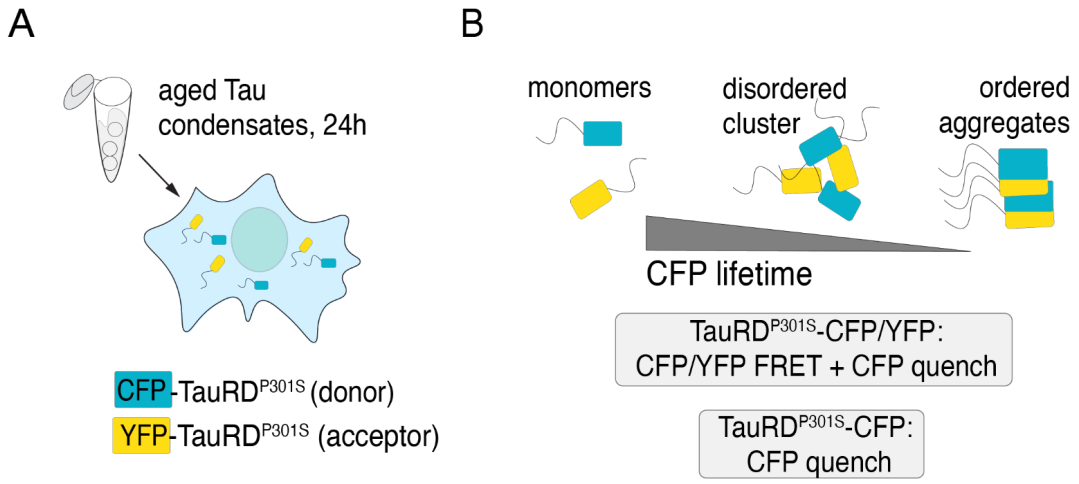

Figure 17. Principle and experimental setup of FLIM in HEK sensor cells. (A) Diagram depicting the experimental setup for FLIM measurement in HEK-TauRD-P301S-CFP and TauRD^{P301S}-CFP/YFP cells. CFP fluorescence was assessed and analyzed to determine FRET signal and fluorescence lifetimes of the donor. (B) Graphic representation of the underlying concept of FLIM-FRET readout. As the distance between the donor (CFP) and acceptor (YFP) molecules decreases, energy can be transferred from the donor to the acceptor, leading to a reduction in the donor's fluorescence lifetime. A similar effect can occur when donor fluorophores are near each other, resulting in self-quenching.

As for the previous experiments HEK sensor cells expressing TauRD^{P301S}-CFP/YFP were employed with and without seeding. Additionally, HEK sensor cells expressing TauRD^{P301S}-CFP were utilized to distinguish between FRET signal and CFP Donor self-quenching. In self-quenching (Figure 17), an energized fluorophore imparts its energy to another fluorophore in its ground state or encounters another fluorophore, leading to non-radiative energy transfer and diminished fluorescence. Contrasting with FRET signal, which is highly specific between a donor and an acceptor fluorophore necessitating a FRET pair to be within 1-10 nm proximity for energy transfer to occur, self-quenching is a concentration-dependent event that decreases fluorescence intensity due to inter-actions among fluorophores. On the other hand, FRET is a distance-dependent and highly selective process.

Fluorescent lifetimes (LT) of HEK sensor cells expressing TauRD variants were assessed using a laser scanning confocal microscope. The obtained LTs were subsequently fit-free assigned to Tau accumulations based on their phenotype on a phasor plot, which depicts each individual pixel with its corresponding measured fluorescent lifetime in the entire field of view.

FLIM-FRET measurements disclosed accumulation-specific fluorescence lifetimes for CFP in cells expressing either CFP solely or in conjunction with YFP. In instances where HEK sensor cells co-expressed CFP and YFP, LTs were further diminished due to the combined influence of FRET and CFP self-quenching (Figure 18A).

For soluble Tau in the cytoplasm of HEK sensor cells expressing TauRD-^{P301S}-CFP/YFP in the absence of accumulations, the fluorescence LT was the most extended, with LT_{SOL} = 1.77±0.02 ns. Owing to the capacity of Tau to freely diffuse within the cytoplasmic compartment, minimal FRET transpires between the donor and acceptor.

The LTs for CLUS and NE were quite comparable, albeit reduced, with $LT_{CLUS/NE}$ = 1.45±0.05 ns, suggesting a higher-order packing density relative to soluble Tau in the cytoplasm. A more pronounced decrease in CFP LT was observed for CYT and NUC, with both exhibiting similar LTs of $LT_{CYT/NUC}$ = 1.34±0.04 ns. Notably, a small subgroup of CYT accumulations (AMY) with a fibrillar appearance demonstrated a further reduced LT of LT_{AMY} = 1.18±0.02 ns. This implies that these cytosolic

aggregates possess a higher packing density, potentially akin to amyloid-like aggregates. Ultimately, these findings indicate a progressive density of TauRD^{P301S} molecules in the order of CLUS/NE < CYT/NUC < AGG < AMY accumulations (Figure 18 D).

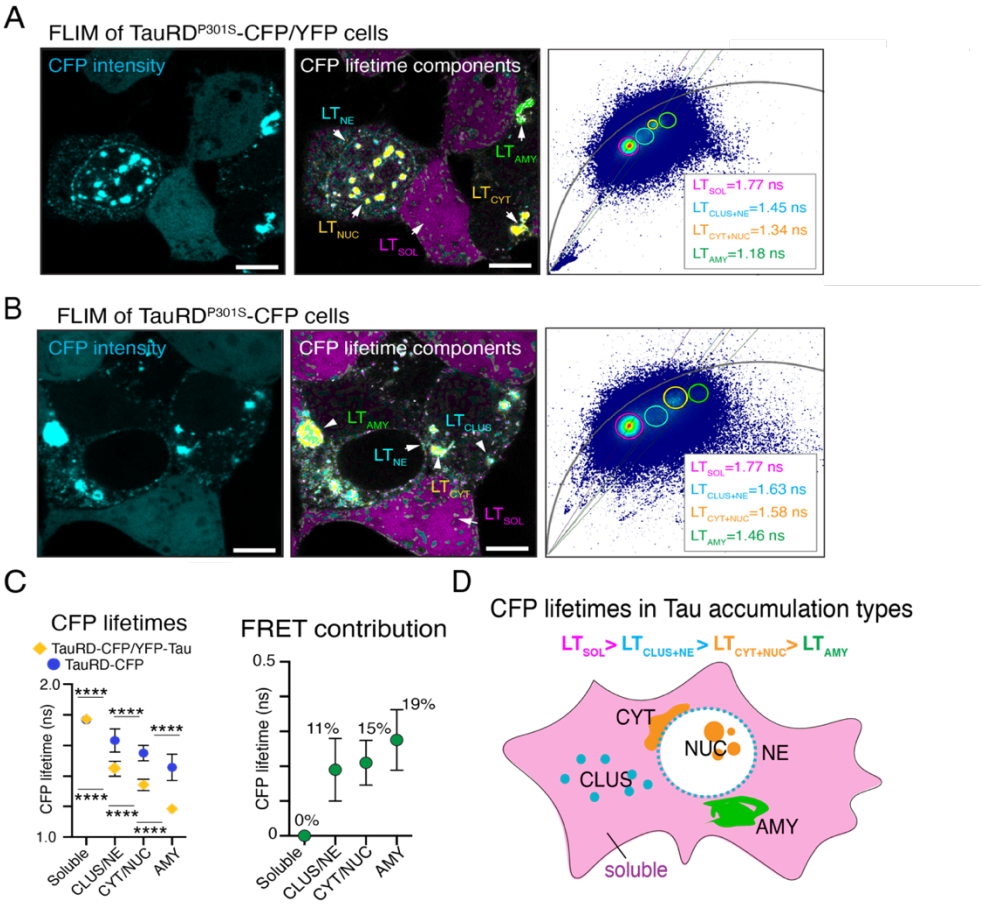

Figure 18. FLIM measurements of TauRD^{p301S}-CFP and TauRD^{p301S}-CFP/YFP in HEK sensor cells. (A) Confocal image and FLIM analysis of HEK sensor cells expressing TauRDP301S-CFP/YFP. The left image presents a representative confocal image of CFP fluorescence intensity. The right image displays the phasor mask overlaid on the confocal image, with each color representing a ROI selected on the corresponding phasor plot. The phasor plot on the right exhibits all measured CFP fluorescence intensities in the image, with each fluorescent lifetime (LT) assigned to a specific pixel. Longer LTs are represented on the left-hand side of the phasor plot, while shorter LTs are on the right-hand side. (B) Representative confocal image, phasor-mask overlay, and corresponding phasor plot for HEK sensor cells expressing TauRDP301S-CFP. (C) CFP LTs and FRET efficiency for TauRD-CFP and CFP/YFP Tau accumulations in HEK sensor cells. Both cases display a similar decrease in CFP LT, with the shorter LT in the TauRD-CFP/YFP case resulting from FRET addition. The right graph illustrates the FRET contribution to the loss of CFP fluorescence LT, calculated between cells expressing TauRD-CFP/YFP and TauRD-CFP. (D) Schematic representation depicting the relationship between CFP LT and Tau accumulation types. (Scale bar in images = 5µm)

As previously mentioned, a reduction in fluorescent LT can also occur independent of FRET. Thereby, the molecular density and a reduction of rotational freedom of the FP play a role. A specific confirmational order of the appearing Tau accumulations could be the cause of LT reduction of CFP independent of the acceptor fluorophore and FRET. Therefore, HEK-sensor cells only expressing TauRD-^{P301S}-CFP were analyzed as well (Figure 19B). The fluorescent LTs showed similar decrease between the different forms of Tau accumulations with LT_{SOL} = 1.77±0.03 ns for soluble Tau in the cytoplasm, $LT_{CLUS/NE}$ = 1.63±0.08 ns for NE and CLUS accumulations, $_{LTCYT/NUC}$ = 1.58±0.07 ns for NUC and NE and finally LT_{AMY} = 1.46±0.08 ns for presumably amyloid-like aggregates. Yet, when compared to the Tau accumulations of TauRD^{P301S} -CFP/YFP, they showed longer lifetimes due to the lack of FRET contribution (Figure 18 C).

Interestingly, the FRET efficiency of Tau accumulations between TauRD^{P301S}-CFP/YFP and TauRD^{P301S}-CFP was relatively minimal (Figure 18 D). Soluble Tau demonstrated no FRET (0%), which is in accordance with the FRET principle, as energy transfer necessitates proximity between molecules. CLUS/NE accumulations exhibited a 11% FRET contribution to the decrease in CFP lifetime, as opposed to 14% for CYT/NUC, suggesting a slightly reduced packing density, consistent with the hypothesis that CLUS/NE accumulations serve as an antecedent stage of more advanced Tau aggregates. As anticipated, the amyloid-like Tau accumulations displayed the highest FRET efficiency at 19%, attributable to their increased packing density.

These findings indicate that the reduction in CFP fluorescent lifetime is not predominantly due to energy transfer between donor and acceptor molecules; rather, it is determined by the conformational packing density of Tau within each type of accumulation.

In summary, both TauRD^{P301S}-CFP/YFP and TauRD^{P301S}-CFP expressing cells, AMY accumulations are characterized by the highest FRET and CFP-lifetime reduction, implying immobility, and dense packing of Tau molecules within, a characteristic feature of Tau amyloid-like aggregates. In contrast, CYT and NUC

display diminished FRET and CFP-lifetime, suggesting that these types of accumulations are less densely packed, likely representing amorphous (non-amyloid) aggregates. CLUS and NE Tau demonstrate even lower FRET and CFP-lifetime reduction, indicative of a reduced Tau density and some molecular mobility within a condensed liquid- or gel-like state of Tau.

6.1.1ODT of cellular Tau accumulation reveals their mass densities.

As the FLIM-FRET measurements revealed accumulation-specific CFP fluorescence lifetimes coupled with lower FRET efficiency, it was posited that these accumulations exhibit variations in mass density, transitioning over time from a more fluid-like state to a more solid, amyloid-like conformation. To investigate this hypothesis, the application of optical diffraction tomography (ODT) was pursued. ODT is a non-invasive imaging modality that quantifies the angular deviation of light traversing through the sample (Figure 19).

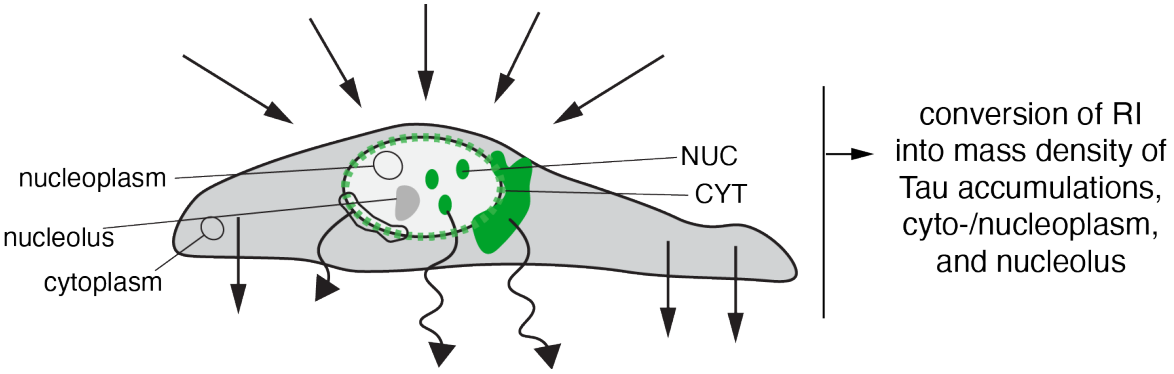

Figure 19. Principal of ODT applied to TauRD^{P301S} HEK sensor model. Schematic Illustration of principal Optical diffraction Tomography (ODT). Accurate determination of mass and density of Tau accumulations by using the refractive Index (RI) because of linear proportionality of RI to mass density of biological specimens. The measured RI is then transformed to 2D-phase tomograms which are then subsequently reconstructed to one 3D-tomogram of the entire cells. Fluorescent imaging in parallel enables determination of density and protein concentration of Tau accumulations within the cell.

By employing this technique, it is possible to accurately determine mass and density parameters, given that the RI value in biological specimens demonstrates a linear proportionality to the mass density of the material, with the proportional coefficient

represented by the RI increment α (Barer & Tkaczyk, 1954). To then calculate the density, approximate concentration and subsequently mass, the formular $n= n_{medium}+ αC$ was used, where n = measured RI in the ROI, n_{medium} = RI of the assay medium, α = RI increment and C = mass density in the ROI.

Due to the inherent nature of the reconstructed tomograms derived from ODT data analysis, which are phase images, the identification and characterization of cellular structures based solely on the tomogram can be a challenging task. To address this issue, fluorescence images of TauRD^{P301S}-CFP/YFP (YFP signal) and SiR-DNA-staining's were meticulously aligned with the corresponding reconstructed tomograms. This approach ensures the presence of reliable landmarks, thereby enabling precise quantification of protein density and concentration within the cellular context (Figure 20).

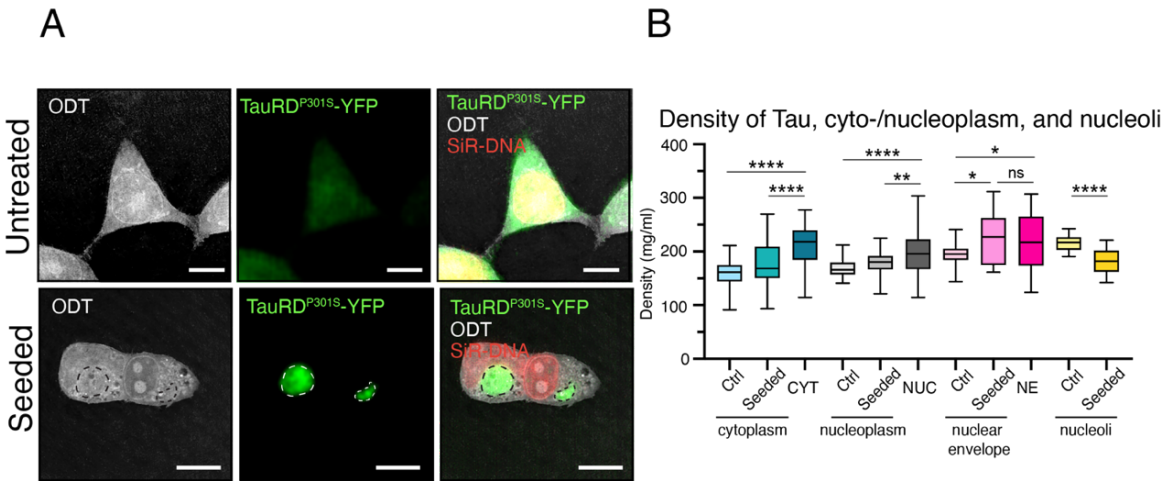

Figure 20. ODT of TauRD^{P301S} reveals accumulation specific densities. ODT analysis of HEK-sensor cells expressing TauRDP^{301S}. (A) Representative 3D reconstructed tomograms and confocal images of seeded and non-seeded cells. ROIs for density measurements were first taken from corresponding fluorescent image and then aligned with the corresponding tomogram (white/black dashed outlines). Sir-DNA staining was performed in parallel to visualize nuclei as landmarks for aligning purposes and for nuclear Tau accumulations. (Scale bar = 5 µm). (B) Calculated densities for Tau accumulation types CYT and NUC as well as the cytoplasm and nuclear space around Tau accumulations. For technical reasons NE accumulations could not be precisely measured, which is why ROIs of nuclear envelopes of seeded and non-seeded cells were compared instead. (Stastical significance was assessed by ordinary one-way ANOVA with, ** p≤ 0.01 and **** p≤0.0001).

In the TauRD^{P301S}-YFP channel, ROIs were delineated for CYT and nuclear NUC Tau accumulations. Subsequently, the average RI values were obtained from the optical ODT tomograms, which facilitated the calculation of mass density and the

approximation of protein concentration. The mean mass density for CYT Tau and NUC accumulations was found to be 212±38 (mean±SD) mg/ml and 218±51 mg/ml, respectively. These values demonstrated a significant increase compared to the adjacent cytoplasmic (177±40 mg/ml; $p<0.0001$; one-way ANOVA) and nucleoplasmic (179±22 mg/ml; $p=0.008$) regions (Figure 20 B).

Attributable to the technical constraints inherent in the custom microscopy setup used, the precise delineation of CLUS and NE Tau accumulations proved unattainable due to the low signal-to-noise ratios present in the fluorescence images. However, larger ROIs encompassing nuclear envelopes in both seeded and non-seeded HEK-sensor cells were selected for measurement and comparison. Remarkably, a global elevation in density was observed in the seeded HEK cells, registering values of 225±46 mg/ml (ne_{dens}) for nuclear envelopes in seeded cells and 196±19 mg/ml for control cells ($p=0.024$; one-way ANOVA), signifying that NE Tau accumulations possess a greater density than the nuclear envelope itself (Figure 20 B).

Intriguingly, the density of the nucleolus, an additional nuclear structure, exhibited a decrease in the presence of Tau accumulations; no_{dens}: 181±26 mg/ml in cells with NUC Tau and 215±15 mg/ml in control cells, $p=0.0007$).

Intriguingly, a comparative analysis of the cytoplasm (cyt_{dens}) and nucleoplasm (nuc_{dens}) densities in cells with or without accumulations (excluding Tau accumulations from the selected ROIs) demonstrated an inclination for elevated density in cells containing Tau accumulations (Figure 20 B; mean±SD, cyt_{dens}: 177±40 mg/ml in cells with CYT accumulations, and 162±23 mg/ml for control cells, $p=0.12$; nuc_{dens}: 179±22 mg/ml in cells with NUC Tau and 169±15 mg/ml in control nuclei, $p=0.37$; one-way ANOVA). The presence of Tau accumulations appears to correspond to an augmentation in overall biomolecular crowding by approximately 10-20 mg/ml.

In summary, CYT and NUC Tau accumulations possess a higher mass density than their respective surrounding cellular environment.

Furthermore, the emergence of Tau accumulations seems to coincide with an enhancement in cyto- and nucleoplasm density, which could have implications for numerous molecular processes. Additionally, ODT has been demonstrated to be a valuable tool to study protein aggregation in a cellular context, allowing for a more accurate assessment of protein characteristics.

5.3 Investigating the maturation of Tau condensates in vitro.

5.3.1 FLIM and FLIM/FRET of Tau condensates

Tau accumulations in HEK sensor cells expressing TauRD^{P301S} have demonstrated not only the sequential appearance of distinct Tau accumulation types over time, but also unique physical characteristics associated with each type, such as protein diffusion rates and protein concentration, as well as density. However, the underlying mechanisms or processes driving these changes in each Tau accumulation remain elusive (Figure 21).

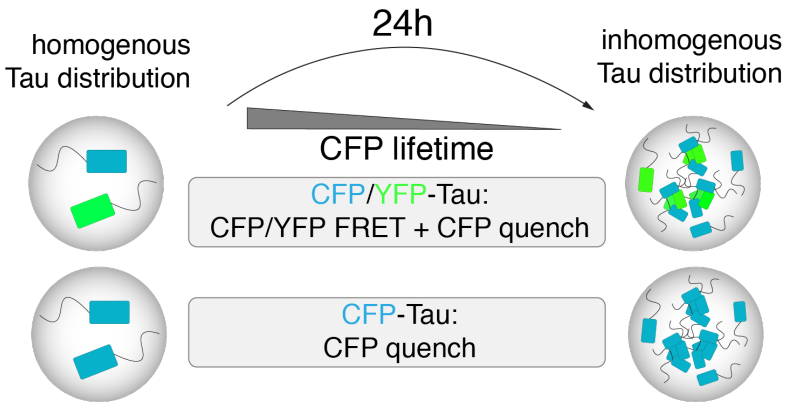

Figure 21. Principle of FLIM in in vitro condensates. Schematic illustration explaining the principle of FRET and self-quenching in in vitro Tau condensates. A higher concentration of CFP-Tau and YFP-Tau or CFP-Tau only, causes loss of fluorescent signal/CFP Lifetime due to FRET or self-quenching occurring.

To gain a deeper understanding of the properties of Tau accumulations found in the HEK sensor cell model, an in vitro model of LLPS was utilized. This approach was designed to study Tau condensates that mirror the various types of observed

accumulations to a certain degree. The advantage of in vitro experiments is their controlled and isolated nature, which removes the potential interference from complex cellular processes that could impact the way aggregation occurs.

Various forms of Tau assembly – diffused soluble Tau, liquid-like Tau condensates, and amyloid Tau fibrils – have been identified in vitro. Fibrillar aggregates of Tau are distinguished by pronounced Tau-Tau interactions and a compact, regular arrangement of Tau repeat domains (Fitzpatrick et al., 2017). Conversely, condensates involve multivalent Tau-Tau interactions of a weaker nature, which permit a degree of conformational flexibility and mobility for individual Tau molecules (Wegmann et al., 2018). As condensates age, molecular mobility, as assessed by fluorescence recovery after photobleaching (FRAP), diminishes (Hochmair et al., 2022). This indicates a transition from a liquid to a gel state ("hardening"), which might involve an increase in molecular density and a reconfiguration of Tau molecules that hampers their mobility.

To investigate whether these structural transformations within maturing Tau condensates correlate with a reconfiguration of Tau molecular orientation and potentially spatial density observed in HEK sensor cells, condensates were generated utilizing an equimolar mix of CFP-tagged Tau and YFP-tagged Tau (1:1) in the presence of polyA RNA and 5% PEG8000. The CFP fluorescence lifetimes were quantified via FLIM (as for the HEK cells) at distinct time points post-formation: 1 hour, 4 hours, and 24 hours, respectively (Figure 22,23).

Interestingly, each Tau condensate showed three distinct subpopulations of CFP lifetimes, revealing different phases within the condensates. The "dilute phase" consisted of the low salt buffer, PEG, soluble Tau, and RNA, while the "dense phase" comprised condensates with a high concentration of Tau and RNA. Within the dense phase, a subpopulation known as the "core" demonstrated even shorter CFP lifetimes, indicating a further compaction and solidification of the condensate.

Notably, the 1-hour-old Tau condensates exhibited a lower CFP lifetime for the dense phase (LT_{dense} = 1.4±0.1 ns) compared to the dilute phase (LT_{dilute},1h = 1.7±0.1 ns), confirming FRET occurring in the condensate, indicating the tight packing of Tau within the condensates. The LT_{core} showed an even further decrease

in CFP lifetime to 1.2±0.1 ns. Importantly, these lower CFP lifetimes were rare and present in small numbers within the 1-hour condensates, indicating a homogeneous distribution of Tau within the condensates (Figure 22 A).

Moreover, measurements were conducted on Tau condensates containing only CFP-labeled Tau to assess self-quenching effects. As expected, the 1-hour-old CFP-only Tau condensates displayed much higher CFP fluorescent lifetimes: LT_{dilute} = 3.7±0.2 ns, LT_{dense} = 2.4±0.1 ns, and LT_{core} = 2±0.3 ns. Interestingly, the CFP lifetimes for the dilute phase were much higher compared to CFP/YFP-labeled Tau condensates, indicating FRET occurring even outside the Tau condensates.

Furthermore, CFP lifetime measurements were performed on CFP/YFP-Tau 4-hour-old condensates: LT_{dilute} = 1.7±0.1 ns, LT_{dense} = 1.4±0.1 ns, and LT_{core} = 1.2±0.1 ns (Figure 22B). There was no significant difference between the 1-hour and 4-hour condensates, indicating that the packing of Tau within the condensates did not appear to change over the first 4 hours. Similar trends were observed in CFP-only Tau condensates, with LT_{dilute} = 2.9±0.1 ns, LT_{dense} = 2.3±0.0 ns, and LT_{core} = 1.9±0.1 ns.

Notably, the CFP lifetimes of the CFP/YFP-Tau 24-hour-old condensates showed significant differences compared to the 1-hour and 4-hour condensates: LT_{dilute} = 1.4±0.1 ns, LT_{dense} = 1.2±0.1 ns, and LT_{core} = 1.0±0.02 ns ($p < 0.0001$; two-way ANOVA). Furthermore, the lifetime of soluble CFP-labeled Tau in the dilute phase decreased after 24 hours (LT_{dilute},24h = 1.4±0.1 ns), suggesting the formation of soluble dimers or oligomers.

Moreover, like the 1-hour and 4-hour Tau condensates, the 24-hour CFP-only Tau condensates exhibited an overall decrease in CFP lifetime. However, in comparison to the condensates containing both CFP and YFP-labeled Tau, the CFP-only condensates displayed higher lifetimes (LT_{dilute} = 2.7±0.1 ns, LT_{dense} = 2.1±0.03 ns, and LT_{core} = 1.7±0.02 ns). These findings suggest a higher packing density throughout the condensate due to the absence of FRET and the occurrence of self-quenching.

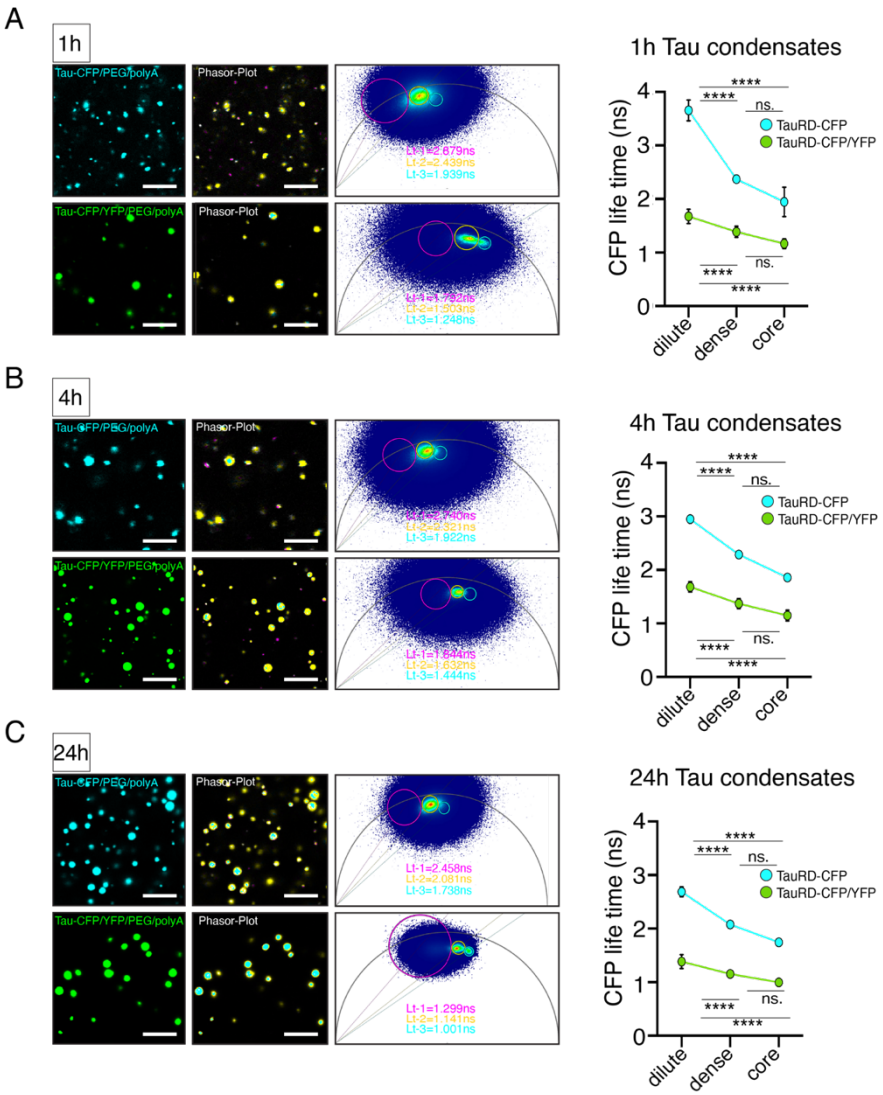

Figure 22. FLIM Measurements of aged Tau condensates. FLIM measurement of CFP- and CFP/YFP Tau condensates at different time points (1h,4h,24h). (A) confocal Image of Tau condensates with CFP-Tau in cyan and CFP/YFP-Tau condensates in green. Phasor Plot and corresponding Phasor Mask are shown respectively. ROI´s selected in the phasor plot are shown in fluorescent image via the phasor mask with the corresponding colors. Tau condensates show CFP lifetime reduction between dilute and dense phase. Small number of Condensates showed core subpopulation with lower LT indicating higher packing. (B) and (C) depict representative confocal images of 4h and 24h Tau condensates for CFP- and CFP/YFP-Tau respectively. 24h condensates not only appear bigger but also show larger amount of CFP lifetimes within core subpopulation indicating a solidifying of the condensates. (Scale bars = 5 µm; stastical significance was assessed by ordinary two-way ANOVA with, *** p≤ 0.001 and **** p≤0.0001)

When comparing the FRET contributions, a noticeable 7% increase in FRET contribution between the 1-hour and 24-hour dense phase of the condensates was observed, indicating a restructuring phenomenon within the condensates (Figure 23 B). Intriguingly, there was also a parallel 7% increase in FRET contribution within the core population, further supporting the hypothesis that Tau condensates increase in viscosity over time, from the center outwards. Notably, a reduction in FRET contribution was noted in the dilute phase, potentially linked to the incorporation of additional soluble Tau molecules from the surrounding milieu into the condensates. This phenomenon could lead to a reduction in the crowdedness of the solution, resulting in a decrease in the FRET signal between CFP- and YFP-labeled Tau.

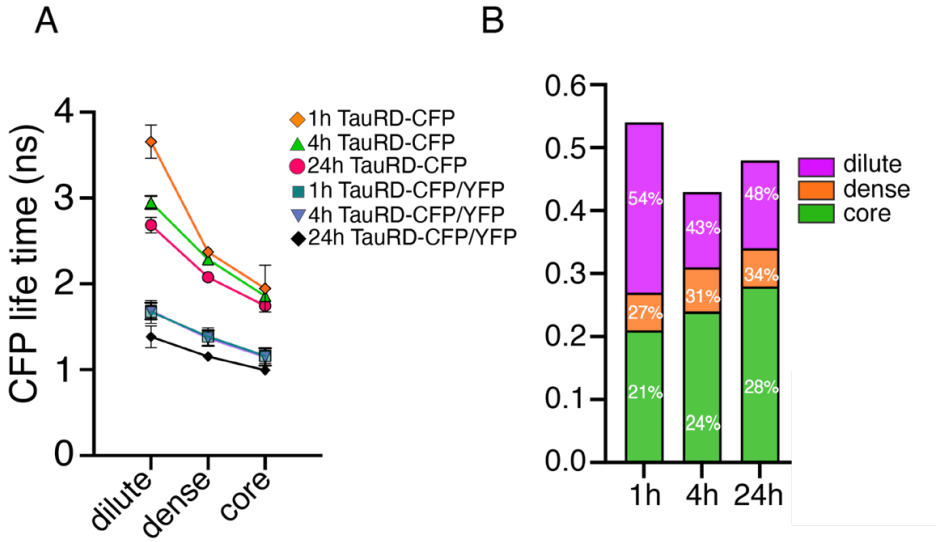

Figure 23. FLIM and FRET Measurements of Tau condensates. Collective graph of CFP and CFP/YFP-Tau condensates at 1h, 4h and 24h after preparation. (A) CFP lifetime measurements of dilute, dense and core phase of Tau condensates for CFP and CFP/YFP-Tau at 1h,4h,24h. Drop in CFP lifetime between the two populations is due to FRET occurring. (B) FRET contribution to CFP lifetime decreases across all three CFP lifetime populations for each Tau condensate timepoint.

To summarize, the observed self-quenching of CFP-Tau and the measured FRET using FLIM (Figure 23 A) collectively suggest the occurrence of a restructuring process within the Tau condensates. However, FLIM alone cannot provide a detailed understanding of the exact changes happening to Tau within the condensates, as factors such as salt concentration, RNA interaction, and pH can influence FLIM measurements and are not taken into consideration.

5.3.2 ODT reveals restructuring of Tau condensates during maturation.

To expand our understanding of the distinct CFP lifetimes associated with each Tau condensate, as indicated through the FLIM and FRET analyses, ODT was employed. This method, previously used in the HEK cells expressing TauRD^{P301S}-CFP/YFP, provides precise measurements of mass density, which in turn offers insights into relative protein concentration. This should enhance one's comprehension of the structural modifications occurring during the aging process of Tau condensates. Based on the FLIM assessments, indications of alterations in the density within the condensates could be anticipated.

Considering that the condensates appear to exhibit denser packing, an overall increase in both density and protein concentration in the 24-hour condensates is likely. To assess potential shifts in molecular density within aging Tau condensates, ODT was employed and procured RI tomograms for in vitro Tau condensates. As for the FLIM experiments these condensates were formulated under the influence of RNA and crowding agents (specifically, 25 µM YFP-Tau, 10 µg/ml polyA, 5% PEG8000) and observed at distinct maturation phases – 1 hour, 4 hours, and 24 hours post-preparation (Figure 24). To dissect the nuances of the Tau condensates, two investigative approaches were employed, each capitalizing on the layer-by-layer, 2D tomograms generated through ODT. The first method involved assessing the protein concentration or density within a selected 0.5 µm slice of the Tau condensate's equatorial plane. This assessment used the "clockscan" tool and cross-sectional profiles within the ImageJ software.

The second strategy focused on a more comprehensive view of the condensate. It entailed calculating the average RI values for each layer or plane within the Tau condensate. Summing up these RI values, the total volume, mass, and concentration of the complete condensate was then analyzed. By combining these two methods, it provided a more complete picture of Tau's distribution within the condensates.

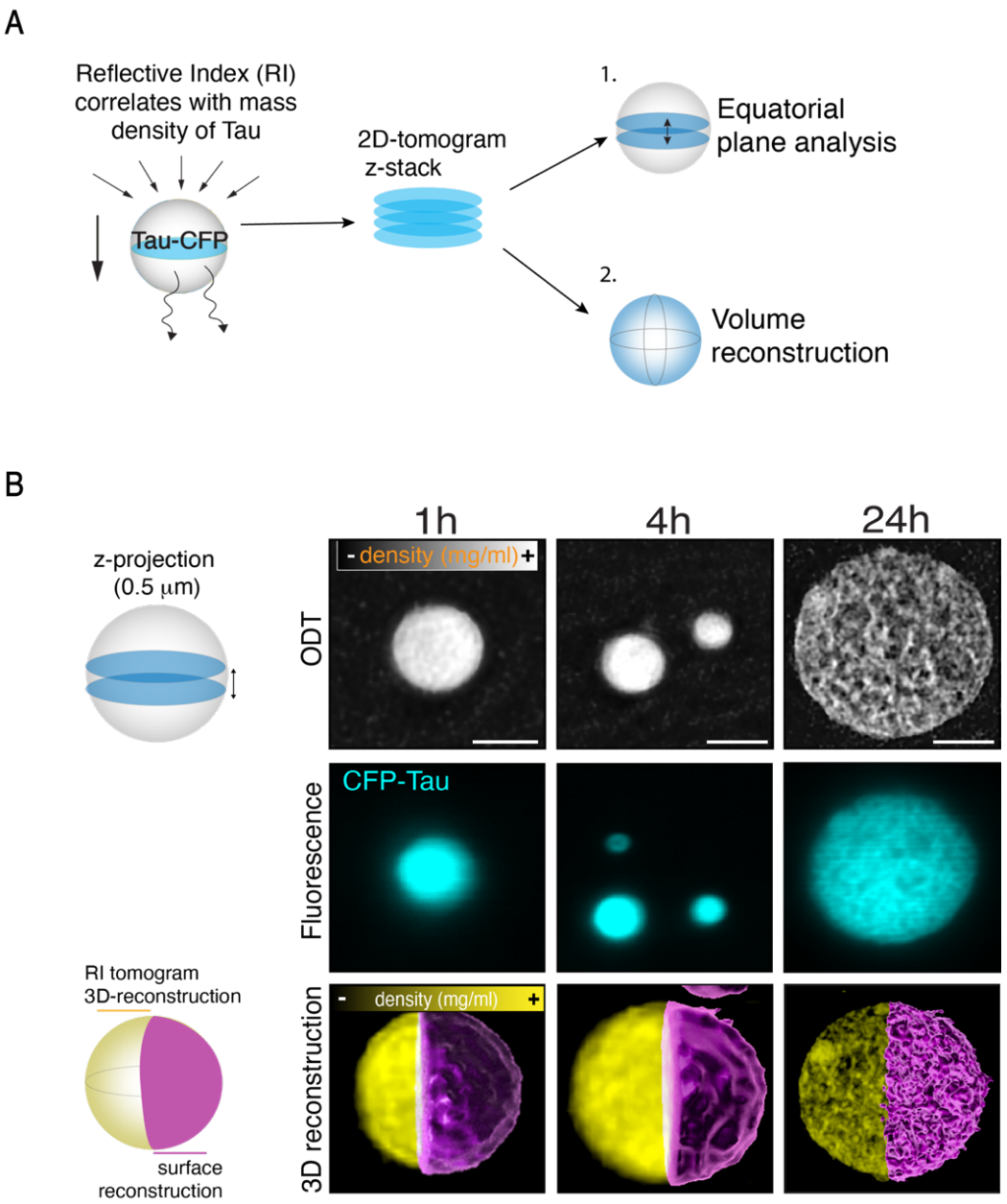

Figure 24. ODT Measurement and 3D reconstruction of Tau condensates. (A) Schematic showing ODT acquisition and analysis of Tau condensates. Condensates were analyzed either by measuring protein concentration/density within equational planes (0.5μm) (1) or by calculating mass, density, and volume of the entire Tau condensate (2). (B) Representative ODT tomogram (grey images) and fluorescence (cyan images) of 1h,4h and 24h Tau condensates, as well as their 3D IMARIS reconstruction showing the imaged 2D RI in yellow and the 3D modeled surface in purple.

ODT, as demonstrated in Figure 25, offers a visualization of the interior of Tau condensates compared to conventional fluorescence microscopy. Utilizing IMAIRS

software for 3D reconstruction of these ODT images, distinct changes in the Tau condensate surfaces, among the three types examined, appeared.

5.3.2.1 Analysis of Tau density distribution within Tau condensates

For Tau condensates at 1-hour old, the 3D-reconstructed ODT tomograms indicated a uniform density distribution both within the interior and across the surface of the condensates (Figure 24 B). When examining the 4-hour old condensates, the surface displayed sizable “wrinkles,” while the interior displayed a subtly granulated appearance.

In contrast, the internal distribution of material within the 24-hour old condensates was uneven, presenting a fibrillar network structure. This structure contained nodes of higher density interspersed with empty spaces, creating a semblance to a porous particle. Correspondingly, the surface of these aged condensates appeared granular.

As detailed in Figure 25 A and B, insights into the distribution of materials within Tau condensates can be gleaned from cross-sectional profiles and radial distribution plots taken from the equatorial plane, specifically at a thickness of 0.5 µm. Condensates at the 1-hour and 4-hour mark showed a uniform distribution of material, though a gradual increase in central mass density was observed over time (with mass density (MD), given as mg/ml; mean±SD): MD at 1h = 197.9±19.7, MD at 4h = 234.3±27.2, with a p-value of $p<0.0001$.

Intriguingly, a considerable proportion of the 24-hour old condensates (~80%) displayed significantly lower central mass densities (MD at 24h = 128.8±44.2; p-value vs MD at 1h = $p<0.0001$, p-value vs MD at 4h = $p<0.0001$). They also exhibited a larger diameter and an uneven material distribution. This heterogeneity in material distribution is discernible in the profile plots of equatorial plane projections, where dense nodes with higher density alternate with low-density regions (Figure 25 A, 26) as well as the high standard deviation of the radial density (Figure 25 B).

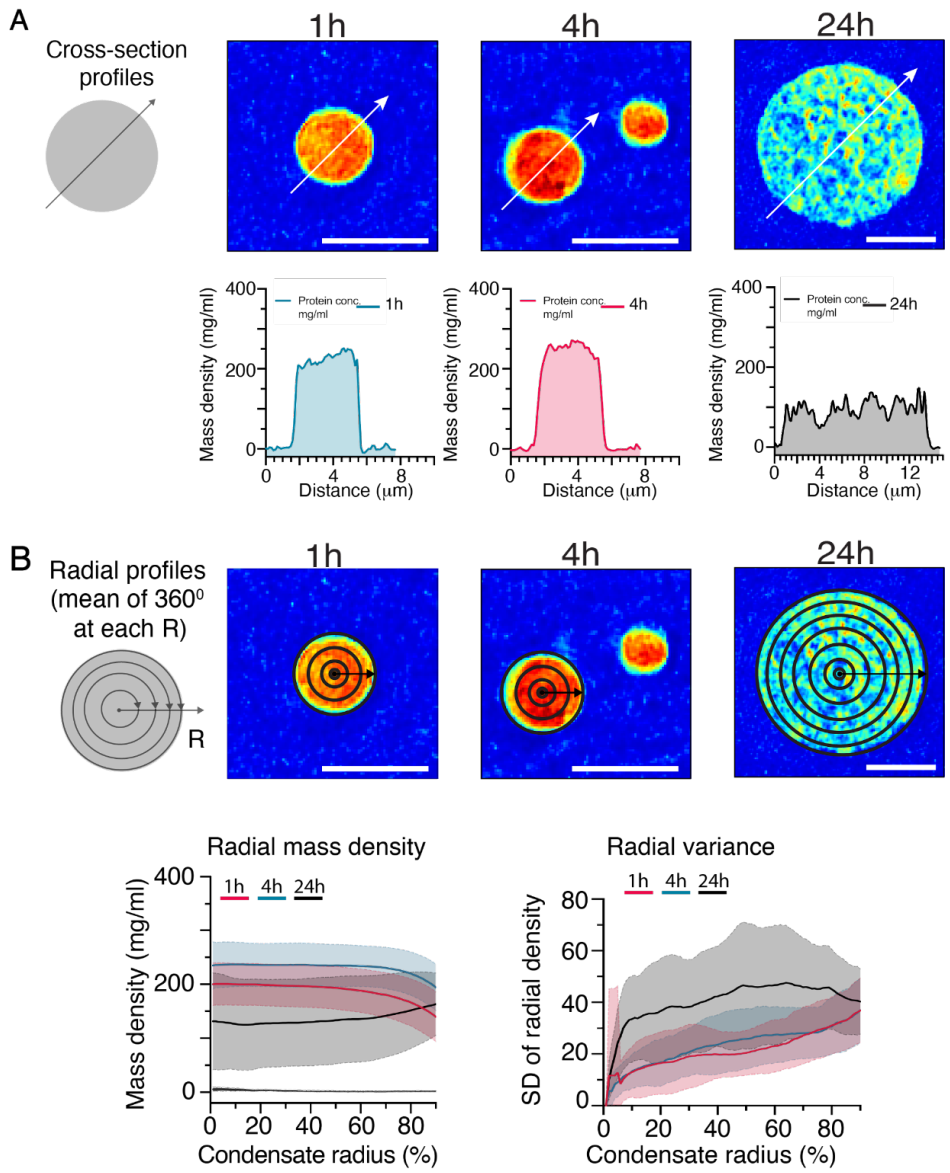

Figure 25 I Density measurements of Tau condensates
(A) Cross-section profile analysis of ODT tomograms of Tau condensates. (top) representative images of single plane ODT tomograms of 1h,4h and 24h old Tau condensates. White arrow indicates RI measurements of Plot-Profile analysis using ImageJ. (Bottom) Calculated mean mass density across single plane image. 1h and 4h Tau condensates show similar condensate size and concentration (mg/ml), whereas 24h condensates show lower concentration and larger size. (B) Clock-scan analysis of equatorial section of Tau condensates. (top) representative ODT images showing “max z-projection” of equatorial planes and subsequently clockscan analysis through ImageJ plugin. (bottom) (left) Graph shows calculated mean density (mg/ml) of Tau condensates from the center of the condensates to the periphery. (bottom) (right) Graph displays the SD´s of clockscan measured rings, displaying variance of measured densities across condensates, visualizing heterogenous distribution of Tau within 24h old condensates. (Scale bars in images = 5μm)

This pattern suggests the evolution of a fibrillar network within the condensates, characterized by pores roughly 2 μm in diameter and fibrils of around 0.8 μm in

thickness. Importantly, 24-hour old Tau condensates show a pronounced propensity for “seeding” Tau aggregation both in vitro and within Tau sensor cells (Figure 13). This suggests that the observed transformation within the condensates could be associated with the generation of seeding-capable, beta-structured Tau material.

5.3.2.2 Full volume analysis of Tau condensates

The observed density and distribution of Tau within 24-hour-old condensates surprisingly appeared to be lower compared to the 1-hour and 4-hour-old condensates, despite their larger size (almost three times as big). This unexpected finding led to the hypothesis that Tau undergoes a shift from a homogeneous distribution to a more heterogeneous distribution within the condensates. This hypothesis is supported by the high variance observed in Figure 26B, indicating an uneven distribution of RI values and, consequently, a heterogeneous density distribution. This could explain how the average density of Tau in the equatorial plane of the 24-hour-old condensates was significantly lower compared to the earlier time points. To comprehensively characterize the change in distribution within the condensate, a full volume analysis of the condensates was performed, taking the total amount and volume into consideration (Figure 26).

The Data obtained from whole condensate volume analyses (Figure 26 A) revealed an increase in total concentration with 136 mg/ml for 1h condensates to 168 mg/ml for 4h condensates, however they also revealed a loss of total concentration for the 24h condensates with 118 mg/ml, while the volume continued to increase (0.04 pl^3 to 88.6pl^3). Interestingly, when comparing the total mass of the condensates an overall increase can be observed with 1.7 pg for 1h, 11.6 pg for 4h and 62.8 pg for 24h condensates. This overall indicates a net gain of material per condensate in 24-hour-old condensates compared to those at 1 hour and 4 hours. Interestingly, it is worth noting that while the mass and volume of the 1-hour and 4-hour condensates demonstrate an almost linear increase in a codependent manner, a subtle deviation is observed in the 24-hour condensates. In contrast, these 24-hour condensates

exhibit a smaller mass despite the increasing volume, suggesting a loss of material over time.

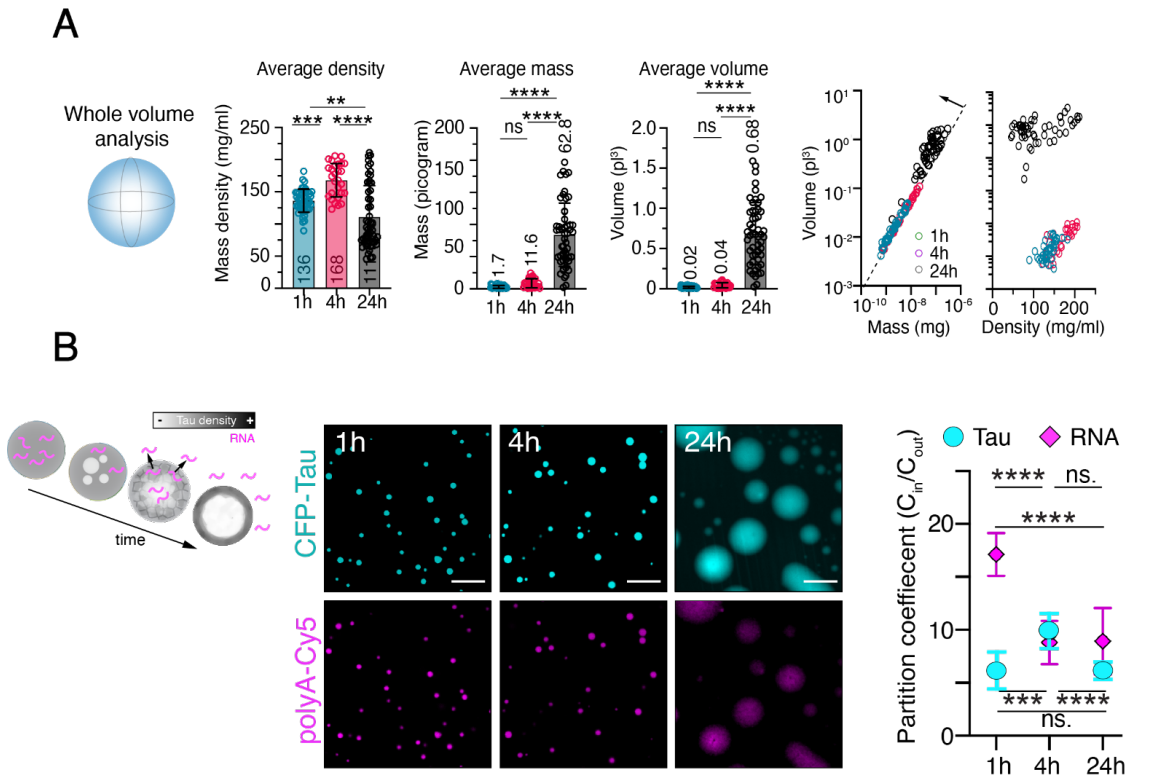

Figure 26. Full Volume analysis of Tau condensates. (A) Results obtained from the full volume analysis of Tau condensates using ODT, focusing on the volume, mass, and density of condensates at different time points (1h, 4h, and 24h). The graphs present the calculated volume (pl), mass (pg), and density (mg/ml) for each condensate. Remarkably, the 24h old Tau condensates exhibit a notable decrease in density, while displaying significantly larger volumes and total masses. This suggests a potential restructuring or redistribution of material within the condensates over time. insights into the partition coefficients of Tau and RNA across the different Tau condensates. The left panel depicts a model illustrating the redistribution of RNA outside the condensates as the condensates age. Representative confocal images in the middle panel show the colocalization of CFP-Tau and Cy5-polyA within the condensates at 1h, 4h, and 24h time points. The right panel presents the calculated partition coefficients, indicating the distribution of Tau and RNA between the fluorescent signal inside and outside the condensates (stastical significance was assessed by ordinary one-way ANOVA with, *** p≤ 0.001 and **** p≤0.0001).

It is noteworthy that Tau condensates formed in the presence of RNA and PEG. The decrease in mass density observed in 24-hour-old Tau: RNA condensates could be attributed to a decrease in the concentration of Tau or RNA, or both, within the condensates. Therefore, to investigate whether Tau or RNA concentrations are changing, condensates were formed using CFP-Tau in the presence of fluorescently labeled RNA (1% Cy5-labeled polyA). Their partition coefficient in the dilute phase

and inside the condensates were compared at 1h, 4h, and 24h (Figure 26 B). Interestingly, 1h old Tau condensates showed not only high amounts of Tau in the condensates but also RNA, which plays a role in catalyzing Tau LLPS and potentially fibrillization. In comparison to the 4-hour-old condensates, a significant loss of RNA within the condensates is observed in the 24-hour-old condensates. Furthermore, the 24-hour-old Tau condensates exhibit a further redistribution of Tau molecules from within the condensates to the dilute phase. This structural conversion may signify the formation of amyloid-like Tau fibrils, providing an explanation for how liquid-like Tau condensates can catalyze Tau aggregation. Notably, the Tau: RNA-containing condensates at this stage contain seeding competent material capable of initiating Tau accumulation and aggregation in cells (Hochmair et al., 2022; Prince et al., 2023).

In summary, the findings of this study reveal a notable structural transition that occurs as Tau condensates age, resulting in self-restructuring and the formation of filamentous Tau networks. This structural transformation provides a potential explanation for the different manifestations of Tau accumulations observed in HEK cells expressing TauRD^{P301S}. It is plausible that Tau transitions from a more soluble state (CLUS) to a more solid-like state (CYT, NUC), which is supported by the protein concentrations measured using ODT. Moreover, the results underscore the reliability and accuracy of ODT as a valuable tool for characterizing Tau condensate formation and accurately quantifying protein concentrations. However, the precise effects and interactions of these Tau accumulations remain unknown and require further investigation.

5.4 Association of Tau accumulations with cytoplasmic and nuclear structures and organelles

5.4.1 Association of Tau accumulations with the cytoskeleton

Following the insights gained from ODT and FLIM-FRET experiments, which elucidated potential mechanistic underpinnings of Tau accumulation formation in

HEK cells (CLUS, CYT, NE, NUC). The subsequent objective was to probe the potential interaction partners of these accumulations within the cellular milieu. Unraveling the intricate molecular mechanisms through which Tau disrupts cellular functions and characterizing its protein-protein interactions are imperative for comprehending its pathogenic role.

Confocal z-stack imaging, a powerful technique, facilitates the acquisition of a series of optical sections at distinct focal planes, enabling three-dimensional reconstruction of target protein distribution and localization. This approach allows for the visualization of colocalization events across multiple focal planes, unraveling the intricate spatial relationship between Tau and the proteins of interest. Complementing this, StED imaging, a super-resolution technique surpassing the diffraction limit of conventional confocal microscopy, bestows enhanced spatial resolution. StED imaging yields sharper images with minimized optical blurring, enabling meticulous assessment of colocalization events at the nanoscale. By synergistically employing confocal z-stack imaging with StED imaging, information from z-stack images and the superior spatial resolution achieved by StED, facilitate a comprehensive analysis of colocalization.

To investigate the interaction between Tau and the cytoskeleton, experiments focusing on its association with microtubules as well as its interactions with actin (Cabrales Fontela et al., 2017) and vimentin (Cabrales Fontela et al., 2017; Capote & Maccioni, 1998) were conducted. Following the established protocols, HEK cells were seeded with Tau condensates, fixed, and subjected to immunostaining for tubulin, actin, and vimentin. Confocal z-stack imaging was performed to capture the 3D structure of the cells with various Tau accumulations, and subsequent reconstruction was carried out using IMARIS software (Figure 27). The 3D reconstruction of Tau accumulations provided valuable.

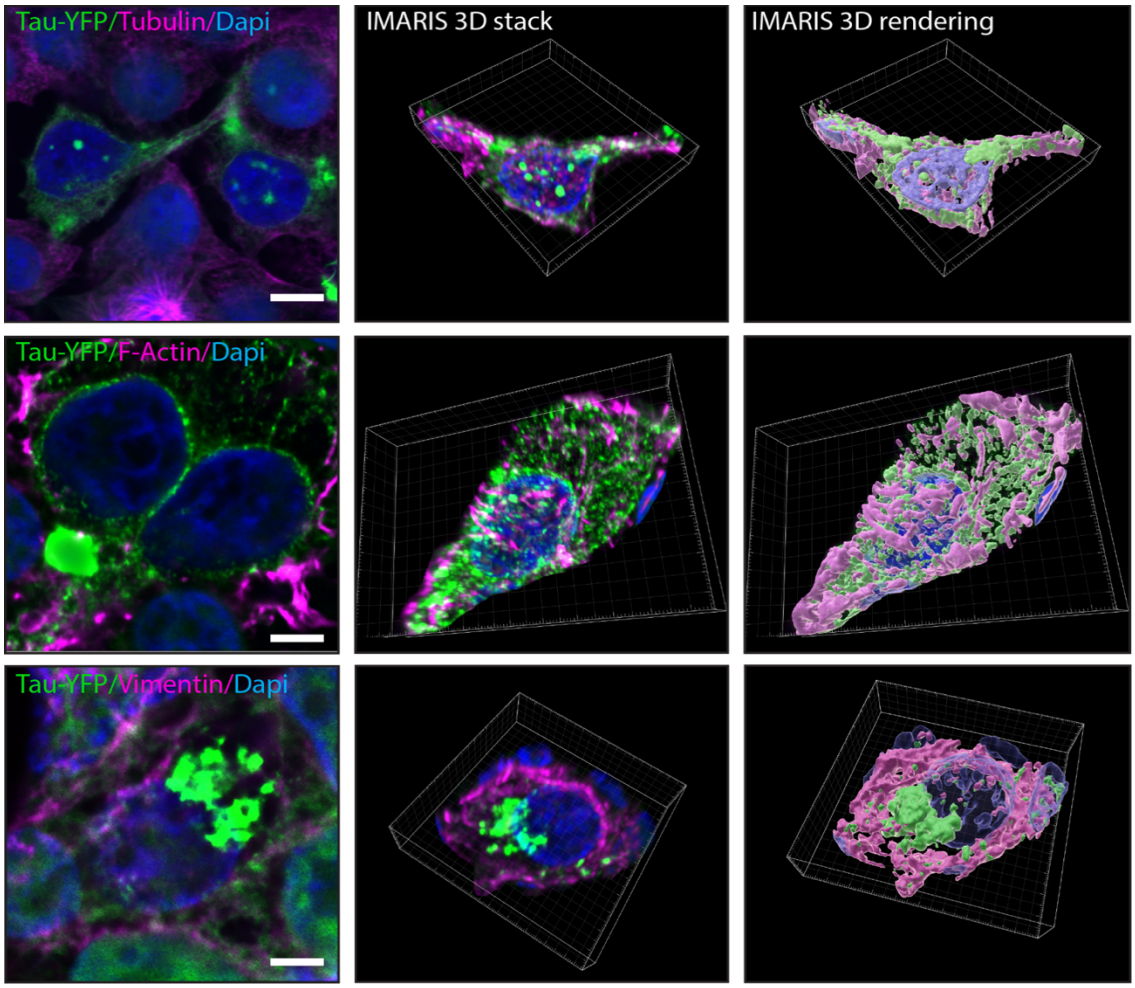

Figure 27. 3D reconstruction of Tau accumulations in HEK cells. Representative images of 3D reconstruction of TauRDp301S-CFP/YFP co stained with cytoskeletal markers tubulin, actin,vimentin. Z-stack confocal images were taken and further processed through surface reconstruction using IMARIS software. Panels show representative images of acquired single plane confocal image then a z- projection of the z-stack and finally the reconstructed surfaces of Tau and the respective staining. (Scale bars in the images = 5µm).

insights into the cellular distribution of Tau and its potential interactions with the cytoskeleton. The reconstructed surfaces revealed a significant overlap of Tau with tubulin and vimentin around the nuclear envelope, indicating a potential interaction at these sites. In contrast, the interaction pattern with actin did not show a specific pattern based on the reconstruction. To quantitatively analyze the interactions between Tau and the cytoskeleton, a colocalization analysis was conducted. In colocalization analysis, two prominent methods are commonly used: the object-based approach and the intensity-based approach.

The object-based approach involves analyzing the structural overlap of defined ROIs to determine colocalization. This method relies on the 3D reconstruction of the fluorescent signals, such as using software like IMARIS, to generate surfaces representing the objects of interest, in this case, Tau accumulations and the cytoskeletal components. By comparing the spatial overlap of these reconstructed surfaces, colocalization can be assessed. However, one challenge with this approach is the subjective nature of selecting intensity thresholds to generate the reconstructed surfaces, which can introduce potential bias.

On the other hand, the intensity-based approach focuses on comparing the fluorescent intensity values between the two channels to determine colocalization. This method involves analyzing the pixel intensities within the same voxel of each channel and evaluating the degree of correlation between the intensities. If there is a high degree of correlation, it suggests colocalization of the proteins of interest. The advantage of the intensity-based approach is its quantitative nature, as it directly compares the fluorescence signals without relying on subjective thresholding. This approach allowed to assess colocalization by examining the overlapping fluorescent signals between Tau and the cytoskeleton, considering adjacent signals as potential indications of their interaction (Figure 28).

Colocalization analysis revealed distinct patterns of interaction between Tau and different cytoskeletal components. As anticipated, a significant association between Tau and tubulin was observed, with Tau appearing to align along microtubules as indicated by the white arrowheads. Interestingly, Tau condensates (CLUS) exhibited a close association with microtubules, while the Tau accumulations in the cytoplasm (CYT) seemed to exert pressure on microtubules, displacing them and occupying cellular space. StED imaging further supported these findings by showing CYT Tau accumulations occupying cellular space negative for tubulin (Figure 29 A). Additionally, it showed that CYT and CLUS accumulations of Tau present in a fibrillar phenotype, which was not visible with laser scanning confocal microscopy due to the resolution limitation, suggesting that the earlier forms of Tau accumulations might have protofibril properties, which could explain the high seeding potency.

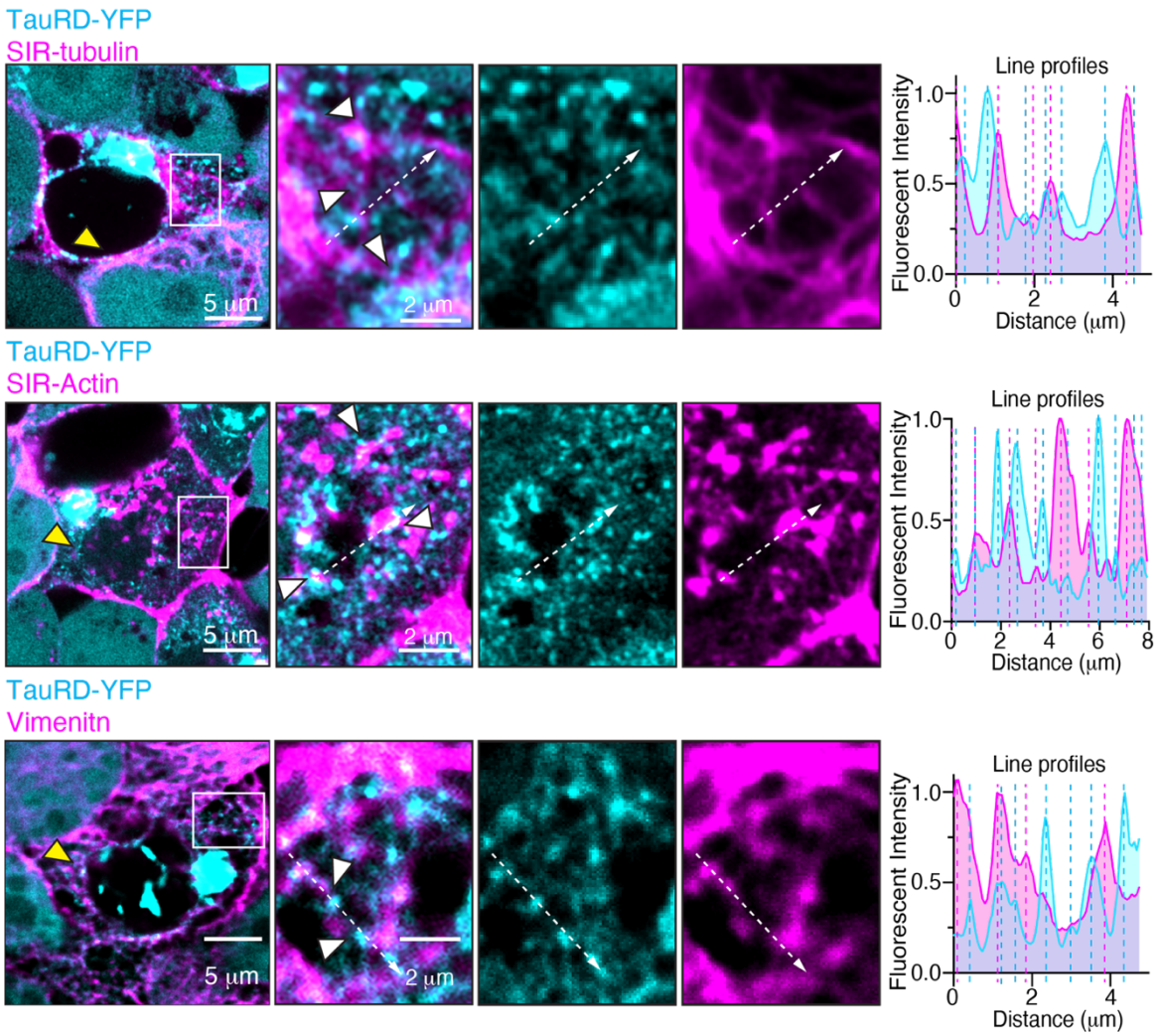

Figure 28. Line profile analysis of Tau and the cytoskeleton. Representative laser scanning confocal images of Tau (cyan) and Cytoskeletal marker (pink), tubulin, actin, and vimentin. From left to right: Representative overlay of co staining between Tau and Tubulin/actin/vimentin, zoom ins showing overlay and respective channels of CLUS Tau accumulations and tubulin/actin/vimentin with white line indicating where Line plots were analyzed. The graph shows the fluorescent signal of the individual channel measured across the white dashed line. Fluorescent peaks in proximity indicate colocalization between Tau and co-stained protein. (Scale bars = 5 µm and 2µm for zoom-ins).

In contrast, the interaction between Tau and actin appeared to be more random, with no clear colocalization pattern. Notably, Tau CLUS showed affinity for actin nodes but not actin branches, suggesting a limited influence of Tau on actin filament formation.

Noteworthy interactions were observed between Tau and vimentin, with small Tau condensates situated between vimentin nodes along the filaments, indicating potential influence on the vimentin network or intermediate filaments in general.

When closer examined with StED, it showed small fibrillar Tau aligning with vimentin across the branches as well as filling the spaces in between, further supporting the colocalization results (Figure 29 B).

These observations suggest that Tau may impact the organization and function of vimentin filaments. It is important to consider that actin filaments predominantly run at the periphery of the cell, while tubulin and vimentin have been observed along the nuclear envelope. Remarkably, closer examination of the nuclear envelope revealed a high colocalization between Tau, tubulin, and vimentin (yellow arrow heads), whereas no colocalization with actin was observed.

This suggests that Tau accumulations at the nuclear envelope may disrupt normal nuclear transport by binding to vimentin and tubulin, potentially interfering with their roles in the transport process.

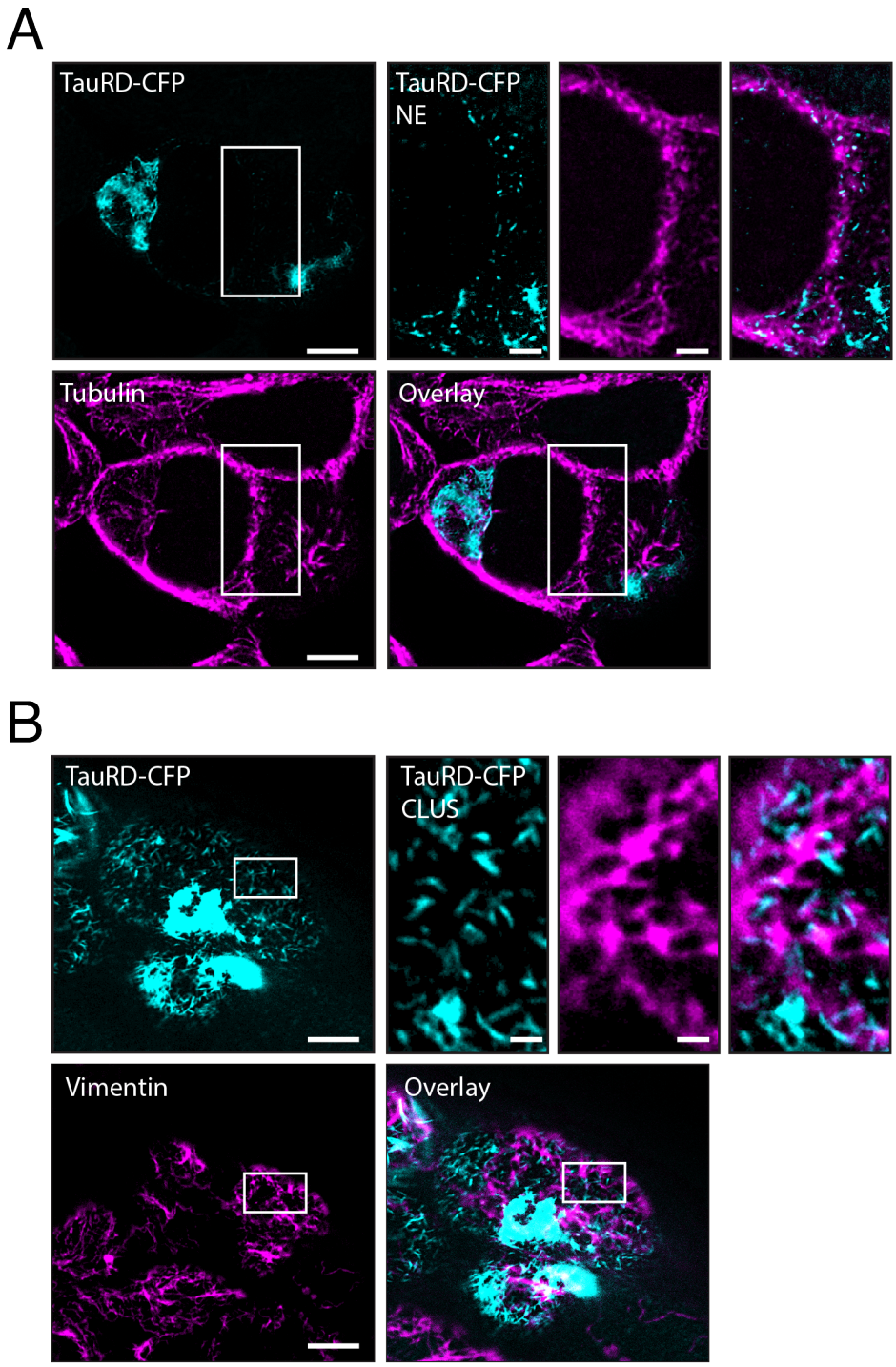

Figure 29. STED images of TauRD expressing HEK cells stained for cytoskeleton.
(A) Representative STED image of HEK cells expressing TauRDp301S -CFP/YFP. Fluorescent signal of Tau and tubulin shown in cyan and pink. Tau is shown to colocalize with tubulin around the nucleus and CYT Tau accumulations show no signal for tubulin. (B) Representative STED images of co-staining of Tau and Vimentin with fluorescent signals for Tau and Vimentin being shown in cyan and pink respectively. Tau is shown to form around vimentin network, as well as in between spaces of vimentin nodes. Furthermore, STED images of both conditions reveal fibrillar structure of small Tau accumulations (CLUS) in the cytoplasm. (Scale bars =5 μm and 2μm for the zoom-ins).

5.4.1.2 Nocodazole / Latrunculin Treatment confirms binding of Tau clusters to microtubules, not F-actin.

To validate the co-localization findings of Tau with the cytoskeleton and investigate its binding to tubulin and actin, two chemical agents capable of disrupting these structures were employed. Nocodazole, an antineoplastic agent, was used to interfere with microtubule polymerization. Although it is primarily employed for cell cycle arrest by affecting spindle formation during mitosis at low doses, higher concentrations of nocodazole reversibly impede Tau polymerization (Qiang et al., 2018).

On the other hand, Latrunculin A, a naturally occurring toxin extracted from specific sponges (Latrunculia and Negombata), binds to actin monomers near the nucleotide binding cleft, preventing actin polymerization (Fujiwara et al., 2018).

It is important to note that there is currently no commercially available reagent known for disrupting Vimentin, which is why its investigation was not included in this study.

To investigate the binding affinity of Tau to tubulin and actin, HEK cells were transfected with 24-hour-old Tau condensates and subsequently treated with either nocodazole or latrunculin A for a 2-hour period prior to imaging. Tubulin and actin were labeled using a live dye (sir-Tubulin/Actin), and the cells were then subjected to imaging and analysis. The number of Tau CLUS accumulations within a defined area was compared between treated and untreated cells (Figure 30 A and B).

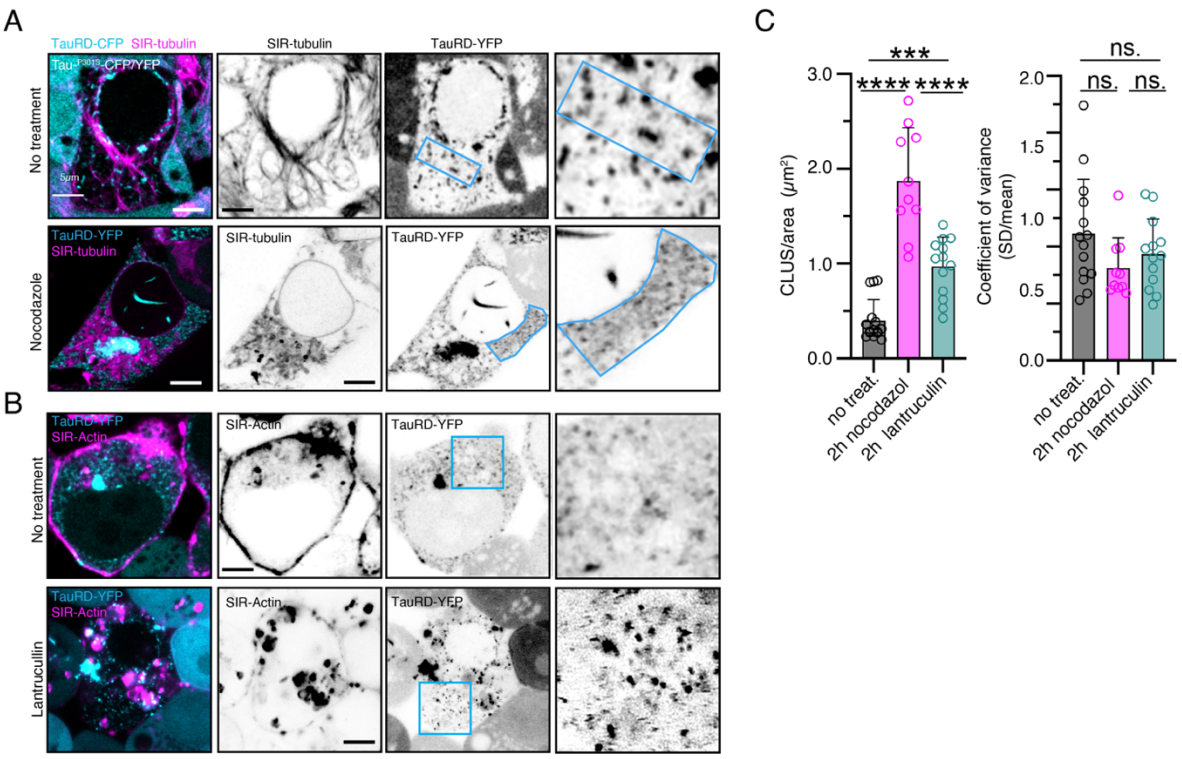

Figure 30. Colocalization analysis of nocodazole/latrunculin A treated HEK cells. (A)+(B) Representative confocal images of Tau cluster analysis done on untreated and nocodazole/latrunculin A treated TauRD expressing HEK cells. From left to right: overlay confocal image of Tau (cyan) and Tubulin/actin (pink) fluorescent signal, inverted black and white images of each channel respectively, zoom in of analyzed ROI used for Cluster Analysis. (C) Cluster Analysis graphs representing the number of Tau CLUS/μm^2 and the coefficient variance (CV) for untreated and nocodazole/latrunculin A treated cells. Analysis revealed upon treatment, the number of Tau CLUS in the cytoplasm increases by two-fold for latrunculin treated cells and four-fold for nocodazole treated cells. Treated cells show lower CV than non-treated cells, which is coherent with the increase in Tau CLUS numbers. (Scale bars = 5μm) (stastical significance was assessed by ordinary one-way ANOVA with, *** p≤ 0.001 and **** p≤0.0001).

The obtained data confirmed that upon nocodazole treatment, there was a significant increase in occurrence of small Tau CLUS accumulations in the cytoplasm of treated cells compared to untreated cells (1.9 ± 0.6 CLUS/μm^2 to 0.4 ± 0.2 CLUS/μm^2, $p<0.001$ of one-way ANOVA), confirming strong binding affinity of Tau to Tubulin. The observed increase in CLUS Tau accumulations can be attributed to the recruitment of released Tau molecules (Figure 30 C).

Treatment of HEK cells with latrunculin A, which disrupts actin polymerization and leads to the release of Tau into the cytoplasm, also resulted in an increase in CLUS numbers (0.9 ± 0.3 CLUS/μm^2), although to a lesser extent compared to nocodazole treatment. These findings are consistent with my previous observations of

colocalization between Tau clusters and actin nodes. The depolymerization of actin by latrunculin A causes the release of Tau into the cytoplasm.
In addition, the coefficient of variation (CV) was assessed as a measure of variability in the mean intensity of Tau within the measured area. A lower CV indicates a more evenly distributed Tau signal within the cytoplasm, which is expected in nocodazole and latrunculin-treated cells due to the increased release of Tau. Although the CV values for nocodazole and latrunculin treatment did not significantly differ from those of non-treated cells, they showed a decrease of 0.8 ± 0.3 and 0.9 ± 0.3, respectively, compared to 1.2 ± 0.5 in control cells.
These findings confirm the colocalization and interaction of Tau with Tubulin and Actin and suggest that released Tau can bind to Tau CLUS accumulations.

5.4.2 Association of Tau accumulations with nuclear structures

My subsequent objective was to acquire a more holistic comprehension of the importance of perinuclear Tau accumulations, given their substantial colocalization with Tubulin and Vimentin in the vicinity of the nuclear envelope. Moreover, the investigation of perinuclear Tau accumulations has received comparatively less attention when compared to Tau aggresomes, making it a topic of considerable interest for the further characterization of Tau aggregation.
To achieve this, HEK cells were seeded with Tau condensates and subsequently performed IHC staining for Lamin-B1, an intermediate filament responsible for nuclear structural support, nuclear pore complex (NPC), which facilitates nuclear transport of proteins, and ultimately for nucleophosmin, a structure associated with ribosomal biogenesis.
Confocal z-stack imaging was performed to capture the 3D structure of the cells with Tau accumulations, and subsequent reconstruction was carried out using IMARIS software, as for the staining's of the cytoskeleton (Figure 31).
Significant overlap between Tau and Laminar and NPC staining was observed in the 3D reconstructions. Notably, Lamin, which provides internal support to the nucleus,

showed co-localization with Tau, suggesting that Tau enters the nucleus and binds to Lamin, potentially destabilizing the nuclear structure and leading to the formation of nuclear folds. This phenomenon has been previously reported in studies where Tau accumulations were observed in conjunction with nuclear folds (Diez & Wegmann, 2020).

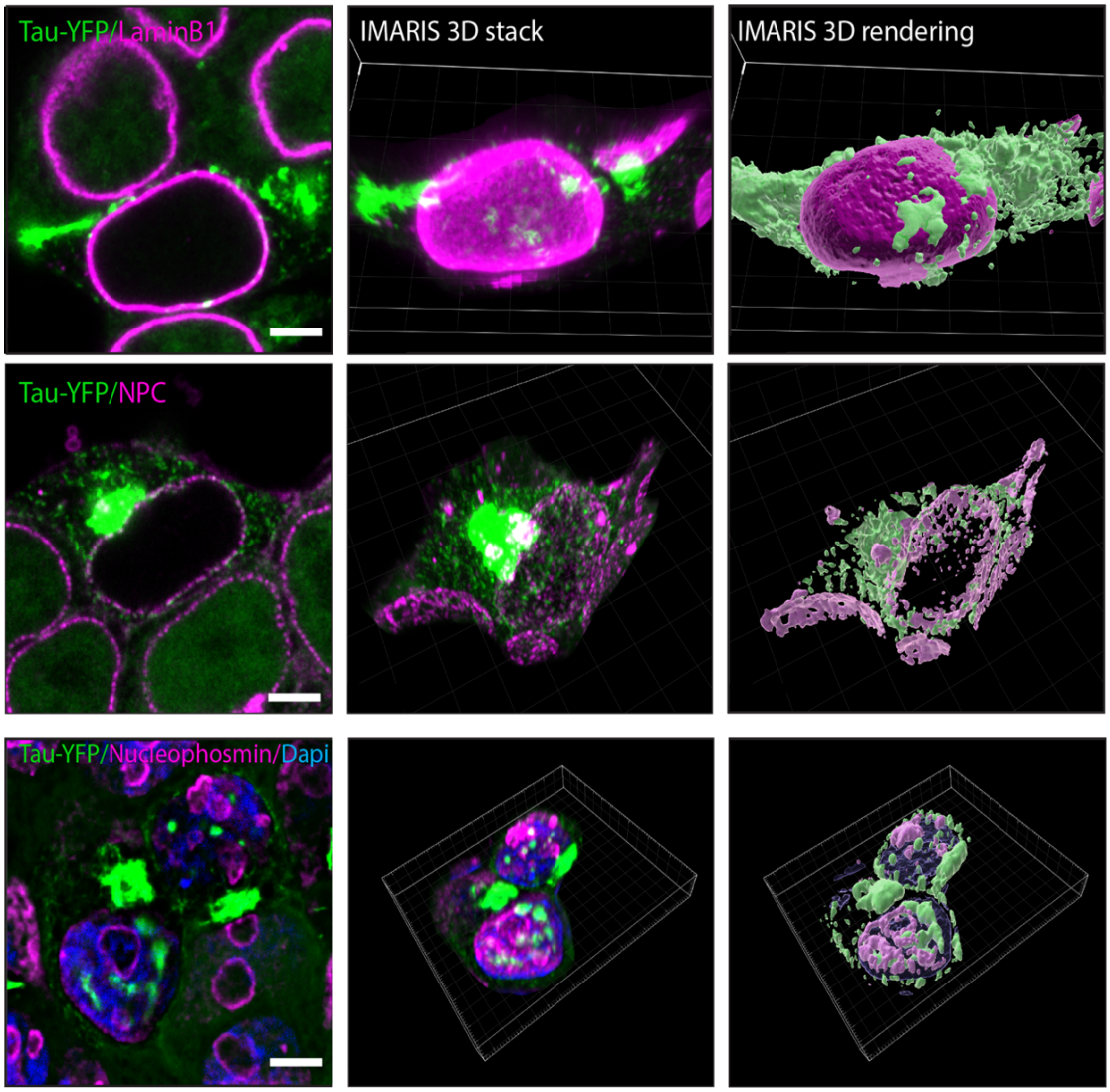

Figure 31. 3D reconstruction of Tau accumulations and nuclear structures. Representative images of 3D reconstruction of TauRDp301S-CFP/YFP (green signal) co-stained with nuclear structures lamin-B1, NPC and Nucleophosmin (pink signal). Z-stack confocal images were taken and further processed through surface reconstruction using IMARIS software. Panels show representative images of acquired single plane confocal image then a z- projection of the z-stack and finally the reconstructed surfaces of Tau and the respective staining. (Scale bars in the images = 5µm).

The co-localization of Tau with NPC further supports this observation, indicating that Tau may obstruct the nuclear pores, impeding the import and/or export of molecules. Interestingly, although Tau interacts extensively with RNA, it does not exhibit significant colocalization with nucleophosmin, responsible for ribosomal biogenesis.
To perform a quantitative analysis of the 3D reconstructed surfaces using IMARIS, the same intensity-based colocalization analysis as previously done with the cytoskeleton IHC staining's was employed (Figure 32). The focus of my investigation was directed towards cells exhibiting perinuclear accumulations in the nuclear envelope (NE Tau accumulations) and within the nucleus (NUC Tau accumulations), aiming to unravel the interplay between Tau and nuclear proteins. As depicted in Figure 32, prominent Tau accumulations were observed within the nucleus (NUC), as well as around the nuclear envelope (NE). Colocalization analysis of Lamin demonstrated a significant overlap between Tau and Lamin, with Tau appearing to be situated within the Lamin structure, consistent with the findings from the 3D IMARIS reconstructions. To validate this colocalization, StED microscopy was employed, confirming the co-localization of Tau within the nuclear envelope, suggesting its potential interference with nuclear transport (Figure 33). To gain further insights into this phenomenon, a more detailed examination of the Nuclear Pore Complex (NPC) was conducted (Figure 33). Corresponding with the reconstructed surfaces, small accumulations of Tau were observed surrounding the entire nucleus, exhibiting a strong colocalization with the NPCs. StED microscopy confirmed this colocalization and revealed the close proximity of Tau around the nuclear envelope, indicating the possible obstruction or interference with the nuclear pores. Lastly, to investigate the interaction between Tau and nucleoli, considering its well-established association with RNA in the context of LLPS and disease, colocalization analysis on nucleoli staining's was performed. The results showed that Tau NUC AG accumulations tended to form around, but not near the nucleoli within the nucleus, confirming the findings obtained from the 3D reconstructions.
These findings suggest that Tau does not hinder RNA synthesis and transport directly but rather interacts with RNA itself. Additionally, these results strongly

support the hypothesis that Tau aggregation hinders nuclear transport and/or nuclear structure and function overall.

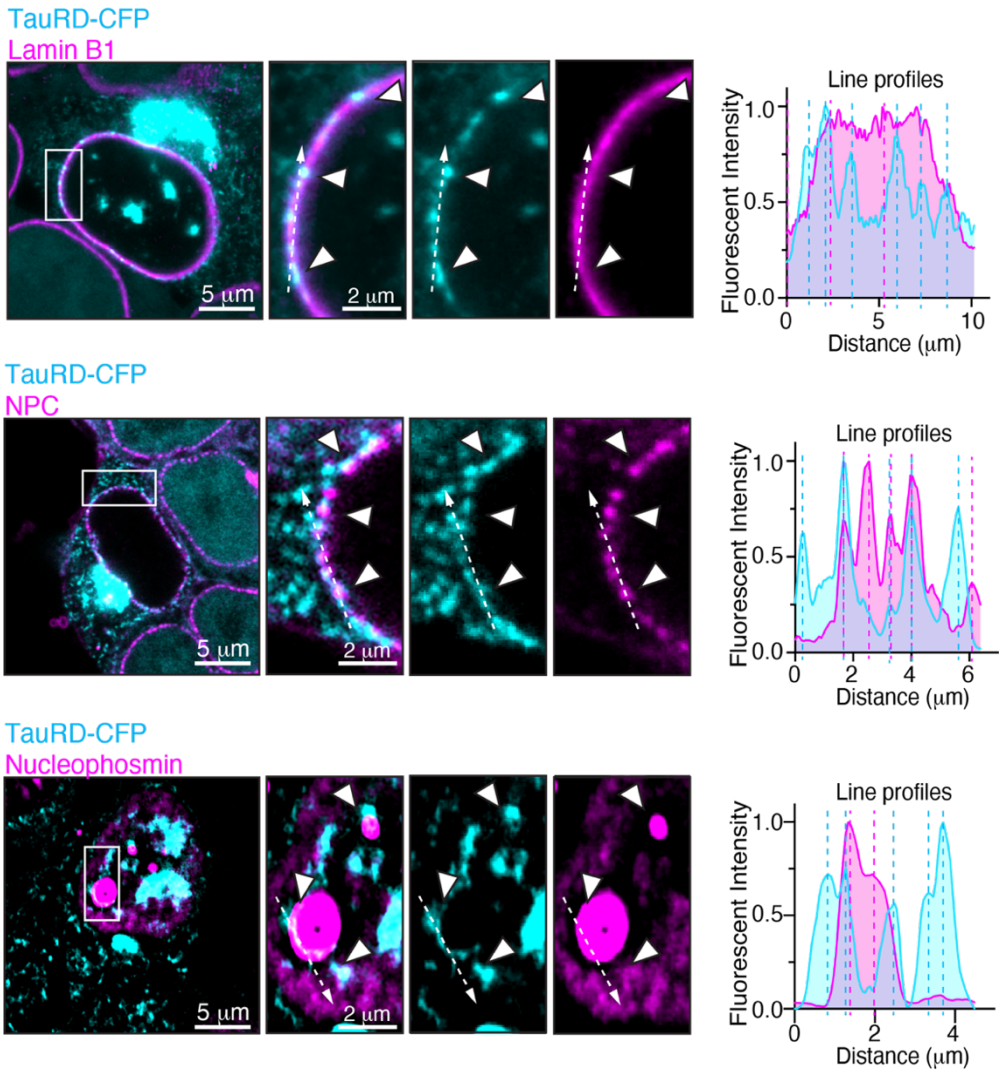

Figure 32. Line profile analysis of Tau and nuclear structures. Representative laser scanning confocal images of Tau (cyan) and nuclear structure(pink): Lamin-B1, NPC and nucleophosmin. From left to right: Representative overlay of co staining between Tau and Lamin/NPC/nucleophosmin, zoom ins showing overlay and respective channels of CLUS Tau accumulations and respective co-staining with white line indicating where Line plots were analyzed. The graph shows the fluorescent signal of the individual channel measured across the white dashed line. Fluorescent peaks in proximity indicate colocalization between Tau and co-stained protein. (Scale bars = 5 µm and 2µm for zoom-ins).

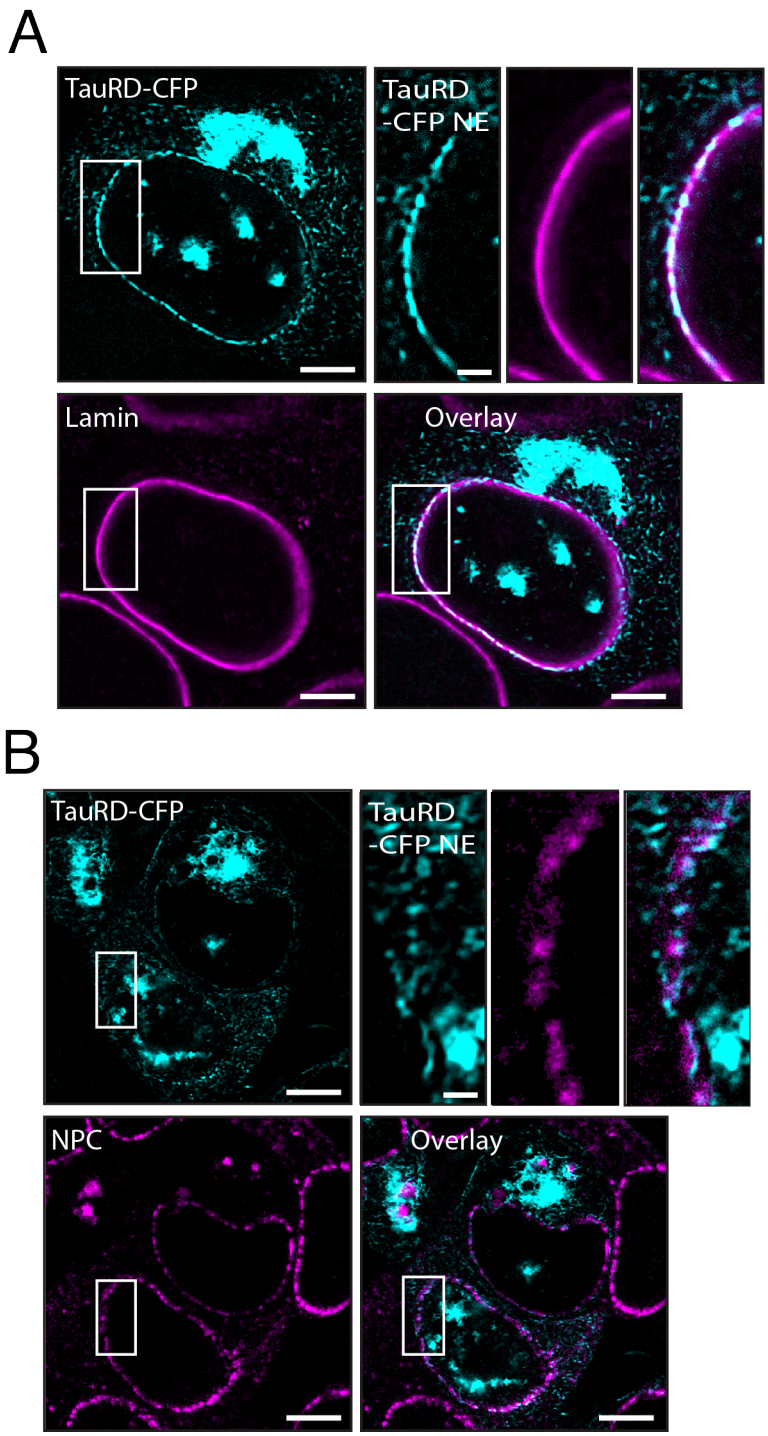

Figure 33. STED images of TauRD expressing HEK cells and nuclear structures. (A) Representative STED image of HEK cells expressing TauRD^{p301S}-CFP/YFP. Fluorescent signal of Tau and Lamin shown in cyan and pink. Tau is shown to colocalize with Lamin around the nucleus, on both the inside and outside. (B) Representative STED images of co-staining of Tau and NPC with fluorescent signals for Tau and NPC being shown in cyan and pink respectively. Tau is shown to colocalize with the NPC puncta on in- and outside. (Scale bars =5 μm and 2μm for the zoom ins).

5.4.3 Association of Tau accumulations with the endoplasmic reticulum

Since Tau appears to strongly colocalize with the cytoskeleton via tubulin, vimentin and actin, as well as nuclear structures such as Lamin and the NPC, the next aim was to characterize its interaction with the endoplasmic reticulum (ER) and mitochondria. Tau has emerged as a key player in the interaction with other cellular organelles, including ER and mitochondria. The ER is a multifunctional organelle involved in protein synthesis, folding, and calcium homeostasis. Perturbation of ER function and protein misfolding are prominent features in neurodegenerative disorders, including AD. Recent studies have revealed an intriguing association between Tau and the ER, suggesting a potential role in ER stress and protein aggregation. Tau has been shown to directly interact with ER components, such as the ER chaperones and calcium channels, leading to impaired protein folding and disrupted calcium signaling (Cieri et al., 2018). These interactions can trigger ER stress responses and activate downstream signaling pathways implicated in neurodegeneration.

Therefore, to study the interaction between Tau and the ER, two proteins associated with the ER, Sec61B and KDEL were selected.

Sec61B is a component of the Sec61 protein complex, which is involved in protein translocation across the ER membrane. The Sec61 complex forms a protein-conducting channel that allows newly synthesized proteins to be transported into the ER lumen or integrated into the ER membrane. It interacts with other components of the Sec61 complex to facilitate the proper insertion and folding of nascent polypeptides into the ER. This translocation machinery is essential for the correct targeting and processing of proteins destined for various cellular compartments, including the ER and beyond.

KDEL is a specific sequence of amino acids (Lys-Asp-Glu-Leu) that serves as a retrieval signal for proteins in the ER. Proteins containing the KDEL motif are typically resident ER proteins that are responsible for maintaining ER homeostasis and function. The KDEL signal interacts with specific receptors, such as the KDEL receptor (KDELR), allowing these proteins to be recognized and retrieved from the

Golgi apparatus and returned to the ER. This retrieval process ensures proper localization of ER proteins and helps maintain ER integrity.

Now to investigate now the ER, HEK cells transfected with 24-hour-old Tau condensates along with Sec61b-mapple or KDEL-mapple were employed, which allowed for visualization of the ER.

Colocalization analysis was performed using the "plot profile" function in ImageJ (Figure 34). The results revealed clear colocalization between Tau and both ER markers in the cytoplasm. Intriguingly, Tau seemed to localize in the interfold spaces of the ER, as indicated by the white arrowheads in the figure, and exhibited a wrapping pattern around the ER membrane. These findings suggest that Tau aggregation may potentially interfere with ER function, although it is also possible that Tau associates with other cytoplasmic proteins near the ER. To validate the authenticity of the colocalization between Tau and Sec61B/KDEL, we conducted ER bursting experiments. It has been previously demonstrated that exposing cells to a hypotonic solution leads to reversible disassembly of the ER into small vesicles, which can then reassemble upon returning to an isotonic solution (King et al., 2020). Therefore, we exposed HEK cells expressing Sec61B or KDEL and containing Tau condensates to a 10% hypotonic solution (10% cell media in water) for 5-10 minutes, followed by live cell imaging (Figure 35). Interestingly, even after hypotonic exposure and ER disassembly, Tau CLUS accumulations were still observed to colocalize with both Sec61B- and KDEL-positive cells, indicating a strong binding interaction between Tau and the ER membrane. It is important to note that further investigations are required to fully elucidate the interaction between Tau and ER, as the observed colocalization could be attributed to the adhesive properties of Tau aggregates.

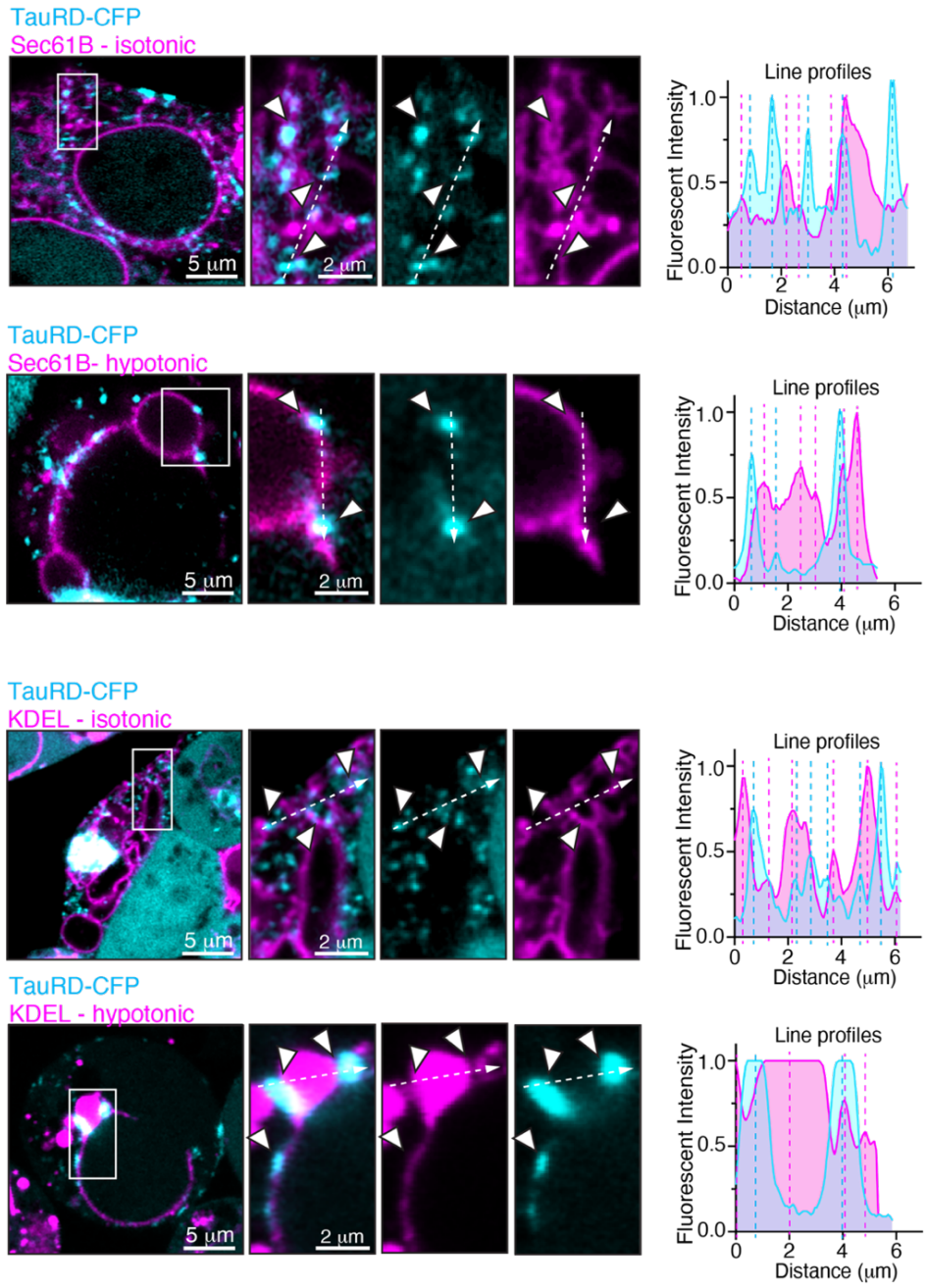

Figure 34. Line profile analysis of Tau and ER in isotonic and hypotonic solution. Representative laser scanning confocal images of Tau (cyan) and ER (pink): Sec61B and KDEL in isotonic and hypotonic cell media. From left to right: Representative overlay of co staining between Tau and Sec61B and KDEL either in isotonic solution or hypotonic solution (10% media), zoom ins showing overlay and respective channels of CLUS Tau accumulations and Sec61B and KDEL with white line indicating where Line plots were analyzed. The graph shows the fluorescent signal of the individual channel measured across the white dashed line. Fluorescent peaks in proximity indicate colocalization between Tau and co-stained protein. (Scale bars = 5 µm and 2µm for zoom ins).

5.4.4 Association of Tau accumulations with mitochondria

Tau has also been implicated in mitochondrial dysfunction, another critical aspect of AD pathogenesis. Mitochondria are essential for cellular energy production, calcium regulation, and apoptosis. Dysfunctional mitochondria and impaired energy metabolism have been observed in AD brains. Tau accumulation in mitochondria has been linked to mitochondrial impairment, including reduced ATP synthesis, altered mitochondrial dynamics, and increased oxidative stress (X. Wang et al., 2007). It has been shown to directly interact with mitochondrial proteins and affect their functions, leading to disrupted mitochondrial integrity and compromised neuronal viability.

To determine the colocalization of Tau CLUS accumulations with mitochondria, colocalization analysis was performed using the "Plot profile" function in ImageJ. HEK cells were co-transfected with 24-hour-old Tau condensates and an MTS-mscarlet mammalian vector, which enables visualization of mitochondria (Figure 35). The mitochondria targeting sequence (MTS) is a specific peptide sequence present in proteins that are targeted to the mitochondria. It serves as a signal for mitochondrial import and guides the protein to the mitochondrial matrix or other sub compartments within the mitochondria.

By fluorescently tagging MTS mitochondria can be visualized and tracked, providing a reliable marker for studying their localization and potential interactions with Tau CLUS accumulations.

Consistent with previous studies, the colocalization analysis revealed a direct interaction between Tau and mitochondria, as indicated by their proximity. The formation of Tau clusters around mitochondria suggests a binding affinity, where Tau aggregates adhere to the mitochondrial membrane. This observation raises the possibility of a direct interaction between Tau and the mitochondrial membrane, potentially affecting mitochondrial ion exchange and function.

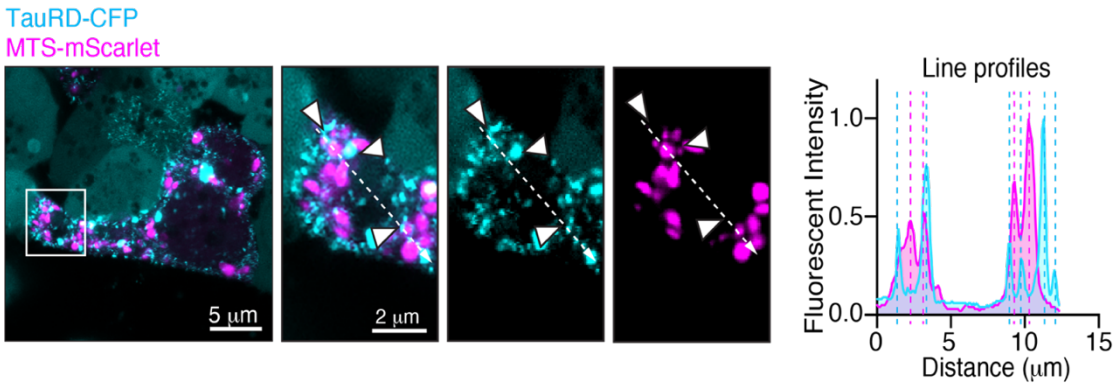

Figure 35. Line profile analysis of Tau accumulations and mitochondria. Representative laser scanning confocal images of TauRD^{p301S}-CFP/YFP (cyan) and MTS-mscarlet (pink). From left to right: Representative overlay of co staining between Tau and MTS, zoom ins showing overlay and respective channels for CLUS Tau accumulations and MTS with white line indicating where Line plots were analyzed. The graph shows the fluorescent signal of the individual channel measured across the white dashed line. Fluorescent peaks in proximity indicate colocalization between Tau and co-expressed MTS. (Scale bars = 5 µm and 2µm for zoom ins).

6 Discussion

In these studies, live-cell imaging revealed the temporal appearance pattern of four types of Tau accumulations: CLUS, NE, CYT, and NUC (Chapter 6.1). It was observed that soluble Tau in the cytoplasm and nucleoplasm undergoes re-localization upon aggregation (Chapter 6.1.1). Subsequently, the characteristics of different Tau accumulation types (CLUS, NE, CYT, and NUC) were characterized using advanced imaging techniques such as FRAP, FLIM-FRET, and ODT (Chapter 6.2).

FRAP analysis provided insights into the diffusion rates of TauRD-YFP molecules specific to each accumulation type, indicating variations in packing density (Chapter 6.2.1). Further investigation of packing density was done through FLIM-FRET analysis (Chapter 6.2.2), and the protein concentration of Tau accumulations was directly measured using ODT (Chapter 6.2.3). Additionally, this study compared and analyzed Tau condensates of different ages, (chapter 6.4), demonstrating their maturation over time, similar to the transition from a liquid-like to a solid-like state observed in cells.

In addition, to the characterization of the states during progressive Tau aggregation, the interaction between Tau and cytoplasmic and nucleoplasmic organelles was investigated using IMARIS 3D reconstruction and colocalization analysis, shedding light on potential interactions of Tau aggregates with cellular processes (chapter 6.5).

In the subsequent discussion, I will focus on discussing these findings in the context of the current knowledge in the field, and ultimately propose a model for the transition of the soluble-to-liquid-to-solid transition of Tau during aggregation.

6.1 Tau accumulation appearance in HEK cell model

6.1.1. Tau accumulation types

Within the cytosol, two subtypes of inclusions were observed: small Tau clusters (CLUS) dispersed within the cell body or at the nuclear envelope (NE), and larger Tau accumulations (CYT) near the nucleus. Nuclear accumulations (NUC) were found within the nucleus, specifically in regions where DAPI-labeled DNA was absent.

These different types of accumulations could be clearly distinguished based on their size, fluorescent intensity, and localization. Interestingly, when closer examining CLUS and NE accumulations using StED microscopy, it was observed that these structures displayed a distinct short, elongated, and branched appearance, reminiscent of short fibrils. The presence of these small Tau fibrils on microtubules could already disrupt the microtubular system, contributing to pathological processes. In contrast, the CYT and NUC Tau accumulations displayed larger, amorphous clusters of these structures that - according to our FLIM/FRET data - did not represent amyloid-like Tau aggregates, suggesting that Tau aggregation into amyloid fibrils deposited in AD and FTD brains may go through multiple steps.

Tau nanoclusters have been previously observed on Taxol-stabilized microtubules (Vandebroek et al., 2006). Recent studies have also identified small Tau nanoclusters composed of dimers and trimers that bind to microtubules (Gyparaki et al., 2021), potentially serving as precursors to the formation of larger Tau aggregates. Notably, Tau nanoclusters are also observed using wildtype Tau, therefore not necessarily associated with Tau aggregation (Gyparaki et al., 2021).

Notably, not all cells exhibited the same pattern of Tau accumulation appearance. Some cells displayed CLUS/CYT and NUC accumulations but lacked NE accumulations. Each cell may, thus, propagate Tau in slightly different ways, leading to variations in the types of accumulations observed. This could, for example, be dependent on an individual cell's cell cycle status, exposure to Tau seeds (uptake from medium or transfer from neighboring cell), or 'cellular niche' (status of

neighboring cells). In any way, this observation underscores the need for analysis of Tau aggregation processes not only on the population but also on the individual cell level.

6.1.2. Do Tau accumulations associate with the cytoskeleton?

In this study, I used a combination of object-based and intensity-based colocalization analyses to determine Tau's localization with respect to the cytoskeleton and different organelles. We found that small Tau accumulations in the cytoplasm (Tau CLUS and NE) were associated with microtubules. Our StED images supported these findings, showing branching morphologies in Tau CLUS and CYT/NUC accumulations, supporting the hypothesis of Tau oligomerization on microtubules. In contrast, Tau CYT accumulations seemed to displace microtubules, indicating that the assembly state of CLUS and CYT Tau dictated different interactions - although they seem to be both built from small fibrillar Tau clusters.

Colocalization imaging between Tau and F-actin revealed an association between Tau CLUS and actin nodes. Previous *in vitro* experiments suggested a role of Tau in bridging between microtubules and F-actin filaments, potentially influencing their organization (Elie et al., 2015).

Similarly, Tau exhibited a strong association with Vimentin, an IF protein. Tau appeared to align along Vimentin filaments, and StED microscopy showed Tau CLUS and small Tau branches forming along Vimentin filaments and filling spaces between them. This could be due to Tau interacting with microtubules that associate with Vimentin fibers or interfering with the microtubule-Vimentin interaction, which would affect the stability and organization of the cytoskeleton (Schaedel et al., 2021).

Technical considerations: in the present study, I encountered limitations in colocalization methods, such as potential biases in structure reconstruction, the complexity of 3D reconstruction, and the importance of considering resolution limits and z-distortion in intensity-based methods. Despite these limitations, I believe my choice of combining object-based and intensity-based colocalization analyses was

valuable for studying the localization of Tau accumulations regarding cellular structures. The identification of molecular interaction partners needs further investigation.

6.1.3. Do Tau accumulations cause impairment of nuclear transport?

During cellular Tau aggregation, a significant reduction in soluble Tau occurred in both the cytoplasm (>50% decrease) and the nucleoplasm (>60%), indicating the sequestration of Tau into aggregates. Notably, the nucleus showed a more pronounced decrease compared to the cytoplasm, which occurred upon the appearance of aggregates around the nuclear envelope. These NE Tau clusters partially colocalized with NPCs and the Lamin layer of the nuclear envelope and may serve as seeds for nuclear NUC aggregates.

It was previously reported that Tau can impair nucleo-cytoplasmic transport based on its interaction with nuclear pore proteins (Nups) in the nuclear envelope, or the recruitment of Nups into Tau aggregates (Eftekharzadeh et al., 2018; Hochmair et al., 2022). In both cases these interactions can cause aberrations in NPC structure and function, which ultimately lead to a dysregulation of essential nucleocytoplasmic transport of proteins and RNA. Based on our results, small NE Tau clusters interacting with the nuclear envelope may hinder the diffusion of TauRD into the nucleus, maybe by blocking nuclear pores. However, we did not detect changes in the nuclear-cytosolic distribution of RFP in HEK cells with Tau accumulations, indicating that either the nuclear import deficit is specific to Tau, or that the observed nuclear Tau depletion is caused by a preferred recruitment of nuclear Tau into aggregates, or both. Large cytoplasmic CYT Tau aggregates close to the nuclear envelope could act as a sink for the recruitment of soluble Tau from both the nucleus and the cytosol.

6.1.4 Interaction between Tau and the ER and mitochondria

Emerging evidence suggests that Tau may interact with the ER, a vital organelle involved in protein synthesis, folding, and calcium regulation (Chami & Checler, 2020; Cieri et al., 2018; Hoozemans & Scheper, 2012). Our colocalization analysis revealed Tau clusters adjacent to tubular ER in the cytosol and at the nuclear envelope, which is practically an extension of the ER membrane system (Bragulat-Teixidor et al., 2023; Diez & Wegmann, 2020). Even after hypotonic shock leading to ER vesicle formation, some Tau clusters remained attached to the ER membrane. This suggested a robust Tau-ER interaction, at least for small Tau clusters. Previously, the interaction of soluble phosphorylated Tau with the ER was suggested. It has been proposed that there is an intricate interplay between the activation of the unfolded protein response (UPR) and the early emergence of Tau pathology, specifically soluble Tau cluster formation (Tau CLUS). This suggests a mutual influence between these two processes. Notably, research has unveiled that Tau aggregation can perturb calcium ion (Ca^{2+}) homeostasis and intracellular protein transport, consequently inciting an ER stress response. However, it is theorized that the UPR stress response precedes Tau hyperphosphorylation, supported by in vitro studies demonstrating that UPR can elevate Tau phosphorylation levels. Considering these findings alongside our presented data, it's conceivable that prior events induce the ER stress response, elevating Tau hyperphosphorylation. Subsequently, emerging Tau clusters (Tau CLUS), as indicated by hypotonic burst experiments, might strongly interfere with subsequent ER functions due to their robust binding.

This intricate interaction could potentially contribute to ER stress, a condition recognized for its ability to activate the UPR, ultimately disrupting essential cellular functions and potentially exacerbating neurodegenerative processes (Hoozemans & Scheper, 2012).

Conversely, accumulating evidence suggests Tau's interaction with mitochondria, essential energy-producing organelles. For example, Tau localizes to mitochondria-

associated ER membranes (MAM) in HeLa cells, sites where the ER and mitochondria closely interact (Cieri et al., 2018; David et al., 2005). This interaction has implications for pathological processes, including mitochondrial dysfunction, impaired mitochondrial transport, bioenergetic deficits, increased ROS production, and compromised mitochondrial dynamics (Cieri et al., 2018; David et al., 2005). Disrupted mitochondrial function, caused by aggregated Tau, could lead to oxidative stress, and neuronal damage. Our own colocalization analysis suggested that a subset of small cytosolic Tau clusters was in contact with mitochondria. This, or the attachment of Tau to microtubules, may impact mitochondrial trafficking and stress in neurons, which could further perpetuate Tau aggregation and neurodegeneration.

6.1.5. Suitability of the chosen cell model

For generating Tau accumulations, we used a HEK cell model expressing TauRD^{P301S}-CFP/YFP, a cell model widely used to study the aggregation of Tau (Cecon et al., 2023; Holmes & Diamond, 2014; Liu et al., 2023). However, by overexpressing a truncated form of Tau with a FTD-mutation (P301L), which adopts a conformation that favors aggregation (Nacharaju et al., 1999), both the microtubule binding as well as aggregation dynamics are altered compared to physiological expression levels of wildtype full-length Tau that aggregates in AD. The results obtained in this study therefore reflect rather an “aggressive” form of Tau aggregation in FTD, and translation into AD may be limited. In addition, the aggregation process may be influenced by the lack of neuronal context in HEK cells.
Since the expressed TauRD is small enough to diffuse through nuclear pores into the nucleus - in contrast to full-length Tau that remains almost entirely cytosolic - the observed nuclear accumulations (NUC) may resemble an artifact of the model. Nevertheless, since cellular aggregation of full-length wild-type Tau and TauP301L does not usually occur at the timescale of a cell culture, the chosen model gives at least an approximation for Tau aggregation in cells.
Another factor to consider is the spatial inhibition of TauRD aggregation due to the CFP/YFP tag. The fusion of fluorescent protein tags (CFP/YFP) to TauRD^{P301S} in the

HEK cell model can interfere with the assembly of Tau into amyloid-like fibrillar aggregates by changing the structure and localization of Tau aggregates (Kaniyappan et al., 2020). It is argued that the addition of these fluorescent tags interferes with the formation of amyloid-like structures. In this study, we observed amyloid-like packaging of Tau in a few larger cytosolic Tau aggregates.

6.2 Characterization of Tau accumulations and Tau condensates

6.2.1 Tau accumulations differ in their molecular exchange with the cytosol.

The oligomerization and aggregation of Tau molecules produced different types of Tau accumulations. We previously showed that Tau molecules can assemble into complexes reminiscent of different physical aggregate states - liquid-like condensates and solid-like aggregates (Hochmair et al., 2022) - which are characterized by different diffusion rates and packing densities of Tau molecules in them. To test whether the cellular Tau accumulation represented similar forms of Tau assemblies, we characterized them with FRAP and FLIM/FRET. Indeed, FRAP analysis, measuring how fast molecules in Tau accumulations exchange with their surrounding cytosol, suggested clear differences in diffusion rates among accumulation types (Figure 16). CLUS Tau showed reduced diffusion compared to free Tau in the cytosol, similar to liquid-condensed Tau (Hochmair et al., 2022). In contrast, CYT and NUC clusters did barely recover, indicating less Tau mobility in these forms of accumulations due to an increased polymerization state.

Since the decrease in FRAP matched the hierarchy of Tau accumulation occurrence, these findings suggest that cellular Tau may undergo a transition from a soluble monomeric state into a condensed liquid-like, and further into a densely packed aggregate state. Indeed, we were able to recapitulate this behavior of Tau *in vitro* using recombinant Tau.

The precise mechanism underlying Tau polymerization within condensates and the observed Tau CLUS remains a subject of ongoing investigation. However, specific structural alterations have been elucidated. For instance, recent research indicates that during Tau's LLPS, this intrinsically disordered protein undergoes a transition from a paperclip-like conformation to a more extended one. This structural shift involves the elongation of both the N- and C-termini of Tau, leading to increased accessibility of the MTB region, thereby facilitating nanocluster formation. Notably, this process is notably accelerated in the presence of AD mutations such as P301L and P301S (Wen et al., 2021).

Additionally, there is speculation that hyperphosphorylation of Tau enhances its β-sheet propensity within the repeat domain. This heightened β-sheet formation promotes oligomerization, resulting in alterations in charge distribution and composition (Wegmann et al., 2018)

Technical considerations: Applying FRAP had limitations due to motion-related errors in x, y, z-direction during live-cell imaging, which called for manual ROI adjustments for smaller NE and NUC accumulations. This challenges the precision of recovery rate for the smaller Tau accumulation types CLUS and NE. Additionally, whereas recovery after bleaching of small accumulations reports on a combination of internal rearrangement and supply of molecules from the surrounding, ROIs smaller than the accumulation itself report almost entirely on the internal redistribution of Tau molecules. However, the versatility of FRAP applications in cellular and *in vitro* experiments has made this technique a valuable tool for studying protein aggregation in various biological systems and disease contexts, including Tau (Lester et al., 2021), amyloid-beta (Tiwari et al., 2021), α-synuclein (Roberti et al., 2011), and prion proteins.

To overcome the limitations of FRAP, we complemented them with FLIM/FRET measurements, which are independent of bleaching and ROI definition during data acquisition, and therefore produce more reliable read-out.

6.2.2 FLIM-FRET suggests changes in packing density and molecular characteristics during maturation of Tau accumulations and condensates.

FLIM-FRET can probe protein-protein interactions and has been previously applied to investigate amyloid-like protein aggregation (Esbjörner et al., 2014; Gorlovoy et al., 2009; Lu et al., 2020; Rudenko et al., 2019).However, no comprehensive characterization of Tau accumulations in the cellular context has been done.
FLIM, unlike conventional microscopy relying on fluorescence intensity, measures the lifetime of donor fluorophores, or fluorescent proteins, which depends on the proximity to acceptor molecules (FRET part) but also on the surrounding environment (salt, pH) and the molecular density of the donor fluorophores. By analyzing fluorescence lifetime of Tau-RD-CFP in Tau accumulations, we could characterize these factors in the different Tau accumulations. The packing density of Tau accumulations was determined through fit-free FLIM-FRET analysis of the lifetime distribution in phasor plots. By comparing FLIM of Tau accumulations in cells expressing TauRD-CFP only with cells expressing both TauRD-CFP and TauRD-YFP, we were able to distinguish between the contribution of CFP self-quenching and CFP/YFP FRET.

Our FLIM data supported a hierarchical pattern of packing density from soluble Tau to CLUS/NE and further to CYT/NUC accumulations, which largely matched the data obtained by FRAP. NE Tau accumulations had a packing density similar to cytosolic small clusters. Similar NE clusters were previously suggested to be liquid-like, however, solely based on their FRAP recovery (Kang et al., 2021). A subpopulation of CYT accumulations displayed very low CFP lifetimes indicating a very dense packing of Tau molecules such as in amyloid-like fibrils observed in AD brains (Moloney et al., 2021). We previously confirmed the occurrence of amyloid-like Tau aggregates (=Amytracker-positive staining) in a subset (~10% of cells with CYT Tau) of these cells (Hochmair et al., 2022). In combination with the observed hierarchy of Tau accumulation occurrence, this suggested that Tau accumulations undergo a maturation process, in which small liquid-like Tau clusters first occur on microtubules

and then evolve into larger clusters of higher packing density near the nucleus. In a study using fixed cells (Hochmair et al., 2022), we obtained similar results as for the herein presented live-cell experiments. However, the dynamic range of CFP-lifetimes was much larger in non-fixed cells, allowing for more sensitivity in our FLIM measurements.

The lifetime of fluorophores, and hence also FLIM, is sensitive to the complex cellular microenvironment of the fluorophore, including pH, salt, and cellular crowding. To validate our findings in cells, we performed FLIM on in vitro reconstituted Tau-CFP and Tau-CFP/YFP condensates under controlled salt, pH, and crowding conditions. To test whether maturation of liquid Tau condensates was accompanied by an increase in Tau packing density - in analogy to a polymerization or percolation process (Pappu et al., 2022) - we measured FLIM in Tau condensates at three time points after their formation - at 1h, 4h, and 24h, representing different stages during the transition from liquid-like to solid-like Tau accumulations. While CFP lifetimes decreased only slightly over the first 4h, they markedly decreased in 24h-old Tau condensates. Interestingly, the CFP-lifetime of Tau in aged condensates was not homogenous like in 1h-old condensates but different CFP-lifetime populations occurred. This indicated that the maturation process involved the formation of heterogeneous Tau packing densities inside Tau condensates. In fact, we were able to confirm this idea subsequently by ODT of condensates (Figure 26; 6.3.3).

Finally, comparing the *in vitro* Tau condensate CFP-lifetimes with those of Tau accumulations in HEK cells, similarities emerged between CLUS/NE accumulations and the homogeneous distribution of Tau-CFP lifetimes in 1h- and 4h-old condensates within. The enhanced lifetime reduction in 24h-old condensates may resemble the one observed in CYT and AMY Tau accumulations, implying a consolidation process within condensates, as previously suggested from FRAP data(S. K. Rai et al., 2021; Wegmann et al., 2018).

In summary, FLIM-FRET data offer information about the structural characteristics of Tau accumulations and condensates, which in our study suggests a transition of

Tau molecules from soluble into liquid-condensed and solid-like assemblies during cellular Tau aggregation.

6.2.3 ODT reveals high protein concentration in condensates and cellular Tau accumulations.

ODT is an emerging label-free imaging technique in cell biology that allows studying the physical mass density of cellular structures in living cells. Previous studies have employed ODT to examine the density of the spindle apparatus in Xenopus during mitosis (Biswas et al., 2021), the nucleoplasm(Biswas et al., 2023), and protein stress granules formed by fused in sarcoma (FUS;(Schlüßler et al., 2021). We herein applied this technique for the first time to detect density differences between protein accumulations.

For Tau accumulations in cells, ODT measurements revealed distinct densities associated with the different types of accumulations and thereby provided further insights into their properties (Figure 20). CYT and NUC accumulations had densities of 212 ± 38 mg/ml and 218 ± 51 mg/ml, respectively (Figure 20). Assuming that most of the material in these accumulations is TauRD, they contain a ~100-fold higher concentration of Tau compared to soluble Tau in the cytosol of healthy neurons (average 0.2 mg/ml) (Iqbal et al., 2010). It is important to note, that this average value for the Tau concentration in an entire neuron likely underestimates the concentration of Tau in the axon of a healthy neuron. The estimated concentration of Tau within amyloid-like aggregates is approximately 3795 mg/ml, as calculated based on previous research findings. These calculations consider that there are approximately 4 Tau molecules for every 1nm of fibril length, with the total fibril length being around 80 nm (Von Bergen et al., 2006) Additionally, the thickness of TauRD fibrils, which are composed of Tau 14kDa TauRD, is approximately 6 nm, as reported by (Wegmann et al., 2010). To arrive at this estimation, we first assume a cylindrical shape for the fibril, which allows us to calculate a volume of 28.27 nm^3, equivalent to 2.827 × 10^-20 ml. Since TauRD has an actual size of 16 kDa, this corresponds to approximately 2.656 × 10^-17 mg. According to these calculations, it is important

to note that the measured densities for Tau within the, ODT analyzed, aggregates are significantly lower (approximately 10-fold lower) than these calculated values. This discrepancy suggests that these aggregates likely contain not only Tau but also other proteins, as indicated by colocalization analysis. Figures 27-35 illustrate that proteins co-stained with Tau are frequently found within the aggregates, implying that these Tau clusters interact not only with each other but also with surrounding proteins. As these aggregates mature into amyloid-like (AMY) aggregates, higher densities are observed, likely because more β-sheets are forming, leading to a greater packing density than in earlier stages.

Comparing mean densities of cellular Tau accumulations with densities of *in vitro* Tau condensates showed that the density of 1h and 4h-old Tau condensates resembles those of CYT and NUC accumulations in HEK cells. However, 24h-old Tau condensates displayed a decrease in average density but presented an inhomogeneous distribution of mass inside them. These observations were in line with our FLIM/FRET data showing multiple Tau-CFP lifetimes inside aged condensates.

Furthermore, while the mean concentration was lower in 24h compared to 4h-old condensates, their volume and total Tau mass still increased, suggesting that they were accumulating Tau over time, and that dense packing in parts of the condensates led to the reduced mean density. When analyzing the restructuring in 24h-old condensates in more detail, we found condensates with different density distributions, probably reflecting different maturation states. Prominent features were dense nodes and fibrillar structures in a net-like arrangement. In some condensates, all material seemed to have accumulated on the phase border of the condensates, forming a shell-like structure. A similar “shell” formation was previously already suggested for aging phospho-Tau condensates based on FRAP and microscopic fusion analysis (Wegmann et al., 2018). These observations explain why cellular Tau accumulation types showed increasingly lower FRAP. They also indicate that fibrillization of Tau inside condensates may be the origin of the seeding potential observed for aged Tau condensates (Hochmair et al., 2022).

Interestingly, the concentration of RNA in condensates decreases during their maturation. This indicated that RNA may be needed to promote Tau condensation (Hochmair et al., 2022) but loses its affinity to Tau upon Tau restructuring into fibrillar networks inside condensates. This would render RNA a catalyst of Tau LLPS and aggregation. In addition, remaining soluble Tau in 24h-old condensates may leave together with RNA, thereby further lowering the mass density but increasing structural complexity. These findings underscore the pivotal role of RNA-Tau interactions in orchestrating Tau condensate formation. However, as Tau polymerization progresses, RNA may be gradually excluded from the condensates due to a loss of binding affinity to polymerized Tau.

6.3.4 Tau aggregation impacts cyto- and nucleoplasm density

In cells, we detected an overall density increase of the cytoplasm and nucleoplasm of cells with Tau aggregates. This contrasts with our expectation based on the observation that soluble Tau gets efficiently sequestered into Tau aggregates and therefore does not contribute to cytoplasm crowding anymore. The elevation of cytoplasm density could be attributed, for example, to a reduced cell size/volume induced by Tau aggregation, as previously observed for NFTs in a mouse model of tauopathy (De Calignon et al., 2010). It could also result from Tau oligomers disrupting membrane integrity, causing cellular leakage (Ito et al., 2023).Tau aggregates can also hinder protein degradation mechanisms, induce oxidative stress, which in principle all could contribute to the observed physical change in cyto- and nucleoplasm density.

Surprisingly, we observed a decrease in nucleolar density in cells with Tau accumulation. Whether this impacts the main nucleolar function, ribosome biogenesis, remains to be clarified. It was previously reported that ribosome assembly and function are impaired in cell and animal models with Tau aggregation

(Evans et al., 2021; Koren et al., 2019), and that Tau can associate with the nucleolus (Maina et al., 2018). To which extent these observations relate to the observed decrease in nucleolar density needs to be tested.

6.4 Model for phase transition of soluble Tau into Tau aggregates

In this study, our primary objective was to comprehensively characterize distinct Tau aggregate phenotypes previously reported but not thoroughly examined(Hochmair et al., 2022). We began by uncovering their temporal sequence of appearance, with the initial discovery being the sequential emergence of these phenotypes. Utilizing Optical Diffraction ODT and FLIM, pronounced variations were identified in the characteristics of Tau aggregates. These observations substantiate the hypothesis that there exists a phase transition from soluble Tau to amyloid-like solid Tau aggregates. To provide a detailed characterization of the transition dynamics of potential Tau condensates (Tau CLUS/NE), the aforementioned measurement techniques were replicated on in vitro Tau condensates. The analysis identified a gelification process within the Tau condensates, consistent with prior findings (Wegmann et al., 2018). Intriguingly, ODT disclosed previously unreported fibrillization events within Tau condensates, insinuating a transformation of the condensates from a liquid-like state to solid Tau aggregates. Finally, through the application of immunohistochemistry in conjunction with high-resolution imaging, we illuminated the possible implications of these Tau aggregates on various cellular processes. This suggests that Tau aggregates may disrupt a multitude of cellular systems, including but not limited to the cytoskeleton, protein synthesis, and the nucleus.

In Figure 36, we present a proposed model that offers insights into the phase transition of Tau within Tau condensates. Initially, condensates rich in hyperphosphorylated Tau form, giving rise to small Tau clusters known as CLUS within the cytosol. These early assessments reveal that these condensates exhibit

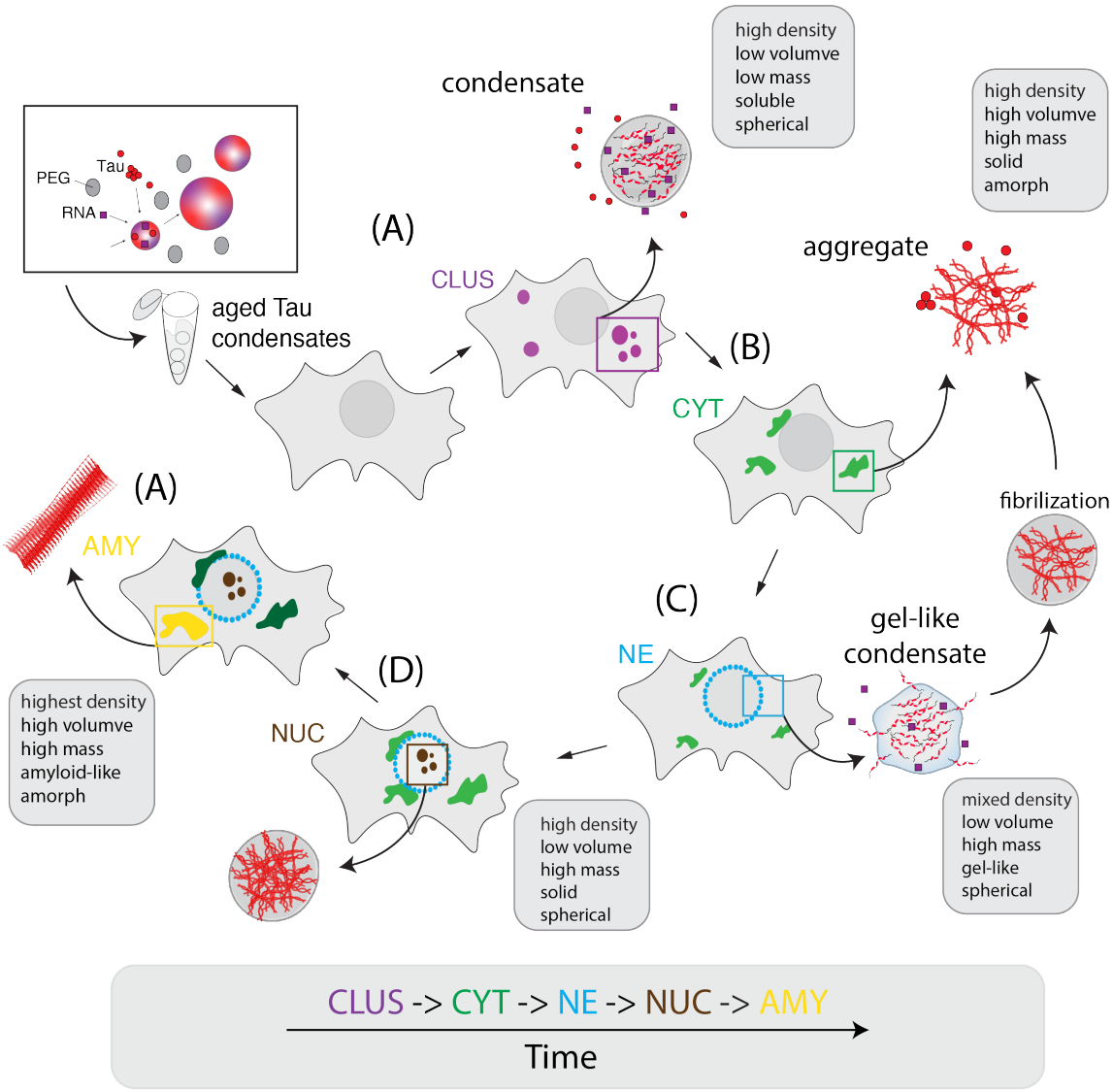

Figure 36. Schematic model of Tau LLPS transition in HEK cell model. (A) Initiation of Tau condensate formation (Tau CLUS) in HEK cells following transfection with aged Tau condensates. These Tau CLUS exhibit a uniform distribution and display high solubility. (B) Concurrently, small Tau CYT aggregates begin to emerge, originating from Tau oligomers as well as Tau condensates. These aggregates exhibit elevated concentrations and packing densities compared to Tau CLUS. (C) Small Tau NE aggregates become apparent in the vicinity of the nucleus. Within these condensates, Tau distribution becomes non-uniform due to percolation. Over time, these condensates initiate fibrilization, evolving into Tau aggregates. (D) Nuclear Tau aggregates (NUC) become detectable after the >15h time point. They exhibit densities similar to those of Tau CYT aggregates, suggesting that they may either be fibrilized Tau condensates, given their predominantly spherical appearance, or fragments of Tau CYT that have separated and migrated into the nucleus. (E) Gradually, Tau CYT aggregates undergo further maturation, eventually adopting an amyloid-like structure, likely attributable to the formation of highly stable beta-sheet arrangements.

liquid-like properties, as indicated by minimal FRET contributions and a low measured ODT variance. As time advances, these condensates undergo percolation, forming structures known as NE aggregates, which reposition themselves around the nucleus while retaining their characteristic spherical appearance. During percolation a significant reorganization occurs within the condensates, characterized by shifts in RNA and Tau concentrations, signifying a conformational transformation. The reduced dependence on RNA within the condensates aligns with the onset of Tau fibril formation.

In parallel, nascent Tau oligomers or protofibers begin to manifest, eventually contributing to the formation of Tau aggregates referred to as CYT. Since CYT and NE aggregates do not consistently appear together, it suggests that Tau aggregates may originate not only from percolated Tau condensates but also independently.

Next, solid-like aggregates eventually emerge within the nucleus (NUC). These aggregates could either represent fully percolated NE Tau condensates that migrated into the nucleus due to a rupture in the nuclear envelope or small Tau aggregates that have dissociated from CYT aggregates and subsequently relocated to the nucleus.

Finally, CYT aggregates undergo further structural transformations, transitioning into beta-sheet-rich aggregates that increasingly resemble amyloid plaques, as indicated by a notable increase in FRET contribution.

7 Methods

7.1 Tau LLPS and aggregation sample preparation

Condensate samples were prepared by adding final concentrations of 0.01 mg/ml unlabeled polyA-RNA or 0.001 mg/ml Cy5 -labeled polyA-RNA (1:10), 5% PEG8000 to a final concentration of 10µM Tau-CFP/YFP, with a 1:1 ratio between CFP and YFP labeled Tau (0.23 mg/ml) diluted in 25 mM HEPES, pH 7.4, 1 mM DTT. Samples were incubated at room temperature for 1h, 4h, 24h. Nuclease free H_2O was used for all buffer preparations to prevent degradation of RNA. Tau aggregation samples were prepared by adding final concentrations of 0.014 mg/ml heparin (82:1, Tau: heparin) to 25µM Tau, diluted in 25mM HEPES, 10mM NaCl, 1mM DTT, pH7.4. Samples were incubated at 37°C for 24h.

7.2 Immunofluorescence labeling of cells

The cells were subjected to a series of preparation steps for immunofluorescence staining. Firstly, they were rinsed with prewarmed phosphate-buffered saline (PBS) and fixed with 4% paraformaldehyde (PFA) in PBS for 15 minutes at room temperature (RT). This was followed by one wash with Tris-buffered saline (TBS) for 10 minutes and two additional washes with PBS.

To enable permeabilization, the cells were treated with 0.1% Triton X-100 in PBS for 20 minutes at RT, followed by two more washes with PBS. Subsequently, the cells were blocked with 5% normal goat serum (NGS) in PBS for 60 minutes at RT. Primary antibodies were then applied to the cells, including rabbit anti-Tubulin (1:1000, ab52866, Abcam), chicken anti-Vimentin (1:1000, ab73159, Abcam), rabbit/mouse anti-nucleophosmin (1:500, ab10530, Abcam), Acti-stain Phalloidin (1:1000, PHDN1-A), mouse anti-Lamin B Receptor (1:500, ab232731, Abcam), and mouse anti-Nuclear Pore Complex proteins (NPC) (1:1000, ab24609, Abcam). The primary antibodies were diluted in 3% NGS in PBS and incubated overnight at 4°C. After three washes with PBS, the cells were incubated with fluorescently labeled secondary antibodies (Alexa-labeled antibodies, Invitrogen) diluted at 1:1000 in 3%

NGS in PBS for 1 hour at room temperature. For STED microscopy, more fluorescently stable antibodies (abberior STAR-635P, ST635P-1001, Abberior) were specifically chosen. To stain the nuclei, DAPI (diluted 1:1000 in PBS) was applied for 10 minutes. Following two additional washes with PBS, the cells were stored at 4°C in PBS with 0.02% NaN_3 until imaging.

Imaging was performed using a Nikon confocal microscope (A1RSI+) equipped with a 60× oil objective for regular confocal images. For STED microscopy, a Leica Stellaris FALCON 8 with a 60× oil objective was used to acquire the images.

7.3 Cellular Tau seeding

HEK293 cells stably expressing the Tau-repeat domain (TauRD) containing the frontotemporal dementia (FTD)-mutation P301S and fused to CFP or YFP (HEK293 $TauRD^{P301S}$-CFP/YFP); ATCC #CRL-3275; cells were provided by Marc Diamond through Erich Wanker) were treated with OPTI-MEM culture medium containing 5µg total Tau (1.15 mg/ml). Prior to the treatment, Tau condensates were mixed with 1% lipofectamine 2000 (Invitrogen) for 15 min to facilitate Tau uptake. After 2 h, condensates and lipofectamine were diluted by addition of 2.5 volumes cell medium, and cells were incubated further for additional 24h. Induced intracellular TauRDP301S accumulations were detected by microscopy using the YFP fluorescence. Cells were imaged alive with a spinning disc confocal microscope (TiCSU-X, Nikon) using a 40× oil objective for quantification of aggregates, a laser scanning confocal microscope (A1Rs+, Nikon) equipped with a 60x oil objective and a Leica Stellaris Tau-STED confocal laser scanning microscope with FLIM for morphological, colocalization and FLIM analysis. The optical diffraction tomograms were obtained by using a custom-built diffraction tomography microscope. Nuclei were counterstained with SiR-DNA or DAPI. Quantification of the number of Tau accumulations per cells, and of different accumulation morphology types was done in Image J.

7.4 Distribution of Tau accumulations in cells

The distribution of accumulation types in cells was determined in three independent experiments from each seven confocal spinning disc images were taken in three wells (8-well dishes) Assignment of accumulation types was done manually on a cell-by-cell level. Differentiation between cytosolic accumulation (CYT) and nuclear envelope accumulation (NE) was based on size and intensity differences. Accumulations 3> the intensity of cytosolic diffuse Tau and an average diameter of ca 5µm defined CYT Tau. NE accumulations were defined as small 1-3 µm diameter puncta always located evenly around the nucleus. Nuclear Tau accumulatios (NUC) were classified as such based on their localization inside the nucleus. Since the total number of cells with accumulations (n cells) differed between experiments, the percentage of cells was always determined in respect to the total counted cells for each field of view. The number and distribution of Tau accumulation types (CYT, NE, NUC) was determined by counting all appearing accumulations, disregarding the presence of multiple accumulations of the same type and or the co-presence of other accumulations. Most cells showed more than one type of accumulations.

7.5 Time course live cell microscopy of Tau accumulations

HEK293 TauRD^{P301S}-CFP/YFP cells were cultivated in opti-MEM full medium (10% P/S, 5% FBS) and seeded (1:15) into 8-well dishes (ibidi) upon reaching 90% confluency. After the cells reached a confluency of around 60%, we treated them with the Tau condensates as described previously. Live cell microscopy was performed on a spinning disc confocal microscope (TiCSU-X), starting 6h after the transfection mix was added, because no accumulations were observed before. 10 µm z-stacks (step size 3µm) of cells were acquired with a 40x oil objective, two EMCCD cameras (8 iXon3 DU-888 ultra) at seven different positions spread among three different wells. Images were taken in two respective channels (YFP, DAPI), for 17-18h in 1h intervals at 37°C overnight. Analysis for the distribution of accumulations was done as mentioned previously. The total cell count for each

position was calculated by counting all visible cells at the beginning (t0) the middle (t8) and the end (t18) either manually or semi- automatically and then fitting them to either a linear increase or decrease to take cells leaving and entering the field of view into consideration. Tau accumulations were then normalized to their respective total cell count and then averaged across all positions (n=21).

7.6 FRAP measurements and analysis of cellular Tau accumulations

In FRAP (Fluorescence Recovery After Photobleaching) experiments conducted on HEK293-TauRDP301S-CFP/YFP cells, a partial bleaching of intracellular Tau accumulations was achieved by applying a laser intensity of 70% for three cycles, with a region of interest (ROI) diameter of approximately 1-2 µm. The recovery of the bleached region was then monitored for 60 seconds. Concurrently, background signals from areas outside the cells and reference signals from a different cell were recorded. To ensure accuracy, all FRAP curves were corrected for background fluorescence and normalized using the background-corrected reference signal. The experiments were carried out using a spinning disk confocal microscope (Eclipse-Ti CSU-X, Nikon) with a 60× objective lens.

7.7 Tau Localization and cell reconstruction

The characterization of the three-dimensional localization of Tau accumulations in cells involved the utilization of two microscopy systems: a laser scanning confocal microscope (Nikon scanning confocal A1RSI+) and a stimulated emission depletion (StED) microscope (Leica Stellaris Tau-STED). HEK293 TauRDP301S-CFP/YFP cells were transfected, fixed, and stained following the previously mentioned protocols.

Initially, z-stacks with a step size of 0.5 µm and dimensions of 1024x1024 pixels were acquired using the appropriate laser powers to achieve optimal resolution. To enhance the clarity of the images, deconvolution of the z-stacks was performed using either Imaris or Fiji Plugins such as "PSF generator" and "Deconvolution Lab". Subsequently, 3D reconstruction of the cells was carried out using the "surface

creation tool" in Imaris. For object-object based colocalization analysis, the shortest distance (0) between two reconstructed surfaces was measured. Additionally, the "Line plot profile" function in ImageJ was employed to analyze the staining's. This intensity-based colocalization analysis involved measuring the intensity of each colored channel along a selected line in a single plane. Peaks in the intensity profile that overlapped or were in close proximity to each other were considered indicative of colocalization.

To complement the colocalization results, higher-resolution STED images were acquired. The staining procedures for the STED experiments followed the same protocol as described earlier, with the use of STED-specific secondary antibodies (Aberrior-STAR-635P-antibodies against mouse, rabbit, and chicken). These antibodies were chosen based on their high fluorescent stability, which enhances the signal quality after depletion.

7.8 Fluorescent lifetime microscopy (FLIM) of eCFP-Tau condensates and HEK sensor cells

Tau: PEG: polyA condensates formed with 10µM eCFP-Tau and eCFP/YFP- Tau in 25 mM HEPES, 1 mM DTT, pH 7.4 were imaged 1h, 4h or 24h after formation. Tau aggregates were produced by incubating 50µM eCFP-Tau and eCFP/YFP-Tau (1:1) with heparin (1:4 molar ratio of heparin:Tau) in PBS, 1 mM DTT with 0.02% NaN_3 and incubated at 37°C for 6 days with addition of fresh DTT 2 mM every 48h. For FLIM, 2–3µl of each sample were pipetted on amine-treated glass-bottom dishes (TC-treated Miltenyi, CG 1.5). HEK293 TauRD^{P301S}-CFP/YFP and HEK293 TauRD^{P301S}-CFP cells were treated with Tau condensates one day prior to confocal FLIM on a Stellaris FALCON (Leica) equipped with a 60x oil objective. FLIM ROI was selected based on fluorescent intensities of recorded CFP (λEx=430 nm) and YFP (λEx=510 nm) channel. To each a photon count of at least 50,000 counts per detected lifetime after decomposition, CFP fluorescent lifetimes were recorded at λEx=430 nm with a laser intensity of 75%. CFP lifetimes of CYT, NE and NUC accumulations in recorded cells were manually defined in each individual FLIM image by placing circular ROIs in phasor plot of lifetime distribution, matching the

phasor mask image, and enabling a fit-free lifetime decomposition. Analysis was performed using LAS X software (Leica). Reduced fluorescent lifetimes of CFP (LT-2, LT-3, LT-4) indicate a lifetime reduction due to dense packing and in the case of CFP: YFP FRET.

7.9 Correlative Optical Diffraction Tomography (ODT) and confocal fluorescence microscopy of Tau aggregates

The three-dimensional (3D) refractive index (RI) of Tau aggregates was measured using a custom-built optical diffraction tomography (ODT) microscope employing Mach-Zehnder interferometry similar to the one described in Kim and Guck 2020 and Biswas et al., 2021(Biswas et al., 2021; Kim & Guck, 2020). Samples were illuminated with a 532nm wavelength laser (MSL-III-532, CNI laser) and spatially modulated holograms were measured from 150 different angles, from which the complex optical fields were retrieved. By mapping the Fourier spectra of retrieved optical fields onto the surface of the Ewald sphere in the 3D Fourier space according to the Fourier diffraction theorem, 3D RI tomograms were reconstructed. Detailed principles for tomogram reconstruction can be found in Wolf, 1969; Sung et al., 2009; Kim et al., 2014. Image acquisition, field retrieval, and RI tomogram reconstruction were performed using custom-written MATLAB scripts (R2020a). Along with ODT images, fluorescence images or image stacks (with a step size of 1 µm) were acquired using a Rescan Confocal Microscope (Luca et al., 2013; RCM1 from confocal.nl). To visualize nuclei, SiR-DNA was added (250nM final concentration) to HEK293T- TauRD^{P301S}-CFP/YFP cells lipo transfected with aged hTau40: Heparin condensates and grown in imaging dishes (81156, µ-Dish, ibidi) for 24h at 37°C . For ODT, a 60x water dipping objective (LUMPLFLN60XW, NA 1.0, Olympus Life Science) and a 100x oil immersion objective (UPlanFl, NA 1.3, Olympus Life Science) were used. The 100x objective was also used for the confocal fluorescence imaging. The mean RI value of each sample was measured by manually segmenting ROIs from the central slice of the reconstructed tomogram or the fluorescence image stack using FIJI (Schindelin et al., 2012). To calculate the mass density of each ROI,

we used the relationship $n=n_{medium}+\alpha C$ where, n = measured RI in the ROI, n_{medium} = RI of the assay medium (1.336, measured with Abbe refractometer: ABBE-2WAJ from Arcarda), α = RI increment (0.19 for proteins (Zhao et al., 2011)) and C = mass density in the ROI.

7.10 Analysis of ODT and fluorescence equatorial plane images of Tau condensates

As described above, a 3D tomogram is computed from multiple 2D quantitative phase images that are acquired upon illuminating the sample at various oblique angles. As the phase retardation in the 2D quantitative phase image is generated by the difference in the refractive index between the object and the surrounding medium, the absolute refractive index of the medium needs to be independently measured by an Abbe refractometer (Arcarda ABBE-2WAJ). Thus, for the condensates, the RI of the buffer (n_{buffer}) was first measured as an averaged value of the entire soluble Tau surrounding of the condensates and set to a reference value of 0.46 mg/mL. After tomogram reconstruction (Kim et al., 2013; Müller et al., 2015), each pixel within the image was assigned a calculated RI. Finally, from this RI value, the mass density of each condensate condition (1h, 4h, 24h) was directly calculated since the RI value in biological samples is linearly proportional to the mass density of material with the proportional coefficient of RI increment, α (Barer & Tkaczyk, 1954).The mass density of Tau condensates was calculated for each pixel in the equatorial planes of each measured droplet (5-8 z-planes based on Droplet size) Ri tomogram. This was done to take into consideration that Tau within the condensate might show a more heterogenous distribution. Using following relationship: $n_{condensate} = n_{buffer} + \alpha C_{condensate}$, where $n_{condensate}$ is the average RI of the condensate, n_{buffer} the RI of the condensate suspension buffer, α is the RI increment (0.190 mL/g for proteins and nucleic acids (Zhao et al., 2011) and $C_{condensate}$ the mass density inside the condensates. To calculate the average mass density of the 1h,4h,24h condensates an average z projection of the equatorial planes was created and then via radial clock scan measured. The ImageJ plugin “radial clock scan” measures the

average intensity in each radial scan. Furthermore, the provided standard deviation of these averaged radial intensities provides information on the variance of intensity values within each measured radial scan. From those, we then calculated the absolute protein concentration (mg/ml) and the amount of heterogeneity within the condensates.

7.11 Full Volume analysis of ODT and fluorescence images of Tau condensates

To comprehensively characterize the volume, mass, and density of Tau condensates, a thorough analysis of the entire volume was conducted. Following the construction of tomograms into z-stacks, the droplets were subjected to a detailed examination. For each timepoint, regions of interest (ROIs) were generated on individual planes by applying a threshold to the tomograms. The surface area on each plane was then quantified using the "Particle Analyzer" tool in ImageJ.
Next, the theoretical volume for each plane was determined by multiplying the measured area by the step size between the imaged planes. The volumes of all the individual planes were summed to calculate the complete volume of the droplet. Subsequently, the mass and density of the droplet were derived based on the calculated volume.

7.12 Data and statistical analysis

Image analysis was done in ImageJ and IMARIS. All data plotting, analysis, and statistical evaluation were performed using GraphPad Prism 9. Comparison of two groups was done by Student's t-test, multiple groups were compared by one-way ANOVA with Tukey or Holmes–Sidak test for multiple comparison, as indicated in the figure legends. ****P<0.0001, ***P<0.001, **P<0.01, *P<0.0.5.

8 Materials

8.1 Mammalian cell lines

HEK293T-TauRD^{p301S}	Epithelial cell line that was isolated 2014 from the kidney of a human embryo and subsequently cloned either with:
HEK293T-TauRD^{p301S}-CFP	TauRD fused to CFP
HEK293T-TauRD^{p301S}-CFP/YFP	TauRD fused to CFP and TauRD fused to YFP.

Table 1 Information about used cell lines.

8.2 Chemicals and Consumables

Chemical/Consumable	*Supplier*
Bovine Serum Albumin (BSA)	*Sigma-Aldrich*
Dimethyl sulfoxide (DMSO)	*Sigma-Aldrich*
Dithiothreitol (DTT)	*Serva*
Falcon™ 15 ml/50 ml Conical Centrifuge Tubes	*BD Biosciences*
Glycerol	*Merck*
µ-Slide 8 well^{high} ibiTreat	*Ibidi*
µ-Slide 8 well Glass Bottom	*Ibidi*
NaCl	*Roth*
Normal Goat Serum (NGS)	*Sigma-Aldrich*
35 mm Glass Bottom Dish	*Matek*
Polyethylene Glycol (PEG 8000)	*Promega*
Paraformaldehyde (16 %)	*Thermo Fisher Scientific*
Tris	*Applichem*
Triton™ X-100	*Sigma-Aldrich*
TWEEN. 20	*Sigma-Aldrich*

Table 2 Chemicals and Consumables

8.3 Proteins, dyes, and constructs

Proteins	*Supplier*
Human full-length wild-type Tau (hTau40)	Peptide by laboratory of Dr. Susanne Wegmann (DZNE, Berlin)
Human full-length wild-type Tau (hTau40) - CFP	Peptide by laboratory of Dr. Susanne Wegmann (DZNE, Berlin)
Human full-length wild-type Tau (hTau40) - YFP	Peptide by laboratory of Dr. Susanne Wegmann (DZNE, Berlin)
polyA-RNA	Peptide by laboratory of Dr. Susanne Wegmann (DZNE, Berlin)
Dyes	*Supplier*
Sir-Actin (50 nmol)	Spirochrome
Sir-Tubulin (50 nmol)	Spirochrome
Acti-Stain Phalloidin	Cytoskeleton, Inc.
Constructs	*Supplier*
pNG2 eCFP-Tau-6xHis	Merck-Novagen
pNG2 eYFP-Tau-6xHis	Merck-Novagen
4xmts-mScarlet-I	Addgene
ER-mscarlet-I (KDEL)	Addgene
ER-mapple-I (Sec61B)	Addgene

Table 3 Proteins, dyes, and constructs

8.4 Antibodies

Primary Antibodies	Species	Dilution	Supplier
a-Tubulin	rabbit	1:1000	Abcam
Vimentin	Chicken	1:1000	Abcam
Nucleophosmin	Mouse	1:500	Abcam
Lamin-B Receptor	Mouse	1:500	Abcam

Nuclear Pore Complex	Mouse	1:1000	Abcam

Secondary Antibodies	conjugate	Dilution	Supplier
Goat Anti-Mouse IgG H&L (Alexa Fluor® 647)	647	1:1000	Thermo-Fisher Scientific
Goat Anti-Rabbit IgG H&L (Alexa Fluor® 647)	*647*	1:1000	Thermo-Fisher Scientific
Goat anti-Chicken IgY (H+L) Cross-Adsorbed Secondary Antibody, DyLight 650	650	1:1000	Thermo-Fisher Scientific
Anti-mouse abberior Star-635P	635P	1:1000	Abberior
Anti-rabbit abberior Star-635P	635P	1:1000	Abberior
Anti-chicken abberior Star-635P	635P	1:1000	Abberior

Table 4 Antibodies

8.5 Buffers and Media

Buffer	
PBS	*137 mM NaCl, 27 mM KCl, 100 mM Na2HPO4, 17.6 mM KH2PO4*
HEPES buffer	*25 mM HEPES, 10 mM NaCl, 1 mM DTT*
Hypotonic buffer	H_2O, 10% (w/v) DMEM complete
Blocking solution	3% (w/v) NGS in PBS
DMEM complete	DMEM, 5 % FBS, 1 % P/S
OptiMEM	OptiMEM

Table 5 Buffers and Media

8.6 Cell culture supplies

Cell culture supplies	Supplier
DMEM	*Gibco*
Trypsin	*Gibco*
Penicillin/Streptomycin (P/S)	Gibco
Fetal bovine serum (FBS)	Gibco

Lipofectamine 2000	Thermo-Fisher -Scientific
Poly-L-Lysine solution	Sigma-Aldrich
OptiMEM	Gibco
Hoechst 33342	Life Technologies

Table 6 Cell culture supplies

8.7 Instruments and software

Instruments	Supplier
Leica Stellaris Tau-STED confocal laser scanning microscope with FLIM	*Leica*
AMBIO NIKON SCANNING CONFOCAL A1RSI+	*Nikon*
AMBIO NIKON SPINNING DISK CONFOCAL CSU-X	Nikon
AMBIO NIKON SORA SPINNING DISK CONFOCAL CSU-W1	Nikon
AMBIO NIKON WIDEFIELD TI2	Nikon
Rescan Confocal Microscope	Olympus

Table 7 Instruments

Software	Supplier
Microsoft Office 365	*Microsoft*
IMARIS	*Oxford Instruments*
ImageJ	Wayne Rasband
Mendeley	Mendeley Ltd.
GraphPad Prism 9	Graphpad software
Photoshop	Adobe
Illustrator	Adobe
MARIE	DZNE

Table 8 Software

9 References

2021 Alzheimer's disease facts and figures. (2021). *Alzheimer's and Dementia*, *17*(3), 327–406. https://doi.org/10.1002/alz.12328

2023 Alzheimer's disease facts and figures. (2023). *Alzheimer's & Dementia*. https://doi.org/10.1002/alz.13016

Ajit, D., Trzeciakiewicz, H., Tseng, J. H., Wander, C. M., Chen, Y., Ajit, A., King, D. P., & Cohen, T. J. (2019). A unique tau conformation generated by an acetylationmimic substitution modulates P301S-dependent tau pathology and hyperphosphorylation. *Journal of Biological Chemistry*, *294*(45), 16698–16711. https://doi.org/10.1074/jbc.RA119.009674

Alquezar, C., Arya, S., & Kao, A. W. (2021). Tau Post-translational Modifications: Dynamic Transformers of Tau Function, Degradation, and Aggregation. In *Frontiers in Neurology* (Vol. 11). Frontiers Media S.A. https://doi.org/10.3389/fneur.2020.595532

ALZHEIMER, A. (1906). Über einen eigenartigen schweren Er Krankungsprozeb der Hirnrinde. *Neurologisches Centralblatt*, *23*, 1129–1136. https://cir.nii.ac.jp/crid/1571135650732510208.bib?lang=en

Andreadis, A. (1992). *Structure and Novel Exons of the Human T Gene*.

Andreadis, A. (2005). Tau gene alternative splicing: Expression patterns, regulation, and modulation of function in normal brain and neurodegenerative diseases. In *Biochimica et Biophysica Acta - Molecular Basis of Disease* (Vol. 1739, Issue 2, pp. 91–103). https://doi.org/10.1016/j.bbadis.2004.08.010

Arevalo-Rodriguez, I., Smailagic, N., Roquéi Figuls, M., Ciapponi, A., Sanchez-Perez, E., Giannakou, A., Pedraza, O. L., Bonfill Cosp, X., & Cullum, S. (2015). Mini-Mental State Examination (MMSE) for the detection of Alzheimer's disease and other dementias in people with mild cognitive impairment (MCI). In *Cochrane Database of Systematic Reviews* (Vol. 2015, Issue 3). John Wiley and Sons Ltd. https://doi.org/10.1002/14651858.CD010783.pub2

B. Trinczek*, A. E. E.-M. M. and E. M. (1999). Tau regulates the attachment/detachment but not the speed of motors in microtubule-dependent transport of single vesicles and organelles. *Journal of Cell Science*, *112*, 2355–2367.

Bachmann, S., Bell, M., Klimek, J., & Zempel, H. (2021). Differential Effects of the Six Human TAU Isoforms: Somatic Retention of 2N-TAU and Increased Microtubule Number Induced by 4R-TAU. *Frontiers in Neuroscience*, *15*. https://doi.org/10.3389/fnins.2021.643115

Ballatore, C., Lee, V. M. Y., & Trojanowski, J. Q. (2007). Tau-mediated neurodegeneration in Alzheimer's disease and related disorders. In *Nature Reviews Neuroscience* (Vol. 8, Issue 9, pp. 663–672). https://doi.org/10.1038/nrn2194

Balupuri, A., Choi, K. E., & Kang, N. S. (2020). Aggregation mechanism of Alzheimer's amyloid β-peptide mediated by α-strand/α-sheet structure. *International Journal of Molecular Sciences*, *21*(3). https://doi.org/10.3390/ijms21031094

Bamburg, J. R., & Bloom, G. S. (2009). Cytoskeletal pathologies of Alzheimer disease. In *Cell Motility and the Cytoskeleton* (Vol. 66, Issue 8, pp. 635–649). https://doi.org/10.1002/cm.20388

Barer, S., & Tkaczyk, S. (1954). Refractive Index of Concentrated Protein Solutions. *Nature*.

Barghorn, S., Davies, P., & Mandelkow, E. (2004). Tau Paired Helical Filaments from Alzheimer's Disease Brain and Assembled in Vitro Are Based on β-Structure in the Core Domain. *Biochemistry*, *43*(6), 1694–1703. https://doi.org/10.1021/bi0357006

Becker, W. (2012). Fluorescence lifetime imaging - techniques and applications. *Journal of Microscopy*, *247*(2), 119–136. https://doi.org/10.1111/j.1365-2818.2012.03618.x

Biernat, J., Mandelkow, E. M., Schroter, C., Lichlenberg-Kraag, B., Steiner, B., Berling, B., Meyer, H., Mercken, M., Vandermeeren, A., Goedert, M., & Mandelkow, E. (1992). The switch of tau protein to an Alzheimer-like state includes the phosphorylation of two serine-proline motifs upstream of the microtubule binding region. *EMBO Journal*, *11*(4), 1593–1597. https://doi.org/10.1002/j.1460-2075.1992.tb05204.x

Biswas, A., Kim, K., Cojoc, G., Guck, J., & Reber, S. (2021). The Xenopus spindle is as dense as the surrounding cytoplasm. *Developmental Cell*, *56*(7), 967-975.e5. https://doi.org/10.1016/j.devcel.2021.03.013

Biswas, A., Muñoz, O., Kim, K., Hoege, C., Lorton, B. M., Shechter, D., Guck, J., Zaburdaev, V., & Reber, S. (2023). Conserved nucleocytoplasmic density homeostasis drives cellular organization across eukaryotes. *Biorxiv*. https://doi.org/10.1101/2023.09.05.556409

Boyko, S., Surewicz, K., & Surewicz, W. K. (2020). Regulatory mechanisms of tau protein fibrillation under the conditions of liquid-liquid phase separation. *PNAS*. https://doi.org/10.1073/pnas.2012460117/-/DCSupplemental

Braak, H., & Braak, E. (1991). Acta H' pathologica Neuropathological stageing of Alzheimer-related changes. In *Acta Neuropathol* (Vol. 82).

Braak, H., & Braak, E. (1995). Staging of Alzheimer's Disease-Related Neurofibrillary Changes. In *Neurobiology of Aging* (Vol. 16, Issue 95).

Bragulat-Teixidor, H., Ishihara, K., Szücs, G. M., & Otsuka, S. (2023). Title: The junctions connecting the endoplasmic reticulum to the nuclear envelope are constricted and remodelled during the cell cycle. *BioRxiv*. https://doi.org/10.1101/2023.01.31.526419

Brangwynne, C. P., Tompa, P., & Pappu, R. V. (2015). Polymer physics of intracellular phase transitions. *Nature Physics*, *11*(11), 899–904. https://doi.org/10.1038/nphys3532

Brettschneider, J., Del Tredici, K., Irwin, D. J., Grossman, M., Robinson, J. L., Toledo, J. B., Fang, L., Van Deerlin, V. M., Ludolph, A. C., Lee, V. M. Y., Braak, H., & Trojanowski, J. Q. (2014). Sequential distribution of pTDP-43 pathology in behavioral variant frontotemporal dementia (bvFTD). *Acta Neuropathologica*, *127*(3), 423–439. https://doi.org/10.1007/s00401-013-1238-y

Brusco, J., & Haas, K. (2015). Interactions between mitochondria and the transcription factor myocyte enhancer factor 2 (MEF2) regulate neuronal structural and functional plasticity and metaplasticity. *Journal of Physiology*, *593*(16), 3471–3481. https://doi.org/10.1113/jphysiol.2014.282459

Cabrales Fontela, Y., Kadavath, H., Biernat, J., Riedel, D., Mandelkow, E., & Zweckstetter, M. (2017). Multivalent cross-linking of actin filaments and microtubules through the microtubule-associated protein Tau. *Nature Communications*, *8*(1). https://doi.org/10.1038/s41467-017-02230-8

Capote, C., & Maccioni, R. B. (1998). The Association of Tau-Like Proteins with Vimentin Filaments in Cultured Cells. In *EXPERIMENTAL CELL RESEARCH* (Vol. 239).

Cecon, E., Oishi, A., Luka, M., Ndiaye-Lobry, D., François, A., Lescuyer, M., Panayi, F., Dam, J., Machado, P., & Jockers, R. (2023). Novel repertoire of tau biosensors to monitor pathological tau transformation and seeding activity in living cells. *ELife*, *12*. https://doi.org/10.7554/elife.78360

Chami, M., & Checler, F. (2020). Alterations of the Endoplasmic Reticulum (ER) Calcium Signaling Molecular Components in Alzheimer's Disease. In *Cells* (Vol. 9, Issue 12). NLM (Medline). https://doi.org/10.3390/cells9122577

Chatani, E., & Yamamoto, N. (2018). Recent progress on understanding the mechanisms of amyloid nucleation. In *Biophysical Reviews* (Vol. 10, Issue 2, pp. 527–534). Springer Verlag. https://doi.org/10.1007/s12551-017-0353-8

Chiti, F., & Dobson, C. M. (2017). *Protein Misfolding, Amyloid Formation, and Human Disease: A Summary of Progress Over the Last Decade*. https://doi.org/10.1146/annurev-biochem

Cho, J. H., & Johnson, G. V. W. (2003). Glycogen synthase kinase 3β phosphorylates tau at both primed and unprimed sites: Differential impact on microtubule binding. *Journal of Biological Chemistry*, *278*(1), 187–193. https://doi.org/10.1074/jbc.M206236200

Cieri, D., Vicario, M., Vallese, F., D'Orsi, B., Berto, P., Grinzato, A., Catoni, C., De Stefani, D., Rizzuto, R., Brini, M., & Calì, T. (2018). Tau localises within mitochondrial sub-compartments and its caspase cleavage affects ER-mitochondria interactions and cellular Ca 2+ handling. *Biochimica et Biophysica Acta - Molecular Basis of Disease*, *1864*(10), 3247–3256. https://doi.org/10.1016/j.bbadis.2018.07.011

Clavaguera, F., Bolmont, T., Crowther, R. A., Abramowski, D., Frank, S., Probst, A., Fraser, G., Stalder, A. K., Beibel, M., Staufenbiel, M., Jucker, M., Goedert, M., & Tolnay, M. (2009). Transmission and spreading of tauopathy in transgenic mouse brain. *Nature Cell Biology*, *11*(7), 909–913. https://doi.org/10.1038/ncb1901

Cummings, J. L., & Cole, G. (2002). *Alzheimer Disease*. http://jama.jamanetwork.com/

Cummings, J., Lee, G., Nahed, P., Kambar, M. E. Z. N., Zhong, K., Fonseca, J., & Taghva, K. (2022). Alzheimer's disease drug development pipeline: 2022. In *Alzheimer's and Dementia: Translational Research and Clinical Interventions* (Vol. 8, Issue 1). John Wiley and Sons Inc. https://doi.org/10.1002/trc2.12295

Cummings, J., Morstof, T., & Zhong, K. (2014). Alzheimers´s disease drug-development pipeline: fewe candidates, frequent failures. *Alzheimers Research & Therapy*.

David, D. C., Hauptmann, S., Scherping, I., Schuessel, K., Keil, U., Rizzu, P., Ravid, R., Dröse, S., Brandt, U., Müller, W. E., Eckert, A., & Götz, J. (2005). Proteomic and functional analyses reveal a mitochondrial dysfunction in P301L tau transgenic mice. *Journal of Biological Chemistry*, *280*(25), 23802–23814. https://doi.org/10.1074/jbc.M500356200

De Calignon, A., Fox, L. M., Pitstick, R., Carlson, G. A., Bacskai, B. J., Spires-Jones, T. L., & Hyman, B. T. (2010). Caspase activation precedes and leads to tangles. *Nature*, *464*(7292), 1201–1204. https://doi.org/10.1038/nature08890

De Calignon, A., Polydoro, M., Suárez-Calvet, M., William, C., Adamowicz, D. H., Kopeikina, K. J., Pitstick, R., Sahara, N., Ashe, K. H., Carlson, G. A., Spires-Jones, T. L., & Hyman, B. T. (2012). Propagation of Tau Pathology in a Model of Early Alzheimer's Disease. *Neuron*, *73*(4), 685–697. https://doi.org/10.1016/j.neuron.2011.11.033

Diez, L., & Wegmann, S. (2020). Nuclear Transport Deficits in Tau-Related Neurodegenerative Diseases. In *Frontiers in Neurology* (Vol. 11). Frontiers Media S.A. https://doi.org/10.3389/fneur.2020.01056

Dixit, R., Ross, J. L., Goldman, Y. E., & Holzbaur, E. L. F. (2008). Differential regulation of dynein and kinesin motor proteins by tau. *Science*, *319*(5866), 1086–1089. https://doi.org/10.1126/science.1152993

Drechsel, D. N., Hyman, A. A., Cobb, M. H., & Kirschner, M. W. (1992). Modulation of the Dynamic Instability of Tubulin Assembly by the Microtubule-Associated Protein Tau. In *Molecular Biology of the Cell* (Vol. 3).

Ebneth, A., Drewes, G., Mandelkow, E.-M., & Mandelkow, E. (1999). Phosphorylation of MAP2c and MAP4 by MARK Kinases Leads to the Destabilization of Microtubules in Cells. In *Cell Motil. Cytoskeleton* (Vol. 44).

Eftekharzadeh, B., Daigle, J. G., Kapinos, L. E., Coyne, A., Schiantarelli, J., Carlomagno, Y., Cook, C., Miller, S. J., Dujardin, S., Amaral, A. S., Grima, J. C., Bennett, R. E., Tepper, K., DeTure, M., Vanderburgh, C. R., Corjuc, B. T., DeVos, S. L., Gonzalez, J. A., Chew, J., … Hyman, B. T. (2018). Tau Protein Disrupts Nucleocytoplasmic Transport in Alzheimer's Disease. *Neuron*, *99*(5), 925-940.e7. https://doi.org/10.1016/j.neuron.2018.07.039

Eisenberg, D., & Jucker, M. (2012). The amyloid state of proteins in human diseases. In *Cell* (Vol. 148, Issue 6, pp. 1188–1203). Elsevier B.V. https://doi.org/10.1016/j.cell.2012.02.022

Eisenberg, D. S., & Sawaya, M. R. (2017). Structural studies of amyloid proteins at the molecular level. *Annual Review of Biochemistry*, *86*, 69–95. https://doi.org/10.1146/annurev-biochem-061516-045104

Elie, A., Prezel, E., Guérin, C., Denarier, E., Ramirez-Rios, S., Serre, L., Andrieux, A., Fourest-Lieuvin, A., Blanchoin, L., & Arnal, I. (2015). Tau co-organizes dynamic microtubule and actin networks. *Scientific Reports*, *5*. https://doi.org/10.1038/srep09964

Esbjörner, E. K., Chan, F., Rees, E., Erdelyi, M., Luheshi, L. M., Bertoncini, C. W., Kaminski, C. F., Dobson, C. M., & Kaminski Schierle, G. S. (2014). Direct observations of amyloid β Self-assembly in live cells provide insights into differences in the kinetics of Aβ (1-40) and Aβ (1-42) aggregation. *Chemistry and Biology*, *21*(6), 732–742. https://doi.org/10.1016/j.chembiol.2014.03.014

Evans, H. T., Taylor, D., Kneynsberg, A., Bodea, L. G., & Götz, J. (2021). Altered ribosomal function and protein synthesis caused by tau. *Acta Neuropathologica Communications*, *9*(1). https://doi.org/10.1186/s40478-021-01208-4

Fändrich, M., & Dobson, C. M. (2002). The behaviour of polyamino acids reveals an inverse side chain effect in amyloid structure formation. *EMBO Journal*, *21*(21), 5682–5690. https://doi.org/10.1093/emboj/cdf573

Feric, M., Vaidya, N., Harmon, T. S., Mitrea, D. M., Zhu, L., Richardson, T. M., Kriwacki, R. W., Pappu, R. V., & Brangwynne, C. P. (2016). Coexisting Liquid Phases Underlie Nucleolar Subcompartments. *Cell*, *165*(7), 1686–1697. https://doi.org/10.1016/j.cell.2016.04.047

Fitzpatrick, A. W. P., Falcon, B., He, S., Murzin, A. G., Murshudov, G., Garringer, H. J., Crowther, R. A., Ghetti, B., Goedert, M., & Scheres, S. H. W. (2017). Cryo-EM structures of tau filaments from Alzheimer's disease. *Nature*, *547*(7662), 185–190. https://doi.org/10.1038/nature23002

Frisoni, G. B., Pievani, M., Testa, C., Sabattoli, F., Bresciani, L., Bonetti, M., Beltramello, A., Hayashi, K. M., Toga, A. W., & Thompson, P. M. (2007). The topography of grey matter involvement in early and late onset Alzheimer's disease. *Brain*, *130*(3), 720–730. https://doi.org/10.1093/brain/awl377

Frost, B., Jacks, R. L., & Diamond, M. I. (2009). Propagation of Tau misfolding from the outside to the inside of a cell. *Journal of Biological Chemistry*, *284*(19), 12845–12852. https://doi.org/10.1074/jbc.M808759200

Fujiwara, I., Zweifel, M. E., Courtemanche, N., & Pollard, T. D. (2018). Latrunculin A Accelerates Actin Filament Depolymerization in Addition to Sequestering Actin Monomers. *Current Biology*, *28*(19), 3183-3192.e2. https://doi.org/10.1016/j.cub.2018.07.082

Goedert, M., & Jakes, R. (1990). Expression of separate isoforms of human tau protein: Correlation with the tau pattern in brain and effects on tubulin polymerization. *EMBO Journal*, *9*(13), 4225–4230. https://doi.org/10.1002/j.1460-2075.1990.tb07870.x

Goedert, M., & Spillantini, M. G. (1999). *Tau mutations in frontotemporal dementia FTDP-17 and their relevance for Alzheimer's disease*. www.elsevier.com/locate/bba

Goedert, M., & Spillantini, M. G. (2006). A century of Alzheimer's disease. In *Science* (Vol. 314, Issue 5800, pp. 777–781). https://doi.org/10.1126/science.1132814

Gorlovoy, P., Larionov, S., Pham, T. T. H., & Neumann, H. (2009). Accumulation of tau induced in neurites by microglial proinflammatory mediators. *The FASEB Journal*, *23*(8), 2502–2513. https://doi.org/10.1096/fj.08-123877

Götz, J., & Ittner, L. M. (2008). Animal models of Alzheimer's disease and frontotemporal dementia. In *Nature Reviews Neuroscience* (Vol. 9, Issue 7, pp. 532–544). Nature Publishing Group. https://doi.org/10.1038/nrn2420

Guo, J. L., Covell, D. J., Daniels, J. P., Iba, M., Stieber, A., Zhang, B., Riddle, D. M., Kwong, L. K., Xu, Y., Trojanowski, J. Q., & Lee, V. M. Y. (2013). Distinct α-Synuclein Strains Differentially Promote Tau Inclusions in Neurons. *Cell*, *154*(1), 103. https://doi.org/10.1016/j.cell.2013.05.057

Guo, T., Noble, W., & Hanger, D. P. (2017). Roles of tau protein in health and disease. In *Acta Neuropathologica* (Vol. 133, Issue 5, pp. 665–704). Springer Verlag. https://doi.org/10.1007/s00401-017-1707-9

Gyparaki, M. T., Arab, A., Sorokina, E. M., Santiago-Ruiz, A. N., Bohrer, C. H., Xiao, J., & Lakadamyali, M. (2021). Tau forms oligomeric complexes on microtubules that are distinct from tau aggregates. *PNAS*. https://doi.org/10.1073/pnas.2021461118/-/DCSupplemental

Haass, C., & Selkoe, D. J. (2007). Soluble protein oligomers in neurodegeneration: Lessons from the Alzheimer's amyloid β-peptide. In *Nature Reviews Molecular Cell Biology* (Vol. 8, Issue 2, pp. 101–112). https://doi.org/10.1038/nrm2101

Hardy, J., & Higgins, G. (1992). Alzheimer's Disease: The Amyloid Cascade Hypothesis. *Science*.

Hardy, J., & Selkoe, D. J. (2002). *The Amyloid Hypothesis of Alzheimer's Disease: Progress and Problems on the Road to Therapeutics*. http://science.sciencemag.org/

Harper, J. D., Wong, S. S., Lieber, C. M., & Lansbury, P. T. (1997). *Observation of metastable Ap amyloid protofibrils by atomic force microscopy*.

Herbert, L. E., Weuve, J., Scherr, P. A., & Evans, D. A. (2013). Alzheimer disease in the United States (2010-2050) estimated using 2010 census. *American Academy of Neurology*.

Hick, M., Herrmann, U., Weyer, S. W., Mallm, J. P., Tschäpe, J. A., Borgers, M., Mercken, M., Roth, F. C., Draguhn, A., Slomianka, L., Wolfer, D. P., Korte, M., & Müller, U. C. (2015). Acute function of secreted amyloid precursor protein fragment APPsα in synaptic plasticity. *Acta Neuropathologica*, *129*(1), 21–37. https://doi.org/10.1007/s00401-014-1368-x

Hippius, H., & Neundörfer, G. (2003). The discovery of Alzheimer`s disease. *Clinical Research*. https://www.ncbi.nlm.nih.gov/pmc/articles/PMC3181715/

Hirokawa, N., Noda, Y., Tanaka, Y., & Niwa, S. (2009). Kinesin superfamily motor proteins and intracellular transport. In *Nature Reviews Molecular Cell Biology* (Vol. 10, Issue 10, pp. 682–696). https://doi.org/10.1038/nrm2774

Hochmair, J., Exner, C., Franck, M., Dominguez-Baquero, A., Diez, L., Brognaro, H., Kraushar, M. L., Mielke, T., Radbruch, H., Kaniyappan, S., Falke, S., Mandelkow, E., Betzel, C., & Wegmann, S. (2022). Molecular crowding and RNA synergize to promote phase separation, microtubule interaction, and seeding of Tau condensates. *The EMBO Journal*, *41*(11), 1–28. https://doi.org/10.15252/embj.2021108882

Holmes, B. B., & Diamond, M. I. (2014). Prion-like properties of Tau protein: The importance of extracellular Tau as a therapeutic target. In *Journal of Biological Chemistry* (Vol. 289, Issue 29, pp. 19855–19861). American Society for

Biochemistry and Molecular Biology Inc. https://doi.org/10.1074/jbc.R114.549295

Holmes, B. B., Furman, J. L., Mahan, T. E., Yamasaki, T. R., Mirbaha, H., Eades, W. C., Belaygorod, L., Cairns, N. J., Holtzman, D. M., & Diamond, M. I. (2014). Proteopathic tau seeding predicts tauopathy in vivo. *Proceedings of the National Academy of Sciences of the United States of America*, *111*(41), E4376–E4385. https://doi.org/10.1073/pnas.1411649111

Hoozemans, J. J. M., & Scheper, W. (2012). Endoplasmic reticulum: The unfolded protein response is tangled in neurodegeneration. In *International Journal of Biochemistry and Cell Biology* (Vol. 44, Issue 8, pp. 1295–1298). Elsevier Ltd. https://doi.org/10.1016/j.biocel.2012.04.023

Hutton, M., & Hardy, J. (1997). The presenilins and Alzheimer's disease. In *Human Molecular Genetics* (Vol. 6, Issue 10). Oxford University Press.

Hutton, M., Lendon, C. L., Rizzu, P., Baker, M., Froelich, S., Houlden, H., Pickering-Brown, S., Chakraverty, S., Isaacs, A., Grover, A., Hackett, J., Adamson, J., Lincoln, S., Dickson, D., Davies, P., Petersen, R. C., Stevens, M., De Graaff, E., Wauters, E., … Heutink, P. (1998). *Association of missense and 5-splice-site mutations in tau with the inherited dementia FTDP-17*.

Iqbal, K., Liu, F., & Gong, C. X. (2016). Tau and neurodegenerative disease: The story so far. In *Nature Reviews Neurology* (Vol. 12, Issue 1, pp. 15–27). Nature Publishing Group. https://doi.org/10.1038/nrneurol.2015.225

Ito, N., Tsuji, M., Adachi, N., Nakamura, S., Sarkar, A. K., Ikenaka, K., Aguirre, C., Kimura, A. M., Kiuchi, Y., Mochizuki, H., Teplow, D. B., & Ono, K. (2023). Extracellular high molecular weight α-synuclein oligomers induce cell death by disrupting the plasma membrane. *NPJ Parkinson's Disease*, *9*(1), 139. https://doi.org/10.1038/s41531-023-00583-0

Ittner, L. M., & Götz, J. (2011). Amyloid-β and tau - A toxic pas de deux in Alzheimer's disease. *Nature Reviews Neuroscience*, *12*(2), 67–72. https://doi.org/10.1038/nrn2967

Ittner, L. M., Ke, Y. D., Delerue, F., Bi, M., Gladbach, A., van Eersel, J., Wölfing, H., Chieng, B. C., Christie, M. J., Napier, I. A., Eckert, A., Staufenbiel, M., Hardeman, E., & Götz, J. (2010). Dendritic function of tau mediates amyloid-β toxicity in alzheimer's disease mouse models. *Cell*, *142*(3), 387–397. https://doi.org/10.1016/j.cell.2010.06.036

Jack, C. R., Knopman, D. S., Jagust, W. J., Petersen, R. C., Weiner, M. W., Aisen, P. S., Shaw, L. M., Vemuri, P., Wiste, H. J., Weigand, S. D., Lesnick, T. G., Pankratz, V. S., Donohue, M. C., & Trojanowski, J. Q. (2013). Tracking pathophysiological processes in Alzheimer's disease: An updated hypothetical model of dynamic biomarkers. In *The Lancet Neurology* (Vol. 12, Issue 2, pp. 207–216). https://doi.org/10.1016/S1474-4422(12)70291-0

Jack, C. R., Knopman, D. S., Jagust, W. J., Shaw, L. M., Aisen, P. S., Weiner, M. W., Petersen, R. C., & Trojanowski, J. Q. (2010). Hypothetical model of dynamic biomarkers of the Alzheimer's pathological cascade. In *The Lancet Neurology* (Vol. 9, Issue 1, pp. 119–128). Lancet Publishing Group. https://doi.org/10.1016/S1474-4422(09)70299-6

Jack, C. R., Petersen, R. C., O'brien, P. C., & Tangalos, E. G. (1992). *MR-based hippocampal volumetry in the diagnosis of Alzheimer's disease*.

Jesu´, J., Avila, J., & Lucas, J. J. (2004). *Role of Tau Protein in Both Physiological and Pathological Conditions*. https://doi.org/10.1152/physrev.00024.2003.-The

Kadavath, H., Hofele, R. V., Biernat, J., Kumar, S., Tepper, K., Urlaub, H., Mandelkow, E., & Zweckstetter, M. (2015). Tau stabilizes microtubules by binding at the interface between tubulin heterodimers. *Proceedings of the National Academy of Sciences of the United States of America*, *112*(24), 7501–7506. https://doi.org/10.1073/pnas.1504081112

Kanaan, N. M., Hamel, C., Grabinski, T., & Combs, B. (2020). Liquid-liquid phase separation induces pathogenic tau conformations in vitro. *Nature Communications*, *11*(1). https://doi.org/10.1038/s41467-020-16580-3

Kanai, Y., & Hirokawa, N. (1995). Sorting Mechanisms of Tau and MAP2 in Neurons: Suppressed Axonal Transit of MAP2 and Locally Regulated Microtubule Binding. In *Neuron* (Vol. 14).

Kang, S. G., Han, Z. Z., Daude, N., McNamara, E., Wohlgemuth, S., Molina-Porcel, L., Safar, J. G., Mok, S. A., & Westaway, D. (2021). Pathologic tau conformer ensembles induce dynamic, liquid-liquid phase separation events at the nuclear envelope. *BMC Biology*, *19*(1). https://doi.org/10.1186/s12915-021-01132-y

Kaniyappan, S., Tepper, K., Biernat, J., Chandupatla, R. R., Hübschmann, S., Irsen, S., Bicher, S., Klatt, C., Mandelkow, E. M., & Mandelkow, E. (2020). FRET-based Tau seeding assay does not represent prion-like templated assembly of Tau filaments. *Molecular Neurodegeneration*, *15*(1). https://doi.org/10.1186/s13024-020-00389-1

Karch, C. M., & Goate, A. M. (2015). Alzheimer's disease risk genes and mechanisms of disease pathogenesis. In *Biological Psychiatry* (Vol. 77, Issue 1, pp. 43–51). Elsevier USA. https://doi.org/10.1016/j.biopsych.2014.05.006

Kemper, B., Carl, D., Schnekenburger, J., Bredebusch, I., Schäfer, M., Domschke, W., & von Bally, G. (2006). Investigation of living pancreas tumor cells by digital holographic microscopy. *Journal of Biomedical Optics*, *11*(3), 034005. https://doi.org/10.1117/1.2204609

Khanahmadi, M., Farhud, D. D., & Malmir, M. (2015). Genetic of Alzheimer's Disease: A Narrative Review Article. In *Iran J Public Health* (Vol. 44, Issue 7). http://ijph.tums.ac.ir

Kim, K., & Guck, J. (2020). The Relative Densities of Cytoplasm and Nuclear Compartments Are Robust against Strong Perturbation. *Biophysical Journal*, *119*(10), 1946–1957. https://doi.org/10.1016/j.bpj.2020.08.044

Kim, K., Yoon, H., Diez-Silva, M., Dao, M., Dasari, R. R., & Park, Y. (2013). High-resolution three-dimensional imaging of red blood cells parasitized by Plasmodium falciparum and in situ hemozoin crystals using optical diffraction tomography. *Journal of Biomedical Optics*, *19*(01), 1. https://doi.org/10.1117/1.jbo.19.1.011005

Kim, K., Yoon, J., Shin, S., Lee, S., Yang, S.-A., & Park, Y. (2016). *Optical diffraction tomography techniques for the study of cell pathophysiology*.

King, C., Sengupta, P., Seo, A. Y., & Lippincott-Schwartz, J. (2020). ER membranes exhibit phase behavior at sites of organelle contact. *PNAS*, *117*. https://doi.org/10.1073/pnas.1910854117/-/DCSupplemental

Klein, W. L., Krafft, G. A., Finch, C. E., & Andrus, E. P. (2001). Review Review Review Targeting small Aβ β oligomers: the solution to an Alzheimer's disease conundrum? In *TRENDS in Neurosciences* (Vol. 24, Issue 4). http://tins.trends.com0166

Kolaczkowska, E., & Kubes, P. (2013). Neutrophil recruitment and function in health and inflammation. *Nat Rev Immunol*, *13*(3), 159–175. https://doi.org/10.1038/nri3399

Koren, S. A., Hamm, M. J., Meier, S. E., Weiss, B. E., Nation, G. K., Chishti, E. A., Arango, J. P., Chen, J., Zhu, H., Blalock, E. M., & Abisambra, J. F. (2019). Tau drives translational selectivity by interacting with ribosomal proteins. *Acta Neuropathologica*, *137*(4), 571–583. https://doi.org/10.1007/s00401-019-01970-9

Kosik, K. S., Orecchio, D., Trojanowski, J. Q., M-Y lee, V., & Lee, G. (1988). Epitopes That Span the Tau Molecule Are Shared with Paired Helical Filaments. In *Neuron* (Vol. 1).

Kou, X., Chen, D., & Chen, N. (2020). The Regulation of microRNAs in Alzheimer's Disease. In *Frontiers in Neurology* (Vol. 11). Frontiers Media S.A. https://doi.org/10.3389/fneur.2020.00288

Kumar, D. K. V., Choi, H. S., Washicosky, K. J., Eimer, W. A., Tucker, S., Ghofrani, J., Lefkowitz, A., McColl, G., Goldstein, L. E., Tanzi, R. E., & Moir, R. D. (2016). Amyloid-β peptide protects against microbial infection in mouse and worm models of Alzheimer's disease. *Science Translational Medicine*, *8*(340). https://doi.org/10.1126/scitranslmed.aaf1059

Kumar, S., & Nussinov, R. (2002). Close-Range Electrostatic Interactions in Proteins. In *ChemBioChem* (Vol. 3). WILEY.

Larson, A. G., Elnatan, D., Keenen, M. M., Trnka, M. J., Johnston, J. B., Burlingame, A. L., Agard, D. A., Redding, S., & Narlikar, G. J. (2017). Liquid droplet formation by HP1α suggests a role for phase separation in heterochromatin. *Nature*, *547*(7662), 236–240. https://doi.org/10.1038/nature22822

Lasagna-Reeves, C. A., Castillo-Carranza, D. L., Sengupta, U., Guerrero-Munoz, M. J., Kiritoshi, T., Neugebauer, V., Jackson, G. R., & Kayed, R. (2012). Alzheimer brain-derived tau oligomers propagate pathology from endogenous tau. *Scientific Reports*, *2*. https://doi.org/10.1038/srep00700

Lee, G., & Leugers, C. J. (2012). Tau and tauopathies. In *Progress in Molecular Biology and Translational Science* (Vol. 107, pp. 263–293). Elsevier B.V. https://doi.org/10.1016/B978-0-12-385883-2.00004-7

Lester, E., Ooi, F. K., Bakkar, N., Ayers, J., Woerman, A. L., Wheeler, J., Bowser, R., Carlson, G. A., Prusiner, S. B., & Parker, R. (2021). Tau aggregates are RNA-protein assemblies that mislocalize multiple nuclear speckle components. *Neuron*, *109*(10), 1675-1691.e9. https://doi.org/10.1016/j.neuron.2021.03.026

Lin, Y., Fichou, Y., Longhini, A. P., Llanes, L. C., Yin, P., Bazan, G. C., Kosik, K. S., & Han, S. (2021). Liquid-Liquid Phase Separation of Tau Driven by Hydrophobic Interaction Facilitates Fibrillization of Tau. *Journal of Molecular Biology*, *433*(2). https://doi.org/10.1016/j.jmb.2020.166731

Lin, Y., Mccarty, J., Rauch, J. N., Delaney, K. T., Kosik, K. S., Fredrickson, G. H., Shea, J.-E., & Han, S. (2019). *Narrow equilibrium window for complex coacervation of tau and RNA under cellular conditions*. https://doi.org/10.7554/eLife.42571.001

Linse, S., Cabaleiro-Lago, C., Xue, W.-F., Lynch, I., Lindman, S., Thulin, E., Radford, S. E., & Dawson, K. A. (2007). *Nucleation of protein fibrillation by nanoparticles*. www.pnas.org/cgi/content/full/

Liu, F., Wu, R., Jin, N., Chu, D., Gu, J., Tung, Y. C., Hu, Z., Gong, C. X., & Iqbal, K. (2023). Two simple assays for assessing the seeding activity of proteopathic tau. *Frontiers in Aging Neuroscience*, *15*. https://doi.org/10.3389/fnagi.2023.1073774

Long, J. M., & Holtzman, D. M. (2019). Alzheimer Disease: An Update on Pathobiology and Treatment Strategies. In *Cell* (Vol. 179, Issue 2, pp. 312–339). Cell Press. https://doi.org/10.1016/j.cell.2019.09.001

Lü hrs, T., Ritter, C., Adrian, M., Riek-Loher, D., Bohrmann, B., Dö beli, H., Schubert, D., Riek, R., & Hoffmann-La Roche, F. (2005). *3D structure of Alzheimer's amyloid-(1-42) fibrils* (Vol. 29). www.pnas.orgcgidoi10.1073pnas.0506723102

Lu, M., Kaminski, C. F., & Schierle, G. S. K. (2020). Advanced fluorescence imaging of in situ protein aggregation. In *Physical Biology* (Vol. 17, Issue 2). Institute of Physics Publishing. https://doi.org/10.1088/1478-3975/ab694e

Maina, M. B., Al-Hilaly, Y. K., & Serpell, L. C. (2016). Nuclear tau and its potential role in alzheimer's disease. In *Biomolecules* (Vol. 6, Issue 1, pp. 2–20). MDPI AG. https://doi.org/10.3390/biom6010009

Maina, M. B., Bailey, L. J., Wagih, S., Biasetti, L., Pollack, S. J., Quinn, J. P., Thorpe, J. R., Doherty, A. J., & Serpell, L. C. (2018). The involvement of tau in nucleolar transcription and the stress response. *Acta Neuropathologica Communications*, *6*(1). https://doi.org/10.1186/s40478-018-0565-6

Mandelkow, E. M., Drewes, G., Biernat, J., Gustke, N., Van Lint, J., Vandenheede, J. R., & Mandelkow, E. (1992). Glycogen synthase kinase-3 and the Alzheimer-like state of microtubule-associated protein tau. *FEBS Letters*, *314*(3), 315–321. https://doi.org/10.1016/0014-5793(92)81496-9

Mandelkow, E. M., & Mandelkow, E. (2011). Biochemistry and cell biology of Tau protein in neurofibrillary degeneration. In *Cold Spring Harbor Perspectives in Biology* (Vol. 3, Issue 10, pp. 1–25). https://doi.org/10.1101/cshperspect.a006247

Masters, C. L., Simms, G., Weinman, N. A., Multhaupt, G., Mcdonald, B. L., & Beyreuthert, K. (1985). *Medical Sciences, 6009; tDepartment of Neuropathology, Royal Perth Hospital* (Vol. 82).

McParland, V. J., Kad, N. M., Kalverda, A. P., Brown, A., Kirwin-Jones, P., Hunter, M. G., Sunde, M., & Radford, S. E. (2000). Partially unfolded states of β-

microglobulin and amyloid formation in vitro. *Biochemistry*, *39*(30), 8735–8746. https://doi.org/10.1021/bi000276j

Medina, M., & Avila, J. (2014). New perspectives on the role of tau in Alzheimer's disease. Implications for therapy. In *Biochemical Pharmacology* (Vol. 88, Issue 4, pp. 540–547). Elsevier Inc. https://doi.org/10.1016/j.bcp.2014.01.013

Meisl, G., Kirkegaard, J. B., Arosio, P., Michaels, T. C. T., Vendruscolo, M., Dobson, C. M., Linse, S., & Knowles, T. P. J. (2016). Molecular mechanisms of protein aggregation from global fitting of kinetic models. *Nature Protocols*, *11*(2), 252–272. https://doi.org/10.1038/nprot.2016.010

Migliaccio, R., Agosta, F., Possin, K. L., Canu, E., Filippi, M., Rabinovici, G. D., Rosen, H. J., Miller, B. L., & Gorno-Tempini, M. L. (2015). Mapping the progression of atrophy in early- and late-onset alzheimer's disease. *Journal of Alzheimer's Disease*, *46*(2), 351–364. https://doi.org/10.3233/JAD-142292

Minoshima, S., Giordani, B., Berent, S., Frey, K. A., Foster, N. L., & Kuhl, D. E. (1997). Metabolic reduction in the posterior cingulate cortex in very early Alzheimer's disease. In *Ann Neurol* (Vol. 42).

Moloney, C. M., Lowe, V. J., & Murray, M. E. (2021). Visualization of neurofibrillary tangle maturity in Alzheimer's disease: A clinicopathologic perspective for biomarker research. In *Alzheimer's and Dementia* (Vol. 17, Issue 9, pp. 1554–1574). John Wiley and Sons Inc. https://doi.org/10.1002/alz.12321

Morris, M., Maeda, S., Vossel, K., & Mucke, L. (2011). The Many Faces of Tau. In *Neuron* (Vol. 70, Issue 3, pp. 410–426). https://doi.org/10.1016/j.neuron.2011.04.009

Mucke, L., Masliah, E., Yu, G.-Q., Mallory, M., Rockenstein, E. M., Tatsuno, G., Hu, K., Kholodenko, D., Johnson-Wood, K., & Mcconlogue, L. (2000). *High-Level Neuronal Expression of A 1-42 in Wild-Type Human Amyloid Protein Precursor Transgenic Mice: Synaptotoxicity without Plaque Formation*.

Müller, P., Schürmann, M., & Guck, J. (2015). *The Theory of Diffraction Tomography*. http://arxiv.org/abs/1507.00466

Nacharaju, P., Lewis, J., Easson, C., Yen, S., Hackett, J., Hutton, M., & Yen, S. H. (1999). Accelerated filament formation from tau protein with specific FTDP-17 missense mutations. *FEBS Letters*, *447*(2–3), 195–199. https://doi.org/10.1016/S0014-5793(99)00294-X

Nichols, E., Steinmetz, J. D., Vollset, S. E., Fukutaki, K., Chalek, J., Abd-Allah, F., Abdoli, A., Abualhasan, A., Abu-Gharbieh, E., Akram, T. T., Al Hamad, H., Alahdab, F., Alanezi, F. M., Alipour, V., Almustanyir, S., Amu, H., Ansari, I., Arabloo, J., Ashraf, T., … Vos, T. (2022). Estimation of the global prevalence of dementia in 2019 and forecasted prevalence in 2050: an analysis for the Global Burden of Disease Study 2019. *The Lancet Public Health*, *7*(2), e105–e125. https://doi.org/10.1016/S2468-2667(21)00249-8

Noble, W., Planel, E., Zehr, C., Olm, V., Meyerson, J., Suleman, F., Gaynor, K., Wang, L., Lafrancois, J., Feinstein, B., Burns, M., Krishnamurthy, P., Wen, Y., Bhat, R., Lewis, J., Dickson, D., & Duff, K. (2005). *Inhibition of glycogen synthase kinase-3 by lithium correlates with reduced tauopathy and degeneration in vivo*. www.pnas.orgcgidoi10.1073pnas.0500466102

Norton, S., Matthews, F. E., Barnes, D. E., Yaffe, K., & Brayne, C. (2014). Potential for primary prevention of Alzheimer's disease: An analysis of population-based data. *The Lancet Neurology*, *13*(8), 788–794. https://doi.org/10.1016/S1474-4422(14)70136-X

Palmqvist, S., Janelidze, S., Stomrud, E., Zetterberg, H., Karl, J., Zink, K., Bittner, T., Mattsson, N., Eichenlaub, U., Blennow, K., & Hansson, O. (2019). Performance of Fully Automated Plasma Assays as Screening Tests for Alzheimer Disease-Related β-Amyloid Status. *JAMA Neurology*, *76*(9), 1060–1069. https://doi.org/10.1001/jamaneurol.2019.1632

Panda, D., Samuel, J. C., Massie, M., Feinstein, S. C., & Wilson, L. (2003). *Differential regulation of microtubule dynamics by three-and four-repeat tau: Implications for the onset of neurodegenerative disease*. www.pnas.orgcgidoi10.1073pnas.1633508100

Pappu, R. V., Cohen, S. R., Dar, F., Farag, M., & Kar, M. (2022). Phase Transitions of Associative Biomacromolecules. In *Chemical Reviews*. American Chemical Society. https://doi.org/10.1021/acs.chemrev.2c00814

Pawley, J. B. (2006). *Handbook of biological confocal microscopy*. Springer.

Pellarin, R., & Caflisch, A. (2006). Interpreting the Aggregation Kinetics of Amyloid Peptides. *Journal of Molecular Biology*, *360*(4), 882–892. https://doi.org/10.1016/j.jmb.2006.05.033

Polanco, D., Carrancho, A., Gracia, P., & Cremades, N. (2022). Characterisation of Amyloid Aggregation and Inhibition by Diffusion-Based Single-Molecule Fluorescence Techniques. *Biophysica*, *2*(4), 506–524. https://doi.org/10.3390/biophysica2040043

Prince, P. R., Hochmair, J., Brognaro, H., Gevorgyan, S., Franck, M., Schubert, R., Lorenzen, K., Yazici, S., Mandelkow, E., Wegmann, S., & Betzel, C. (2023). Initiation and modulation of Tau protein phase separation by the drug suramin. *Scientific Reports*, *13*(1). https://doi.org/10.1038/s41598-023-29846-9

Puzzo, D., & Arancio, O. (2013). Amyloid-β peptide: Dr. Jekyll or Mr. Hyde? In *Journal of Alzheimer's Disease* (Vol. 33, Issue SUPPL. 1). IOS Press. https://doi.org/10.3233/JAD-2012-129033

Qian, W., Shi, J., Yin, X., Iqbal, K., Grundke-Iqbal, I., Gong, C.-X., & Liu, F. (2010). PP2A Regulates Tau Phosphorylation Directly and also Indirectly via Activating GSK-3β. *Journal of Alzheimer's Disease*, *19*, 1221–1229. https://doi.org/10.3233/JAD-2009-1317

Qiang, L., Sun, X., Austin, T. O., Muralidharan, H., Jean, D. C., Liu, M., Yu, W., & Baas, P. W. (2018). Tau Does Not Stabilize Axonal Microtubules but Rather Enables Them to Have Long Labile Domains. *Current Biology*, *28*(13), 2181-2189.e4. https://doi.org/10.1016/j.cub.2018.05.045

Querfurth, H. W., & LaFerla, F. M. (2010). Alzheimer's Disease. *New England Journal of Medicine*, *362*(4), 329–344. https://doi.org/10.1056/NEJMra0909142

Rai, A., Liu, T., Katrukha, E. A., Est Evez-Gallego, J., Manka, S. W., Paterson, I., Fernando D Iaz C, J., Kapitein, L. C., Moores, C. A., & Akhmanova, A. (2011). *Lattice defects induced by microtubule-stabilizing agents exert a long-range*

effect on microtubule growth by promoting catastrophes. https://doi.org/10.1073/pnas.2112261118/-/DCSupplemental

Rai, S. K., Savastano, A., Singh, P., Mukhopadhyay, S., & Zweckstetter, M. (2021). Liquid–liquid phase separation of tau: From molecular biophysics to physiology and disease. In *Protein Science* (Vol. 30, Issue 7, pp. 1294–1314). John Wiley and Sons Inc. https://doi.org/10.1002/pro.4093

Reiman, E. M., Quiroz, Y. T., Fleisher, A. S., Chen, K., Velez-Pardo, C., Jimenez-Del-Rio, M., Fagan, A. M., Shah, A. R., Alvarez, S., Arbelaez, A., Giraldo, M., Acosta-Baena, N., Sperling, R. A., Dickerson, B., Stern, C. E., Tirado, V., Munoz, C., Reiman, R. A., Huentelman, M. J., … Lopera, F. (2012). Brain imaging and fluid biomarker analysis in young adults at genetic risk for autosomal dominant Alzheimer's disease in the presenilin 1 E280A kindred: A case-control study. *The Lancet Neurology*, *11*(12), 1048–1056. https://doi.org/10.1016/S1474-4422(12)70228-4

Roberti, M. J., Jovin, T. M., & Jares-Erijman, E. (2011). Confocal fluorescence anisotropy and FRAP imaging of α-synuclein amyloid aggregates in living cells. *PLoS ONE*, *6*(8). https://doi.org/10.1371/journal.pone.0023338

Roses, A. D. (1996). APOLIPOPROTEIN E ALLELES AS RISK FACTORS IN ALZHEIMER'S DISEASE. In *Annu. Rev. Med* (Vol. 47). www.annualreviews.org

Rowe, C. C., Ellis, K. A., Rimajova, M., Bourgeat, P., Pike, K. E., Jones, G., Fripp, J., Tochon-Danguy, H., Morandeau, L., O'Keefe, G., Price, R., Raniga, P., Robins, P., Acosta, O., Lenzo, N., Szoeke, C., Salvado, O., Head, R., Martins, R., … Villemagne, V. L. (2010). Amyloid imaging results from the Australian Imaging, Biomarkers and Lifestyle (AIBL) study of aging. *Neurobiology of Aging*, *31*(8), 1275–1283. https://doi.org/10.1016/j.neurobiolaging.2010.04.007

Rudenko, L. K., Wallrabe, H., Periasamy, A., Siller, K. H., Svindrych, Z., Seward, M. E., Best, M. N., Bloom, G. S., & Alonso, A. (2019). Intraneuronal Tau Misfolding Induced by Extracellular Amyloid-β Oligomers. *Journal of Alzheimer's Disease*, *71*(4), 1125–1138. https://doi.org/10.3233/JAD-190226

Sakaue, F., Saito, T., Sato, Y., Asada, A., Ishiguro, K., Hasegawa, M., & Hisanaga, S. I. (2005). Phosphorylation of FTDP-17 mutant tau by cyclin-dependent kinase 5 complexed with p35, p25, or p39. *Journal of Biological Chemistry*, *280*(36), 31522–31529. https://doi.org/10.1074/jbc.M504792200

Sanders, D. W., Kaufman, S. K., DeVos, S. L., Sharma, A. M., Mirbaha, H., Li, A., Barker, S. J., Foley, A. C., Thorpe, J. R., Serpell, L. C., Miller, T. M., Grinberg, L. T., Seeley, W. W., & Diamond, M. I. (2014). Distinct tau prion strains propagate in cells and mice and define different tauopathies. *Neuron*, *82*(6), 1271–1288. https://doi.org/10.1016/j.neuron.2014.04.047

Schaedel, L., Lorenz, C., Schepers, A. V., Klumpp, S., & Köster, S. (2021). Vimentin intermediate filaments stabilize dynamic microtubules by direct interactions. *Nature Communications*, *12*(1). https://doi.org/10.1038/s41467-021-23523-z

Schindowski, K., Bretteville, A., Leroy, K., Bégard, S., Brion, J. P., Hamdane, M., & Buée, L. (2006). Alzheimer's disease-like tau neuropathology leads to memory deficits and loss of functional synapses in a novel mutated tau transgenic

mouse without any motor deficits. *American Journal of Pathology*, *169*(2), 599–616. https://doi.org/10.2353/ajpath.2006.060002
Schlüßler, R., Kim, K., Nötzel, M., Abuhattum, S., Beck, T., Müller, P., Maharana, S., Cojoc, G., Girardo, S., Hermann, A., Alberti, S., & Guck, J. (2021). Combined duorescence, optical diffraction tomography and Brillouin 2 microscopy 3. *Biorxiv*. https://doi.org/10.1101/2020.10.30.361808
Schmidt, H. B., & Görlich, D. (2016). Transport Selectivity of Nuclear Pores, Phase Separation, and Membraneless Organelles. In *Trends in Biochemical Sciences* (Vol. 41, Issue 1, pp. 46–61). Elsevier Ltd. https://doi.org/10.1016/j.tibs.2015.11.001
Selkoe, D. J. (1991). The Molecular Pathology of Alzheimer's Disease. In *Neuron* (Vol. 6).
Selkoe, D. J. (2001). *Alzheimer's Disease: Genes, Proteins, and Therapy*. http://physrev.physiology.org
Selkoe, D. J. (2011). Alzheimer's disease. In *Cold Spring Harbor Perspectives in Biology* (Vol. 3, Issue 7, pp. 1–16). https://doi.org/10.1101/cshperspect.a004457
Selkoe, D. J., & Hardy, J. (2016). The amyloid hypothesis of Alzheimer's disease at 25 years. *EMBO Molecular Medicine*, *8*(6), 595–608. https://doi.org/10.15252/emmm.201606210
Sengupta, A., Kabat, J., Novak, M., Wu, Q., Grundke-Iqbal, I., & Iqbal, K. (1998). *Phosphorylation of Tau at Both Thr 231 and Ser 262 Is Required for Maximal Inhibition of Its Binding to Microtubules*.
Shankar, G. M., Li, S., Mehta, T. H., Garcia-Munoz, A., Shepardson, N. E., Smith, I., Brett, F. M., Farrell, M. A., Rowan, M. J., Lemere, C. A., Regan, C. M., Walsh, D. M., Sabatini, B. L., & Selkoe, D. J. (2008). Amyloid-β protein dimers isolated directly from Alzheimer's brains impair synaptic plasticity and memory. *Nature Medicine*, *14*(8), 837–842. https://doi.org/10.1038/nm1782
Soto, C. (2003). Unfolding the role of protein misfolding in neurodegenerative diseases. *Nature Reviews Neuroscience*, *4*(1), 49–60. https://doi.org/10.1038/nrn1007
Spillantini, M. G., & Goedert, M. (1998). Tau protein pathology in neurodegenerative diseases. *Trends Neuroscience*.
Sprague, B. L., & McNally, J. G. (2005). FRAP analysis of binding: Proper and fitting. In *Trends in Cell Biology* (Vol. 15, Issue 2, pp. 84–91). https://doi.org/10.1016/j.tcb.2004.12.001
Stelzmann, R. A., Norman Schnitzlein, H., & Reed Murtagh, F. (1995). An english translation of alzheimer's 1907 paper, "über eine eigenartige erkankung der hirnrinde." *Clinical Anatomy*, *8*(6), 429–431. https://doi.org/10.1002/ca.980080612
Stopschinski, B. E., Thomas, T. L., Nadji, S., Darvish, E., Fan, L., Holmes, B. B., Modi, A. R., Finnell, J. G., Kashmer, O. M., Estill-Terpack, S., Mirbaha, H., Luu, H. S., & Diamond, M. I. (2020). A synthetic heparinoid blocks Tau aggregate cell uptake and amplification. *Journal of Biological Chemistry*, *295*(10), 2974–2983. https://doi.org/10.1074/jbc.RA119.010353

Sunde, M., & Blake, C. (1997). The structure of amyloid fibrils by electron microscopy and x-ray diffraction. In *Advances in Protein Chemistry* (Vol. 50, pp. 123–159). Academic Press Inc. https://doi.org/10.1016/s0065-3233(08)60320-4

Tackenberg, C., & Nitsch, R. M. (2019). The secreted APP ectodomain sAPPα, but not sAPPβ, protects neurons against Aβ oligomer-induced dendritic spine loss and increased tau phosphorylation. *Molecular Brain*, *12*(1). https://doi.org/10.1186/s13041-019-0447-2

Takeda, S., Wegmann, S., Cho, H., Devos, S. L., Commins, C., Roe, A. D., Nicholls, S. B., Carlson, G. A., Pitstick, R., Nobuhara, C. K., Costantino, I., Frosch, M. P., Muller, D. J., Irimia, D., & Hyman, B. T. (2015). Neuronal uptake and propagation of a rare phosphorylated high-molecular-weight tau derived from Alzheimer's disease brain. *Nature Communications*, *6*. https://doi.org/10.1038/ncomms9490

Tanzi, R. E., & Bertram, L. (2005). Twenty years of the Alzheimer's disease amyloid hypothesis: A genetic perspective. In *Cell* (Vol. 120, Issue 4, pp. 545–555). Elsevier B.V. https://doi.org/10.1016/j.cell.2005.02.008

Thinakaran, G., & Koo, E. H. (2008). Amyloid precursor protein trafficking, processing, and function. In *Journal of Biological Chemistry* (Vol. 283, Issue 44, pp. 29615–29619). https://doi.org/10.1074/jbc.R800019200

Tilley, L., Morgan, K., & Kalsheker, N. (1998). Reviews Genetic risk factors in Alzheimer's disease. In *J Clin Pathol: Mol Pathol* (Vol. 51).

Tiwari, A., Pradhan, S., Sannigrahi, A., Jha, S., Biswas, M., & Saleem, M. (2021). In vitro reconstitution demonstrates the amyloid-beta mediated myelin membrane deformation 2 3. *BioRxiv*. https://doi.org/10.1101/2021.08.13.456302

Tripathi, T., Prakash, J., & Shav-Tal, Y. (2019). Phospho-Tau Impairs Nuclear-Cytoplasmic Transport. In *ACS Chemical Neuroscience* (Vol. 10, Issue 1, pp. 36–38). American Chemical Society. https://doi.org/10.1021/acschemneuro.8b00632

Tycko, R. (2011). Solid-state NMR studies of amyloid fibril structure. *Annual Review of Physical Chemistry*, *62*, 279–299. https://doi.org/10.1146/annurev-physchem-032210-103539

Vandebroek, T., Terwel, D., Vanhelmont, T., Gysemans, M., Van Haesendonck, C., Engelborghs, Y., Winderickx, J., & Van Leuven, F. (2006). Microtubule binding and clustering of human Tau-4R and Tau-P301L proteins isolated from yeast deficient in orthologues of glycogen synthase kinase-3β or cdk5. *Journal of Biological Chemistry*, *281*(35), 25388–25397. https://doi.org/10.1074/jbc.M602792200

Vassar, R., Bennett, B. D., Babu-Khan, S., Kahn, S., Mendiaz, E. A., Denis, P., Teplow, D. B., Ross, S., Amarante, P., Loeloff, R., Luo, Y., Fisher, S., Fuller, J., Edenson, S., Lile, J., Jarosinski, M. A., Biere, A. L., Curran, E., Burgess, T., … Citron, M. (1999). *Secretase Cleavage of Alzheimer's Amyloid Precursor Protein by the Transmembrane Aspartic Protease BACE*. www.sciencemag.org

Von Bergen, M., Barghorn, S., Müller, S. A., Pickhardt, M., Biernat, J., Mandelkow, E. M., Davies, P., Aebi, U., & Mandelkow, E. (2006). The core of tau-paired helical filaments studied by scanning transmission electron microscopy and limited proteolysis. *Biochemistry*, *45*(20), 6446–6457. https://doi.org/10.1021/bi052530j

Walsh, D. M., Klyubin, I., Fadeeva, J. V, Cullen, W. K., Anwyl, R., Wolfe, M. S., Rowan, M. J., & Selkoe, D. J. (2002). *Naturally secreted oligomers of amyloid b protein potently inhibit hippocampal long-term potentiation in vivo*. www.nature.com

Wang, L. Q., Zhao, K., Yuan, H. Y., Wang, Q., Guan, Z., Tao, J., Li, X. N., Sun, Y., Yi, C. W., Chen, J., Li, D., Zhang, D., Yin, P., Liu, C., & Liang, Y. (2020). Cryo-EM structure of an amyloid fibril formed by full-length human prion protein. *Nature Structural and Molecular Biology*, *27*(6), 598–602. https://doi.org/10.1038/s41594-020-0441-5

Wang, X., Su, B., Perry, G., Smith, M. A., & Zhu, X. (2007). Insights into amyloid-β-induced mitochondrial dysfunction in Alzheimer disease. In *Free Radical Biology and Medicine* (Vol. 43, Issue 12, pp. 1569–1573). https://doi.org/10.1016/j.freeradbiomed.2007.09.007

Wang, Y., & Mandelkow, E. (2016). Tau in physiology and pathology. In *Nature Reviews Neuroscience* (Vol. 17, Issue 1, pp. 5–21). Nature Publishing Group. https://doi.org/10.1038/nrn.2015.1

Wegmann, S., Eftekharzadeh, B., Tepper, K., Zoltowska, K. M., Bennett, R. E., Dujardin, S., Laskowski, P. R., MacKenzie, D., Kamath, T., Commins, C., Vanderburg, C., Roe, A. D., Fan, Z., Molliex, A. M., Hernandez-Vega, A., Muller, D., Hyman, A. A., Mandelkow, E., Taylor, J. P., & Hyman, B. T. (2018). Tau protein liquid–liquid phase separation can initiate tau aggregation. *The EMBO Journal*, *37*(7). https://doi.org/10.15252/embj.201798049

Wegmann, S., Yu, J. J., Chinnathambi, S., Mandelkow, E. M., Mandelkow, E., & Muller, D. J. (2010). Human tau isoforms assemble into ribbon-like fibrils that display polymorphic structure and stability. *Journal of Biological Chemistry*, *285*(35), 27302–27313. https://doi.org/10.1074/jbc.M110.145318

Wen, J., Hong, L., Krainer, G., Yao, Q. Q., Knowles, T. P. J., Wu, S., & Perrett, S. (2021). Conformational Expansion of Tau in Condensates Promotes Irreversible Aggregation. *Journal of the American Chemical Society*, *143*(33), 13056–13064. https://doi.org/10.1021/jacs.1c03078

Wright, P. E., & Dyson, H. J. (2015). Intrinsically disordered proteins in cellular signalling and regulation. In *Nature Reviews Molecular Cell Biology* (Vol. 16, Issue 1, pp. 18–29). Nature Publishing Group. https://doi.org/10.1038/nrm3920

Wu, J. W., Hussaini, S. A., Bastille, I. M., Rodriguez, G. A., Mrejeru, A., Rilett, K., Sanders, D. W., Cook, C., Fu, H., Boonen, R. A. C. M., Herman, M., Nahmani, E., Emrani, S., Figueroa, Y. H., Diamond, M. I., Clelland, C. L., Wray, S., & Duff, K. E. (2016). Neuronal activity enhances tau propagation and tau pathology in vivo. *Nature Neuroscience*, *19*(8), 1085–1092. https://doi.org/10.1038/nn.4328

Zhao, H., Brown, P. H., & Schuck, P. (2011). On the distribution of protein refractive index increments. *Biophysical Journal*, *100*(9), 2309–2317. https://doi.org/10.1016/j.bpj.2011.03.004

Zheng, H., & Koo, E. H. (2011). Biology and pathophysiology of the amyloid precursor protein. In *Molecular Neurodegeneration* (Vol. 6, Issue 1). https://doi.org/10.1186/1750-1326-6-27

Zlokovic, B. V. (2011). Neurovascular pathways to neurodegeneration in Alzheimer's disease and other disorders. In *Nature Reviews Neuroscience* (Vol. 12, Issue 12). https://doi.org/10.1038/nrn3114